Physics and Physical Oceanography Data Report 2014 I

Analysis of Physical Oceanographic Data from Lake Melville, Labrador, September 2012 - July 2013

Zhaoshi Lu, Brad deYoung, and Samantha Banton

April 30, 2014

Department of Physics and Physical Oceanography
Memorial University of Newfoundland
St. Johns, Newfoundland
A1B 3X7

Abstract

A cruise was carried out during September 2012 in Lake Melville, a large and complex sub-Arctic fjord which serves as a major outlet for freshwater on the Labrador coast, to deploy oceanographic meters with which to collect data on the circulation and hydrography of Lake Melville. Two moorings were deployed to record current velocity and temperature from September 2012 to June 2013. All the moorings included ADCP to measure water speed and thermistors to measure water temperature. Temperature, salinity and density profiles, were collected from CTD casts surveys made at 41 stations from June 15 to July 3, 2013. We present plots of the raw data, statistical analyses, and information on quality control processes.

Acknowledgements

We thank the captain and crew of the What's Happening for their help in the deployment and recovery of the instrumentation. We also acknowledge the support of NSERC and the NCE Arcticnet Program.

Contents

List of Figures

List of Tables

Chapter 1

Introduction

An estuary is a semi-enclosed coastal area of interaction between salt and fresh water. It has one or more rivers flowing into, and a free connection to the open sea. Fjord estuaries, formed by glacial erosion and generally occur at higher latitude. A fjord usually has a river/rivers running into the basin at its head, and a sill near its mouth to the open ocean, isolating the deeper waters of the fjord from the ocean. As a result, a fjords are often a highly stratified, with freshwater at the surface and trapped heavier sea water at the bottom. The typical fjord is relatively long and narrow and with a deep in the basin. The environment in fjord is generally the result of a dynamic balance between factors such as tides, river runoff and sea salinity, local meteorological conditions, and topography.

Hamilton Inlet is the largest inlet on the coast of Labrador and consists of Goose Bay, Lake Melville and Groswater Bay. Hamilton Inlet may be classified as a fjord-type estuary system, based on topography and degree of stratification. Hamilton Inlet serves as a major outlet for freshwater on the Labrador coast (Figure 1.1). Groswater Bay extends west for approximately 50 km, and it then constricts into a narrow shallow channel (known as the Narrows) of about 22 km in length, 2.5 km in width and 30 m in depth. Lake Melville extends west for 170 km from the Narrows, with a basin depth of over 200 m and a maximum width of 35 km. Goose Bay, a 22 km extension of Lake Melville, has a depth of over 60 m. Fresh water is discharged into the lake at the southwestern end by four major rivers (Churchill River, Northwest, the Kenamu, and the Goose, in order of size (Figure 1.2).

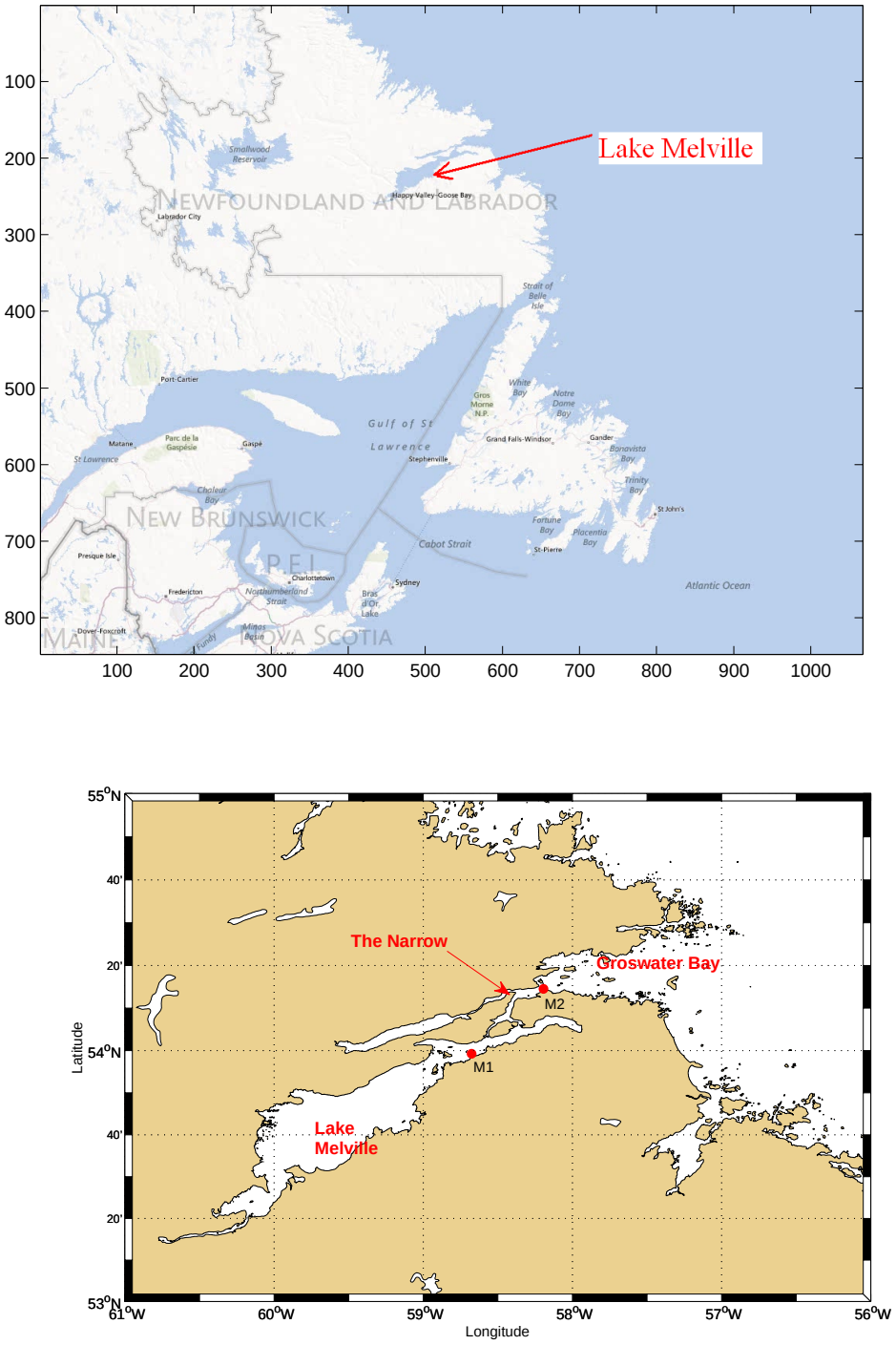

Figure 1.1: Location of Lake Melville, Labrador.

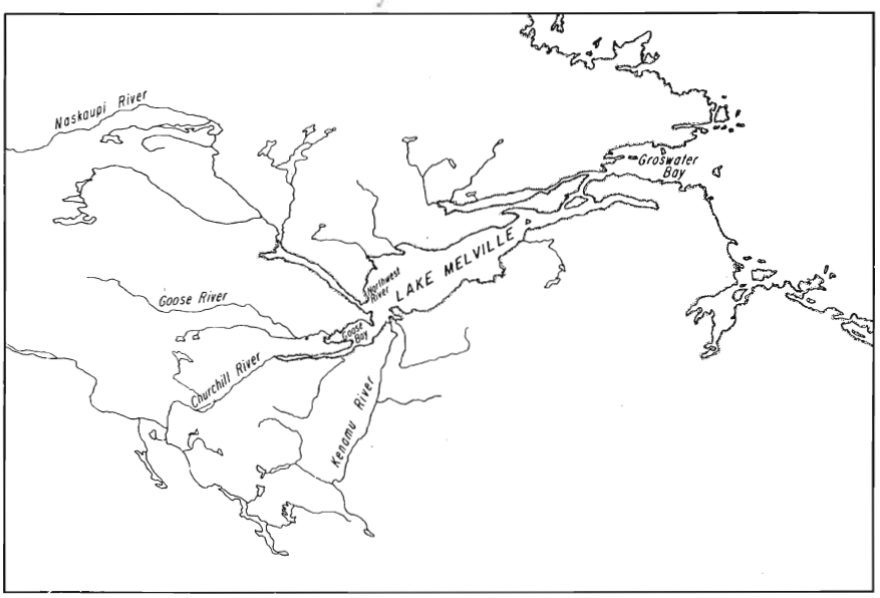

Figure 1.2: Major rivers flowing into Lake Melville.

Chapter 2

Measurements

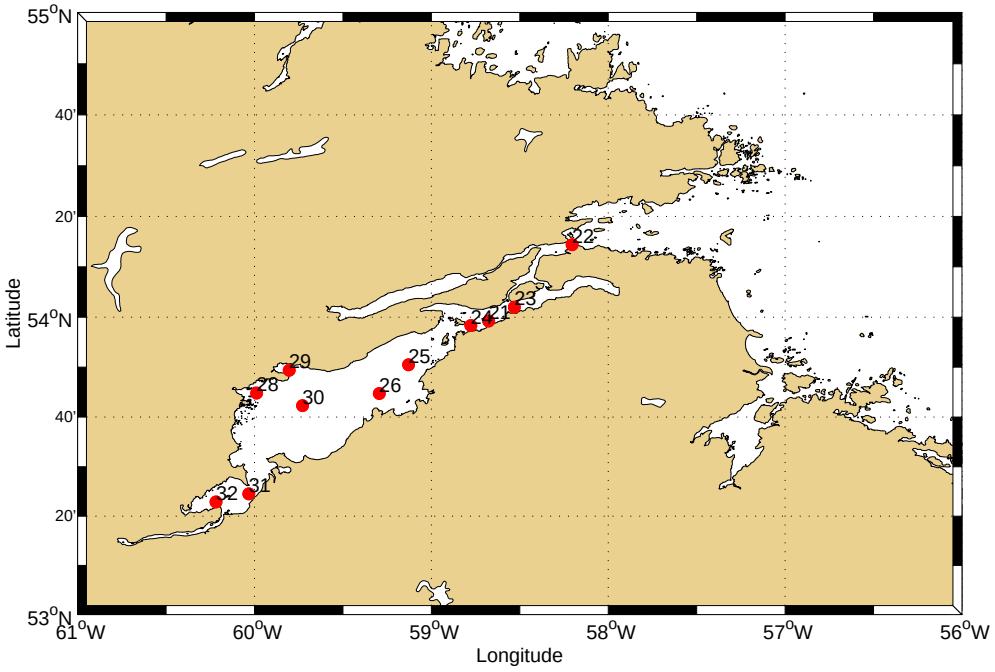

Figure 2.1: Hydrographic (CTD) casts surveys location in the Lake Melville.

To investigate the exchange dynamics of the system near the Narrows of the Lake Melville, mooring measurements were performed at two stations. The locations of the instruments deployed are shown in Figure 1.1. Current data was collected with RDI Acoustic Doppler current profilers (ADCPs), at sites M1 and M2. At the mooring station M1, which is inside the lake, the water depth is

192 m. As the measurements range for RDI ADCP is about 100 m from the sensors, two ADCPs were placed in the middle of the water column, with one ADCP moored at 96 meters above bottom looking upward and another moored at 96.9 m above bottom looking downward. At mooring station M2 outside the lake, which is about 106 m in water depth, one RDI ADCP was moored about 6.4 m above the bottom looking upward. All three ADCPs measured currents over the water column at 2 m spatial intervals and 30 minute temporal intervals. Current measurements were taken from September 8th, 2012 to June 15th, 2013. The instruments were all RDI 4 beam Workhorse Broadband ADCPs working at 300 kHz frequency. All ADCPs were configured to collected data at the same 30 minutes temporal interval.

Water temperature data were collected with Vemco loggers thermistors mounted on each mooring. At station M1, thermistors was mounted at depths of 15, 25, 35, 50, 75, 96, 150, and 175 m. At station M2, thermistors was mounted at depths of 25, 35, 50 and 75 m. All thermistors collected data at the same 1 minutes temporal interval.

Hydrographic data, specifically temperature, salinity and density profiles, were collected from casts surveys made at about 27 stations from from June 15 to July 3, 2013(see Figure 2.1).

A summary of mooring instruments and CTD casts is given in Tables 2.1, 2.2 and 2.3.

Table 2.1: Location and details of 2013 ADCP moorings.

Mooring	Latitude	Longitude	Depth (m)	Averaging Period	Bin Size
M1	53°59.234′N	058°40.527′W	192 m	30 Minutes	2 m
M2	54°14.410′N	058°12.200′W	106 m	30 Minutes	2 m

Table 2.2: Location and details of 2013 CTD casts, June 15 to June 17.

Cast #	Time	Latitude	Longitude	Depth (m)
LM_CTD_21	06-15-13	53°59.234′N	58°40.527′W	185 m
LM_CTD_22	06-15-13	54°14.410′N	58°12.20′W	100 m
LM_CTD_23	06-16-13	54°01.971′N	58°31.797′W	183 m
LM_CTD_24	06-16-13	53°58.334′N	58°46.611′W	174 m
LM_CTD_25	06-16-13	53°50.499′N	59°07.7118′W	200 m
LM_CTD_26	06-16-13	53°44.726′N	59°17.627′W	206 m
LM_CTD_28	06-17-13	53°44.835′N	59°59.229′W	50 m
LM_CTD_29	06-17-13	53°49.387′N	59°48.206′W	53 m
LM_CTD_30	06-17-13	53°42.295′N	59°43.707′W	82 m
LM_CTD_31	06-17-13	53°24.526′N	60°01.867′W	49 m
LM_CTD_32	06-17-13	53°22.900′N	60°12.995′W	47 m

Table 2.3: Location and details of 2013 CTD casts, June 19 to July 03.

Cast #	Time	Latitude	Longitude	Depth (m)
LM1_170_6220	06-19-13 09:21 AM	53° 37.91 ′N	59° 52.89 ′W	28
LM2_170_6274	06-19-13 07:31 PM	53° 37.57 ′N	59° 42.05 ′W	54
LM3_171_12340	06-20-13 09:40 AM	53° 48.47 ′N	59° 07.75 ′W	181
LM3_171_20432	06-20-13 09:40 AM	53° 37.82 ′N	59° 33.60 ′W	128
LM4_171_29892	06-20-13 09:40 AM	53° 40.87 ′N	59° 27.02 ′W	165
LM5_172_12646	06-21-13 09:44 AM	53° 48.22 ′N	59° 07.86 ′W	184
LM6_172_11454	06-21-13 06:10 PM	53° 43.22 ′N	59° 22.52 ′W	158
LM6_173_24344	06-21-13 06:10 PM	53° 48.45 ′N	59° 08.47 ′W	184
LM7_174_10972	06-23-13 05:54 PM	53° 49.53 ′N	59° 09.40 ′W	129
LM7_174_27338	06-21-13 06:10 PM	53° 39.65 ′N	59° 35.80 ′W	33
LM8_175_5194	06-24-13 10:19 AM	53° 41.50 ′N	59° 37.83 ′W	86
LM9_175_4294	06-24-13 06:39 PM	53° 46.21 ′N	59° 20.21 ′W	79
LM10_176_11616	06-25-13 09:45 AM	53° 50.13 ′N	59° 09.47 ′W	171
LM11_176_5194	06-25-13 09:33 PM	53° 40.79 ′N	59° 36.78 ′W	84
LM12_177_5734	06-26-13 10:21 AM	53° 40.72 ′N	59° 37.20 ′W	81
LM13_177_8628	06-26-13 05:24 PM	53° 50.98 ′N	59° 11.32 ′W	148
LM14_178_8146	06-27-13 09:45 AM	53° 51.09 ′N	59° 11.21 ′W	139
LM15_17_8290	06-27-13 05:40 PM	53° 45.56 ′N	59° 27.71 ′W	148
LM16_179_5752	06-28-13 10:24 AM	53° 41.36 ′N	59° 38.16 ′W	93
LM17_179_9154	06-28-13 06:53 PM	53° 45.52 ′N	59° 29.36 ′W	148
LM18_180_14212	06-29-13 09:40 AM	53° 50.08 ′N	59° 10.13 ′W	196
LM19_181_4762	06-30-13 09:57 AM	53° 42.66 ′N	59° 38.85 ′W	66
LM20_181_6778	06-30-13 05:20 PM	53° 52.47 ′N	59° 12.98 ′W	119
LM21_182_5734	07-01-13 10:12 AM	53° 41.76 ′N	59° 40.21 ′W	75
LM22_182_5954	07-01-13 06:33 PM	53° 49.43 ′N	59° 22.21 ′W	76
LM23_183_2530	07-02-13 11:14 AM	53° 27.11 ′N	59° 57.45 ′W	18
LM24_183_3768	07-02-13 06:30 PM	53° 24.82 ′N	60° 01.50 ′W	39
LM25_184_2350	07-03-13 09:27 AM	53° 21.09 ′N	60° 20.50 ′W	17
LM26_184_2530	07-03-13 11:55 AM	53° 21.17 ′N	60° 20.64 ′W	18
LM27_184_4250	07-03-13 11:55 AM	53° 20.99 ′N	60° 21.94 ′W	17

Chapter 3

Plots of raw data records

In this section, figures of raw instruments records are presented, including time series plots of selected ADCP depths, thermistors records, and vertical profiles plots of CTD casts.

3.1 ADCPs records

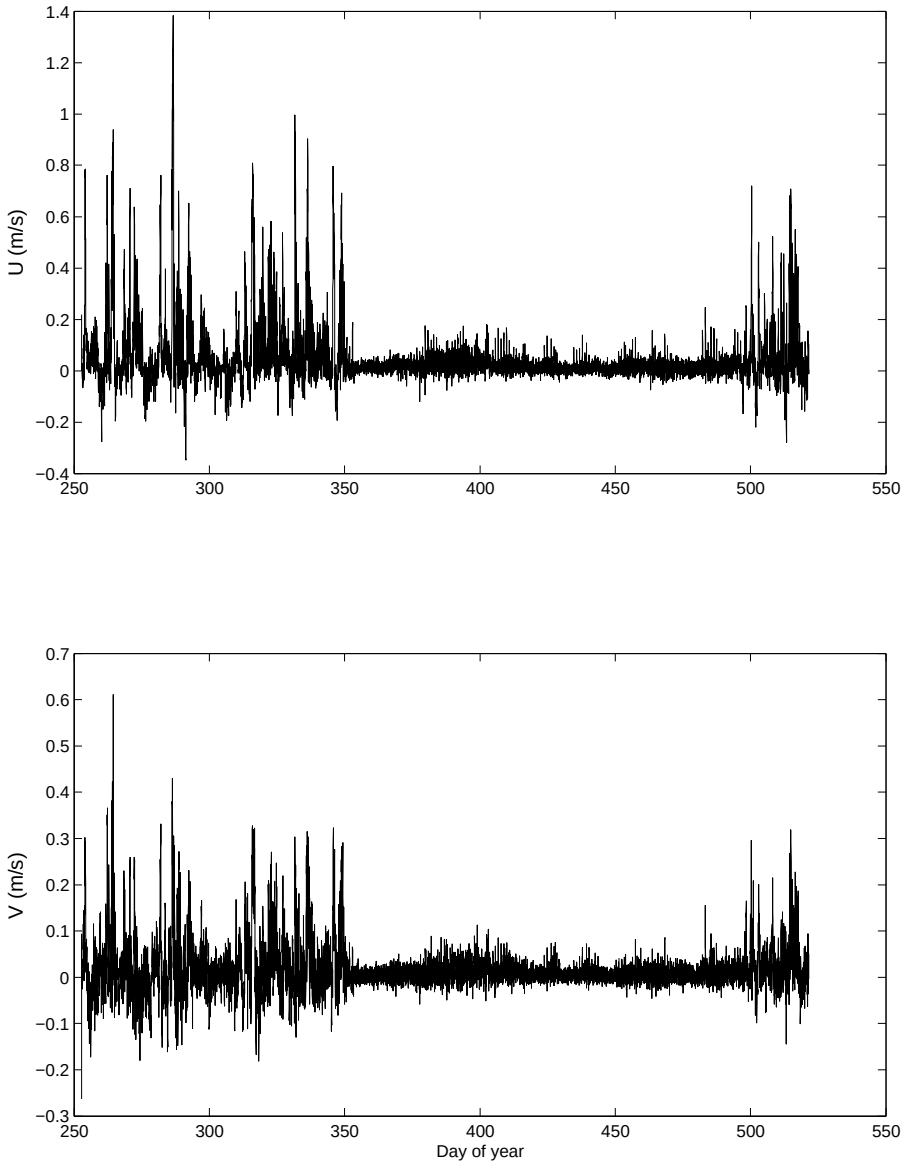

Figure 3.1: Time series plot of ADCP records at 10 m, M1.

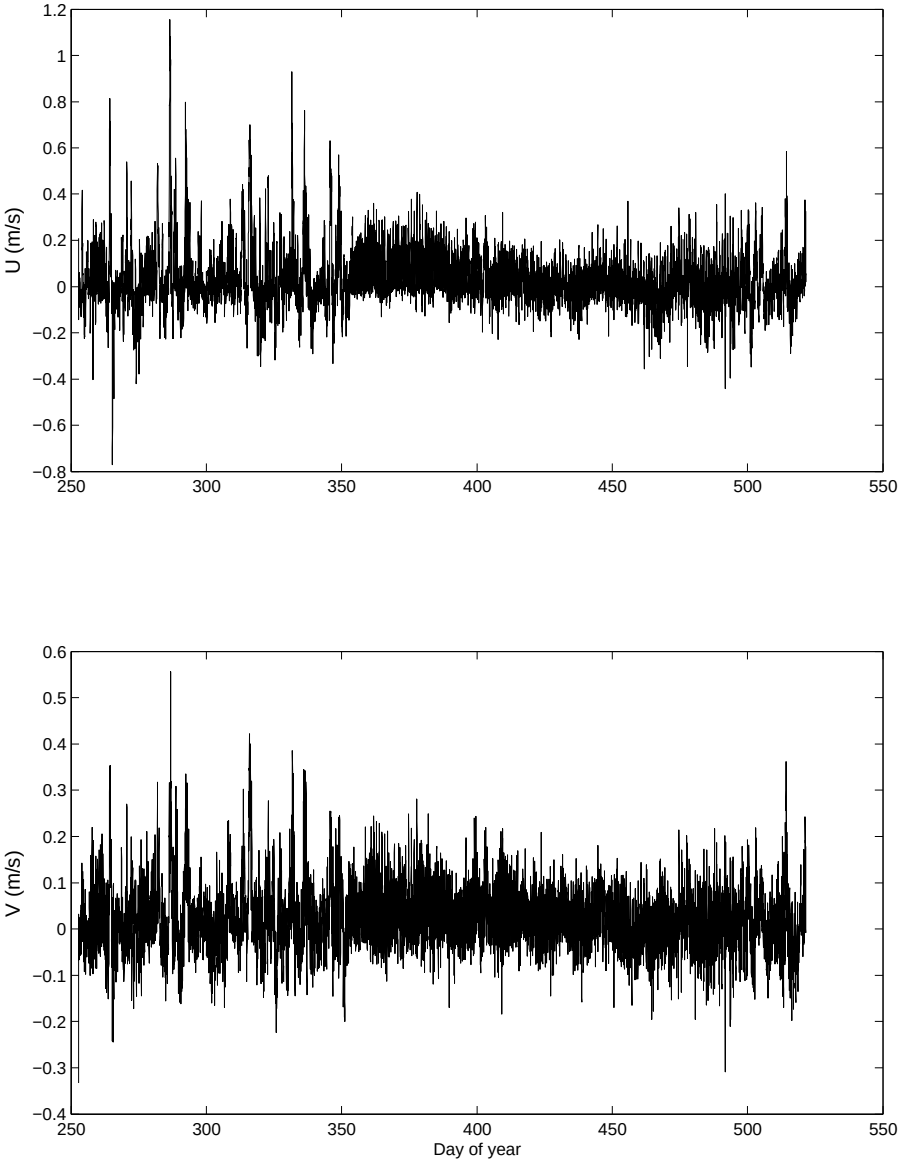

Figure 3.2: Time series plot of ADCP records at 20 m, M1.

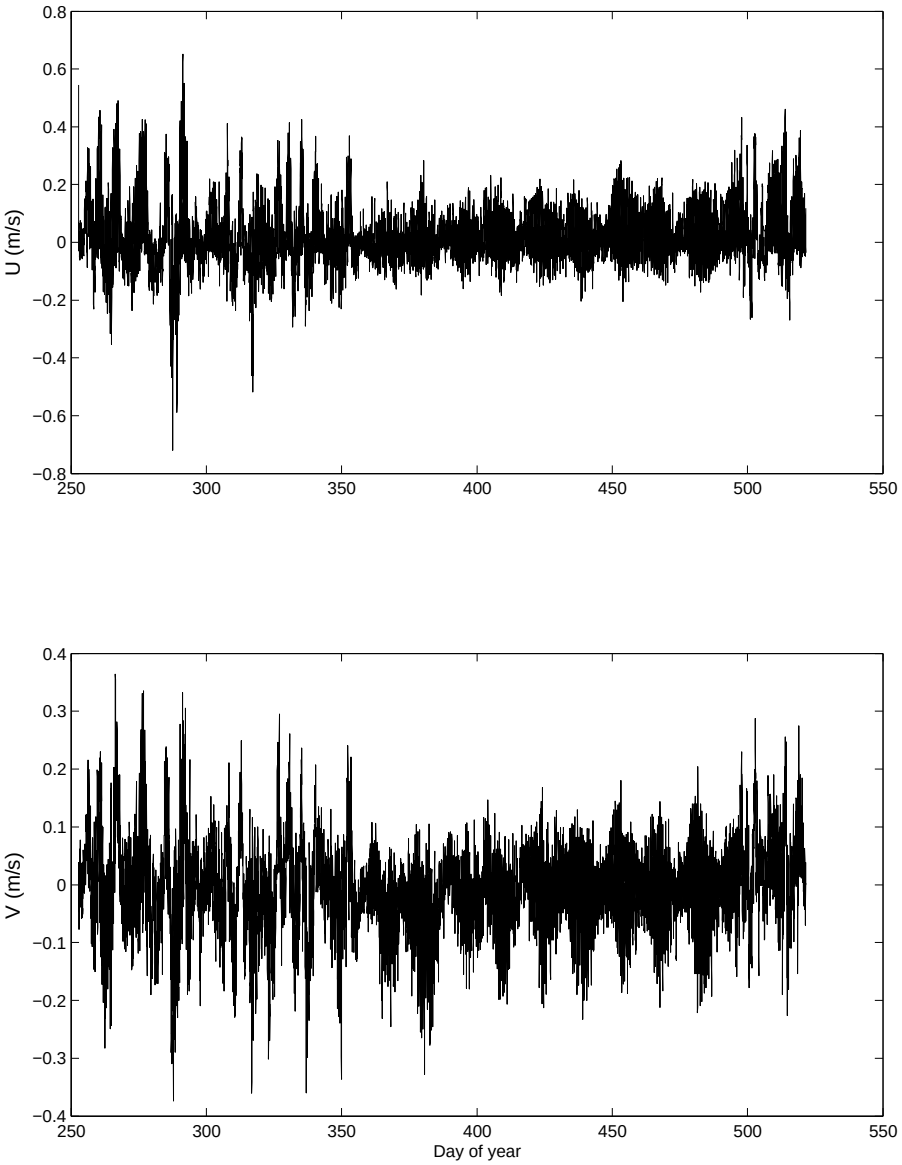

Figure 3.3: Time series plot of ADCP records at 50 m, M1.

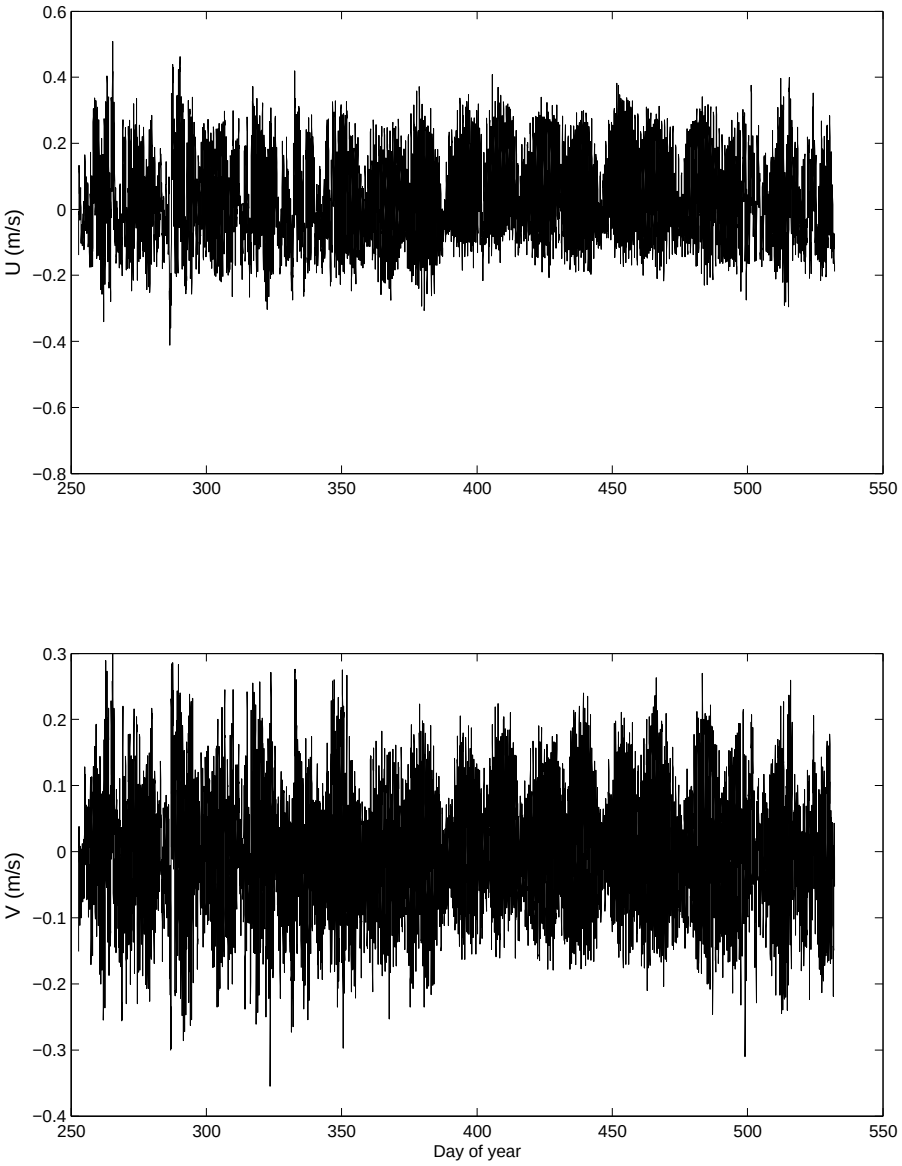

Figure 3.4: Time series plot of ADCP records at 100 m, M1.

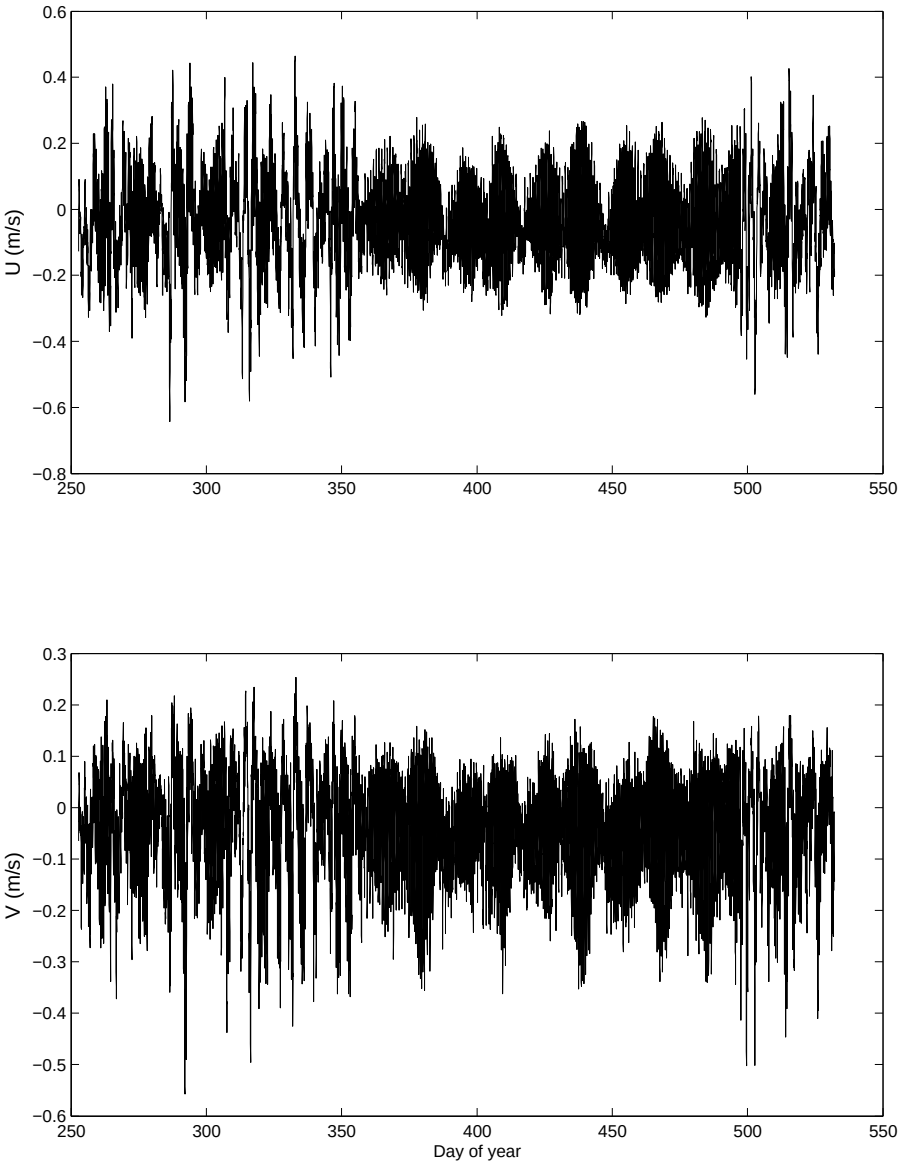

Figure 3.5: Time series plot of ADCP records at 150 m, M1.

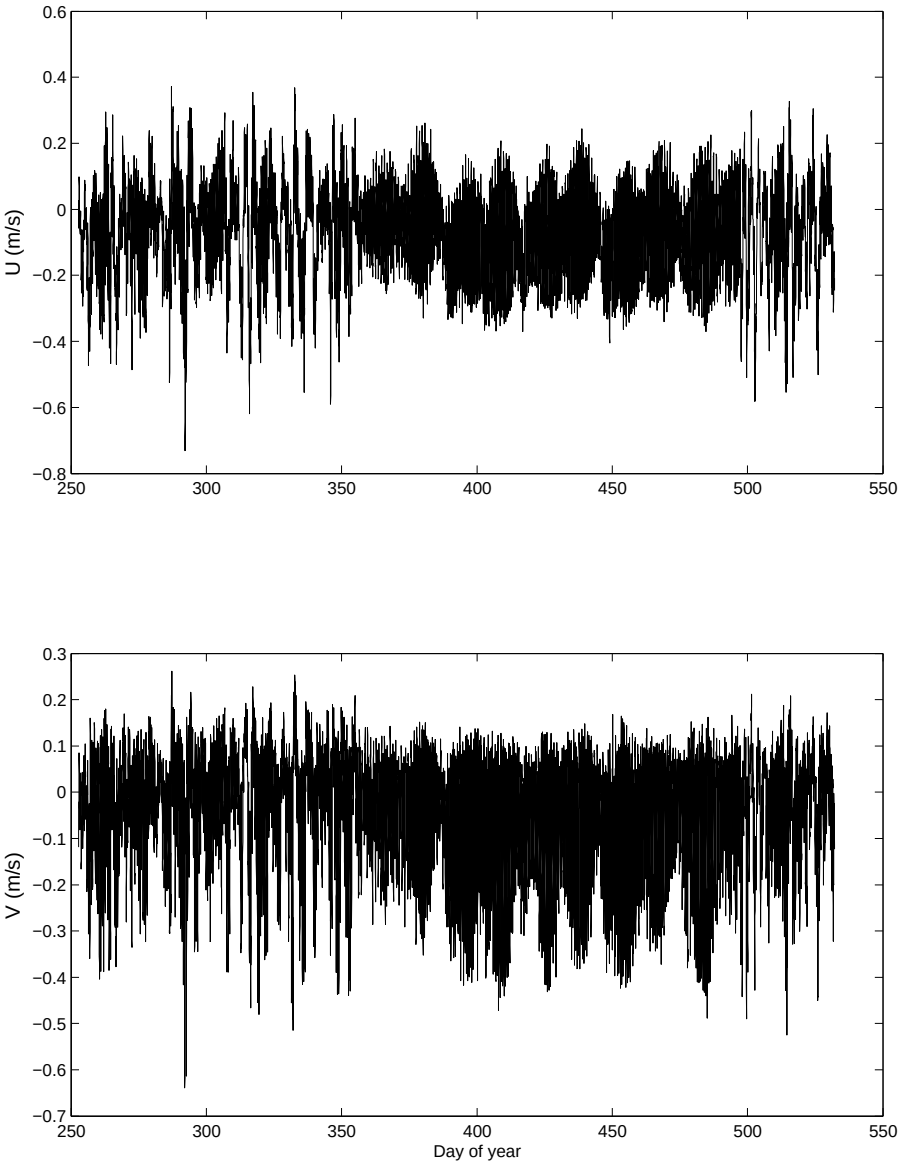

Figure 3.6: Time series plot of ADCP records at 175 m, M1.

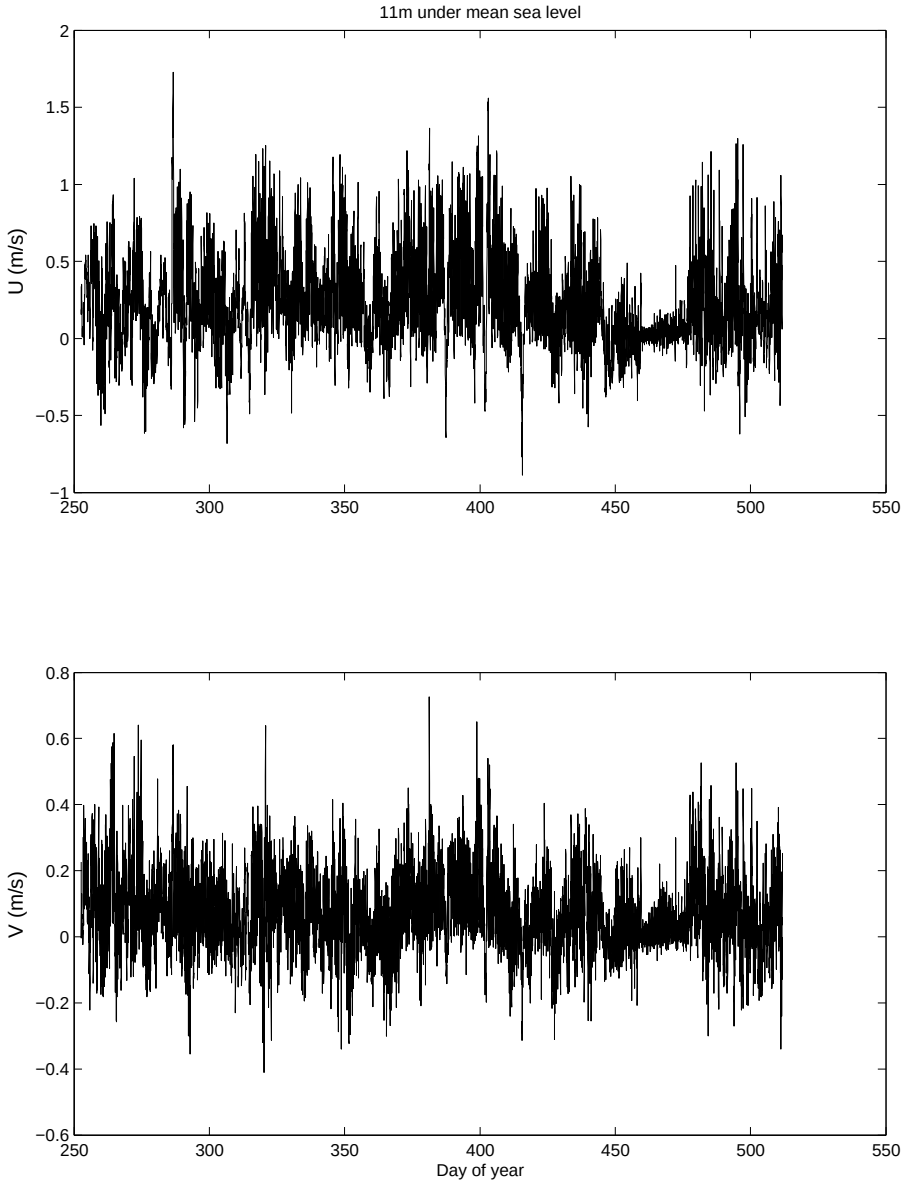

Figure 3.7: Time series plot of ADCP records at 10 m, M2.

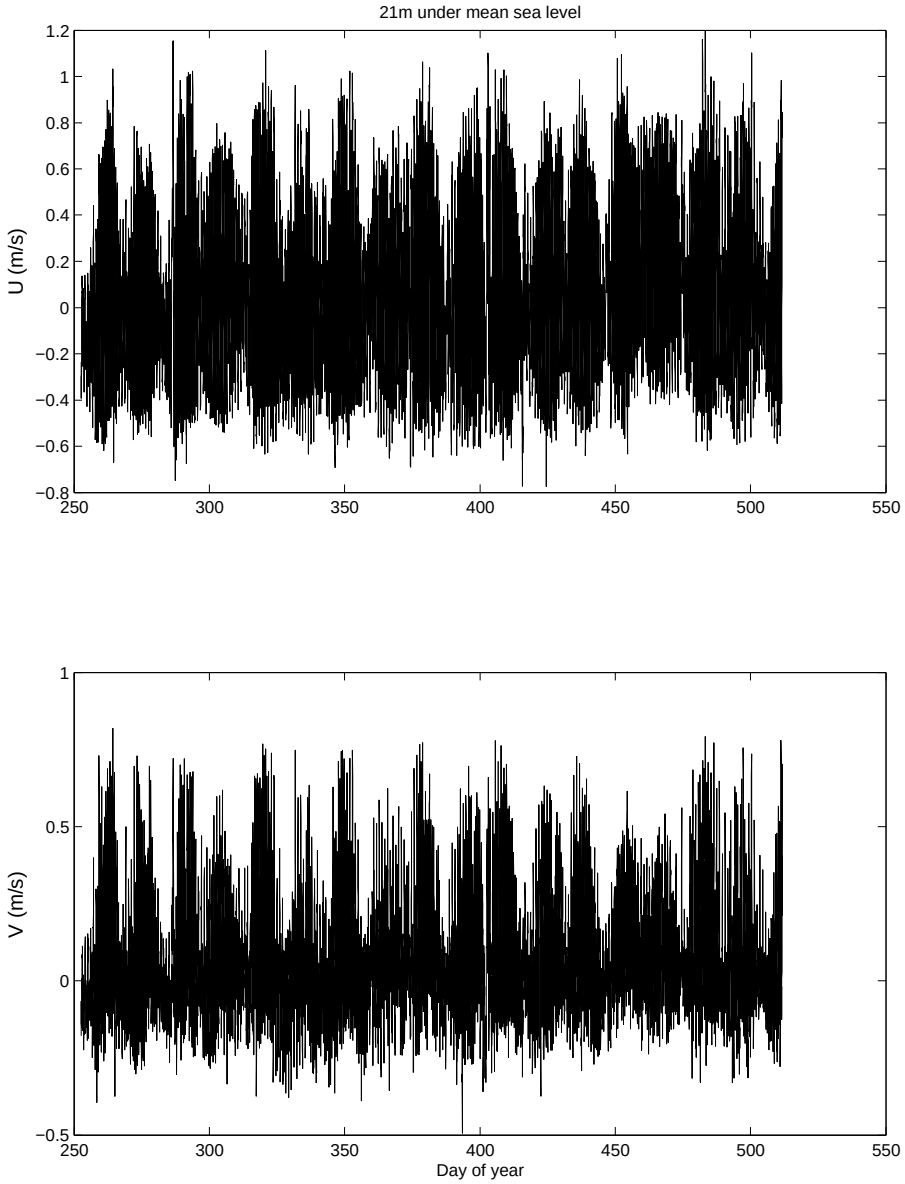

Figure 3.8: Time series plot of ADCP records at 20 m, M2.

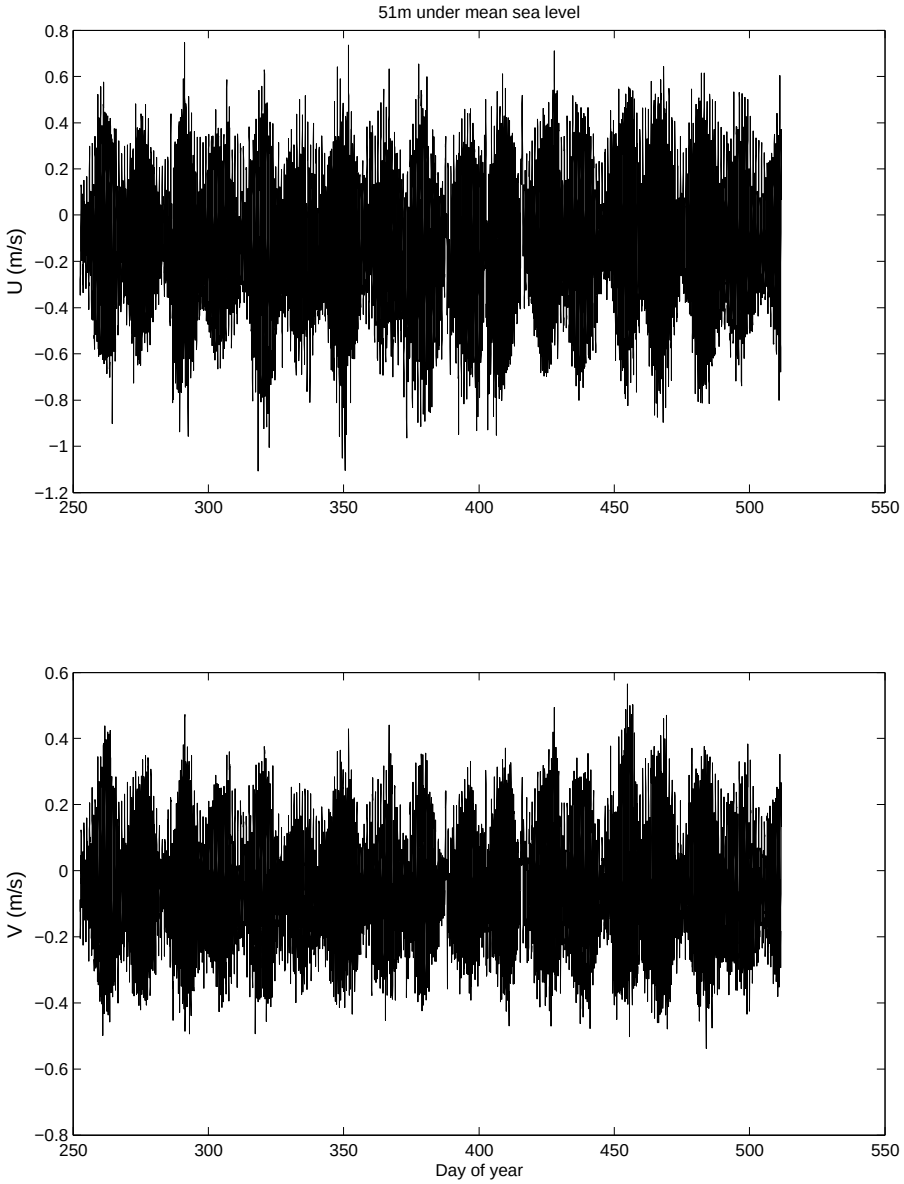

Figure 3.9: Time series plot of ADCP records at 50 m, M2.

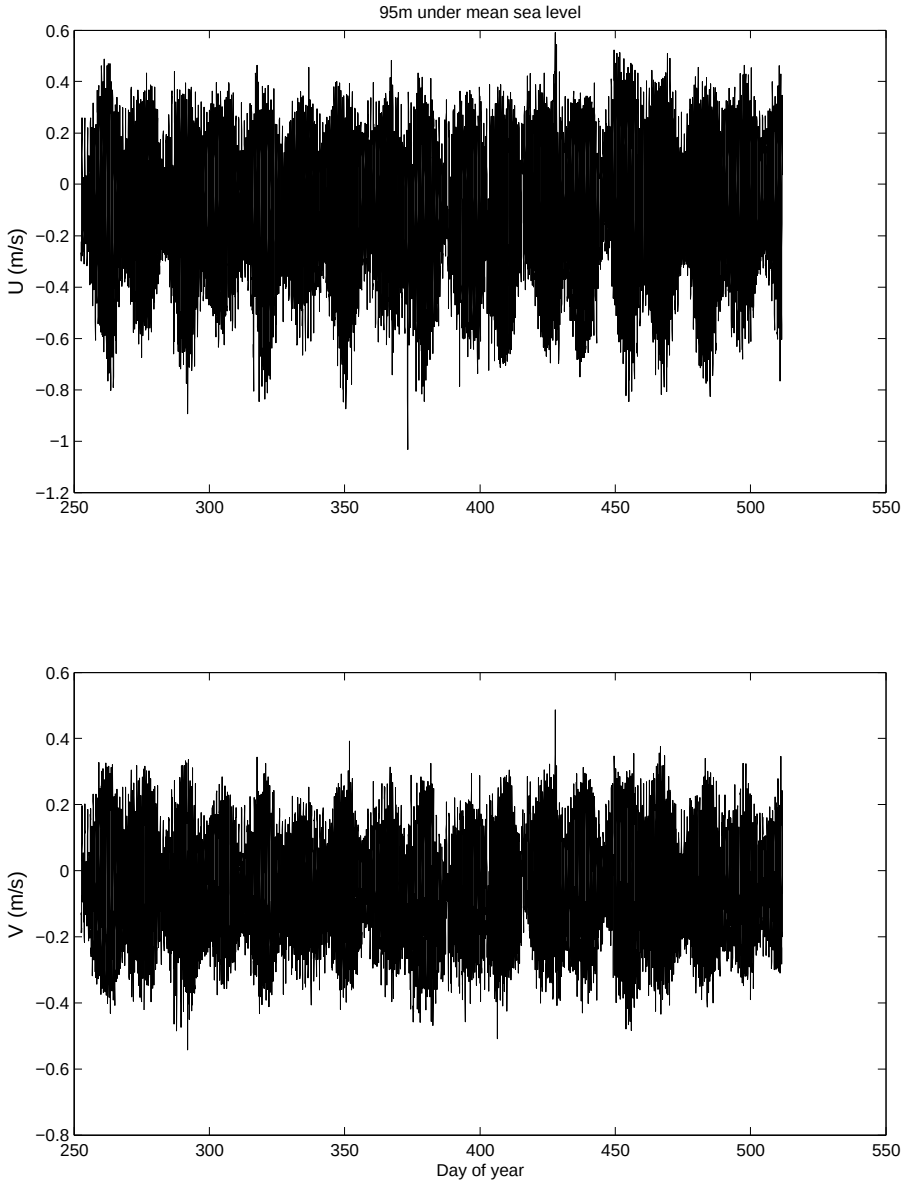

Figure 3.10: Time series plot of ADCP records at 100 m, M2.

3.2 Thermistors records

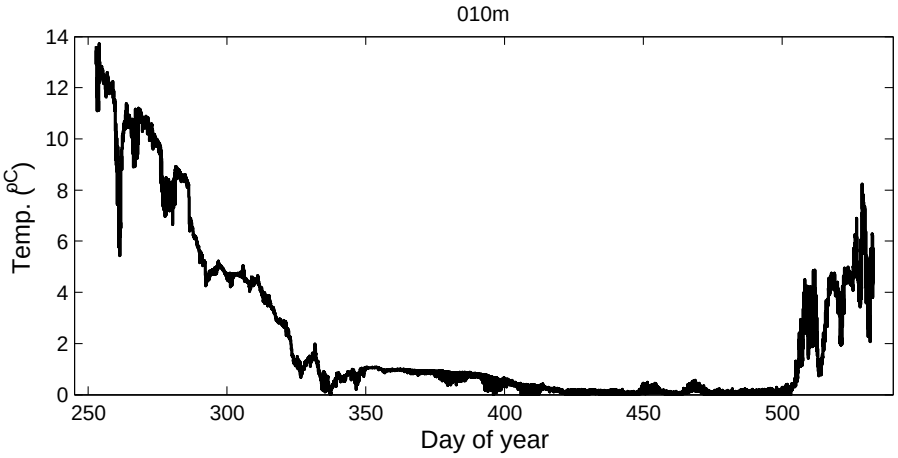

Figure 3.11: Time series plot of thermistors records at 10 m, M1.

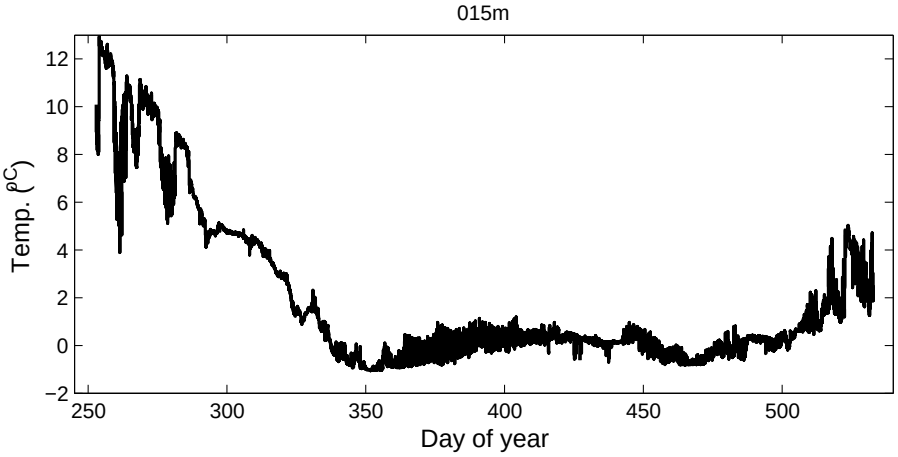

Figure 3.12: Time series plot of thermistors records at 15 m, M1.

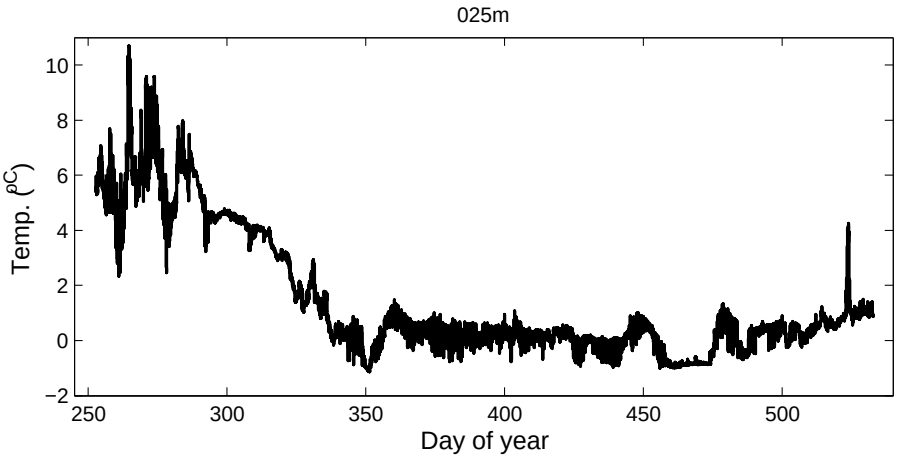

Figure 3.13: Time series plot of thermistors records at 25 m, M1.

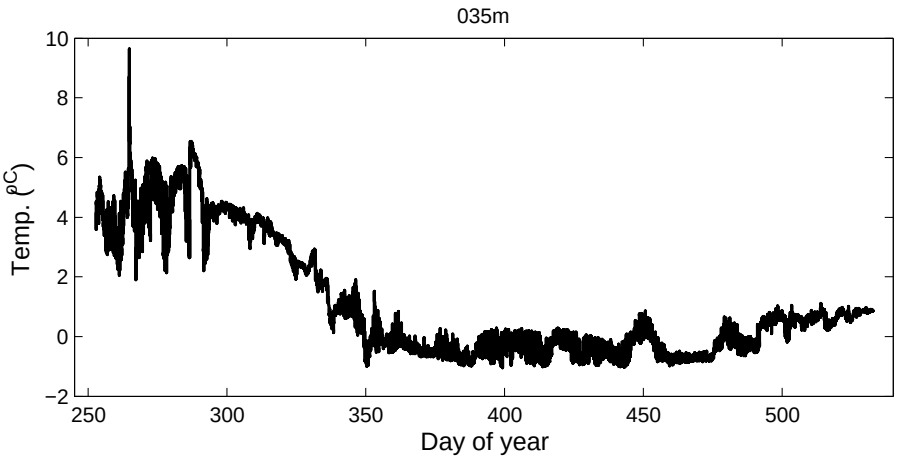

Figure 3.14: Time series plot of thermistors records at 35 m, M1.

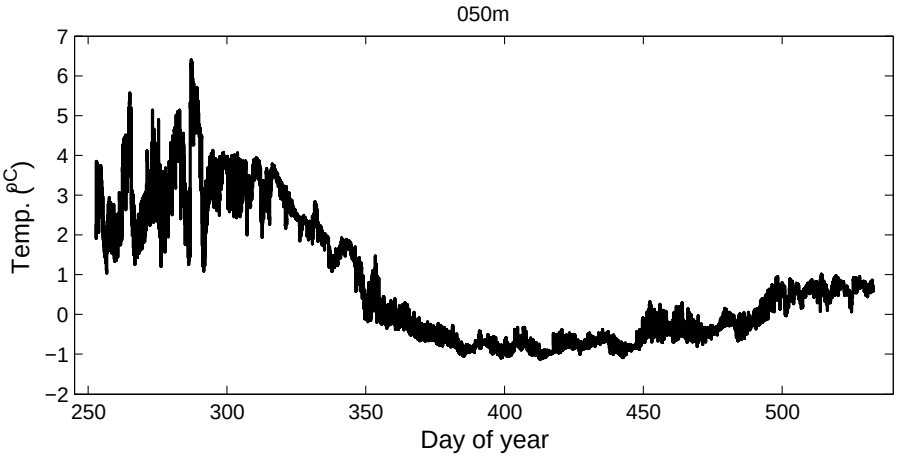

Figure 3.15: Time series plot of thermistors records at 50 m, M1.

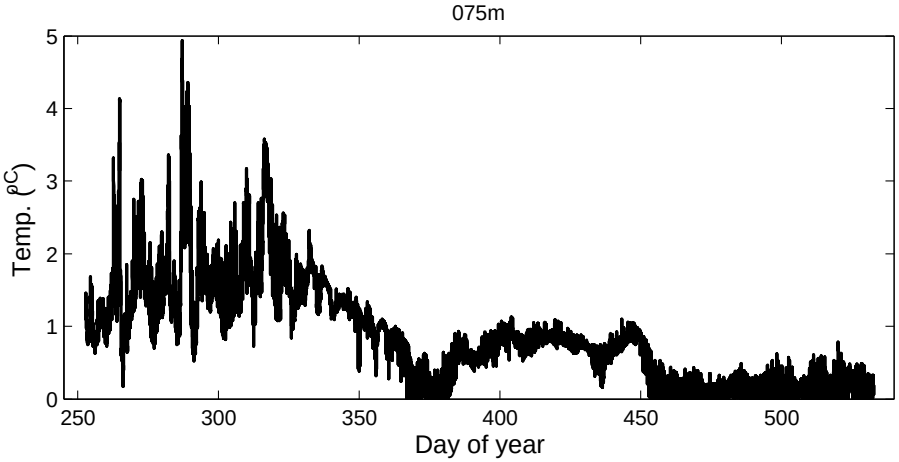

Figure 3.16: Time series plot of thermistors records at 75 m, M1.

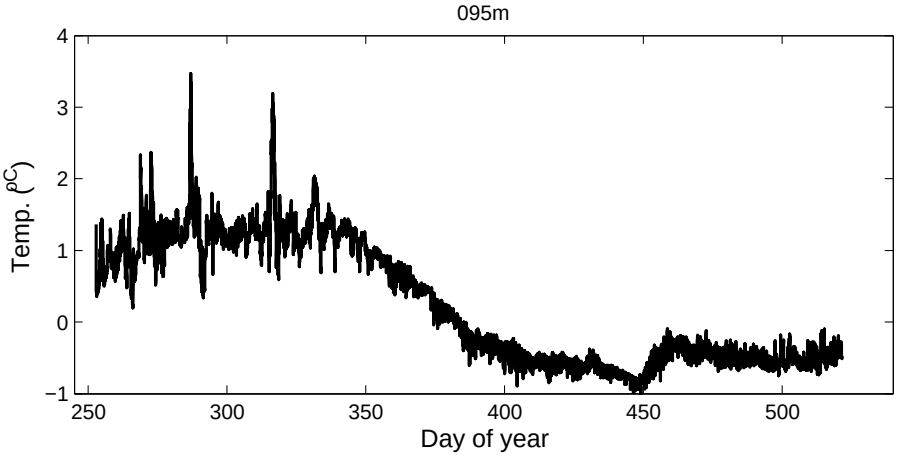

Figure 3.17: Time series plot of thermistors records at 95 m, M1.

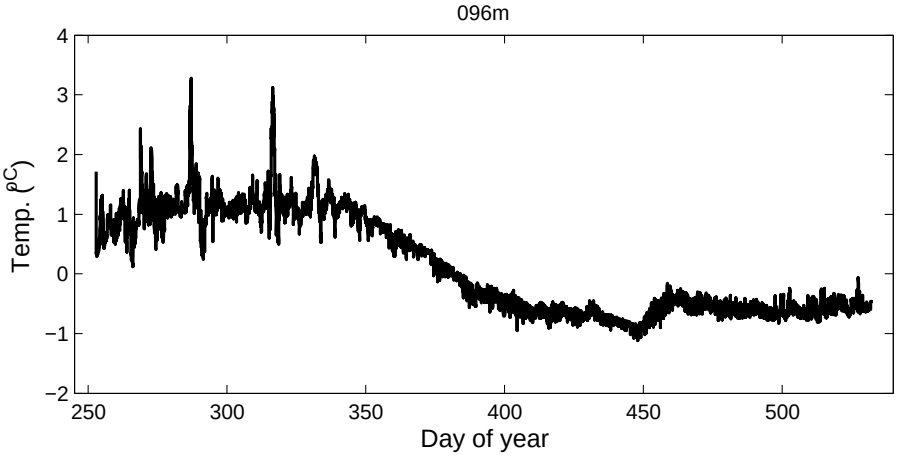

Figure 3.18: Time series plot of thermistors records at 96 m, M1.

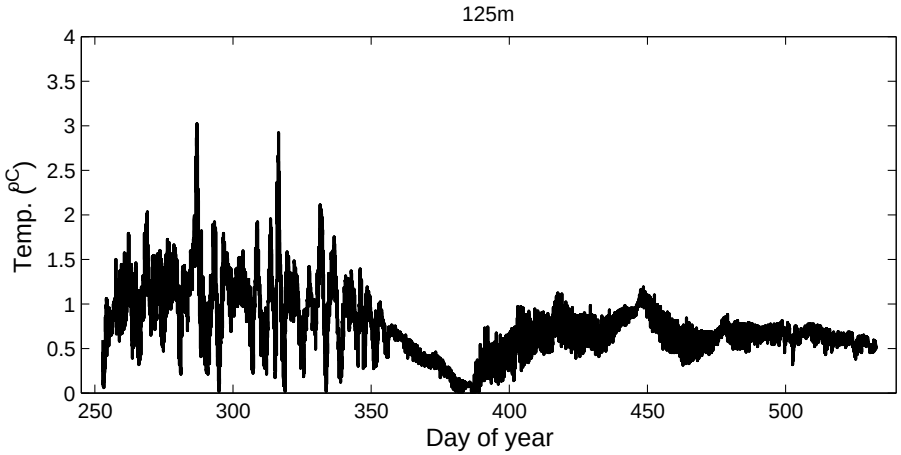

Figure 3.19: Time series plot of thermistors records at 125 m, M1.

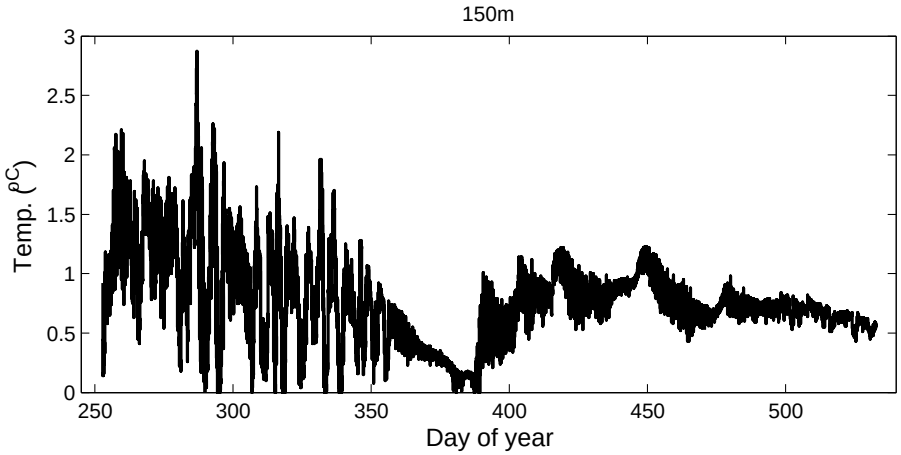

Figure 3.20: Time series plot of thermistors records at 150 m, M1.

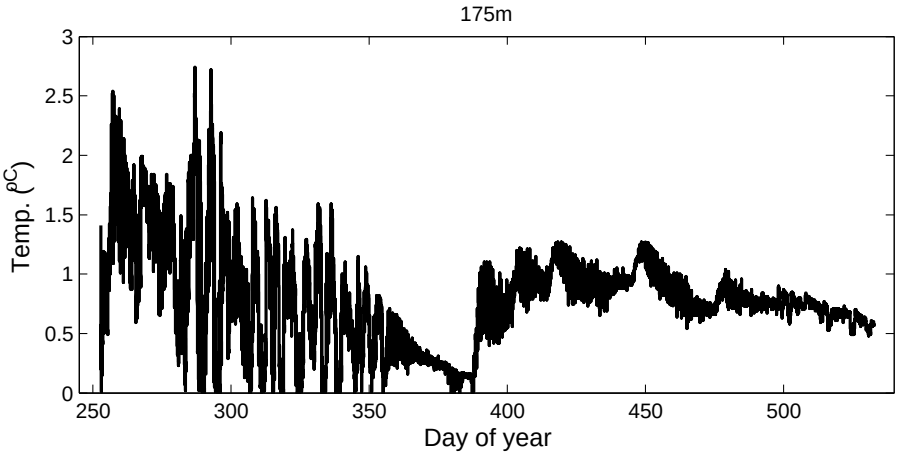

Figure 3.21: Time series plot of thermistors records at 175 m, M1.

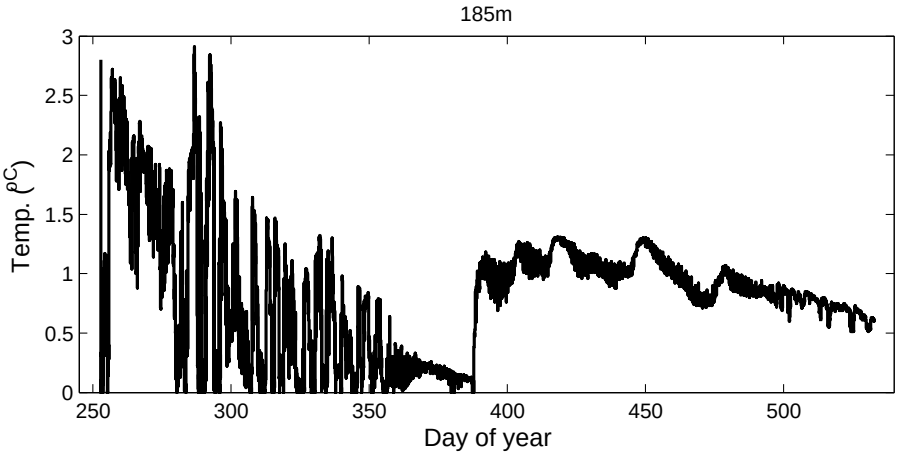

Figure 3.22: Time series plot of thermistors records at 185 m, M1.

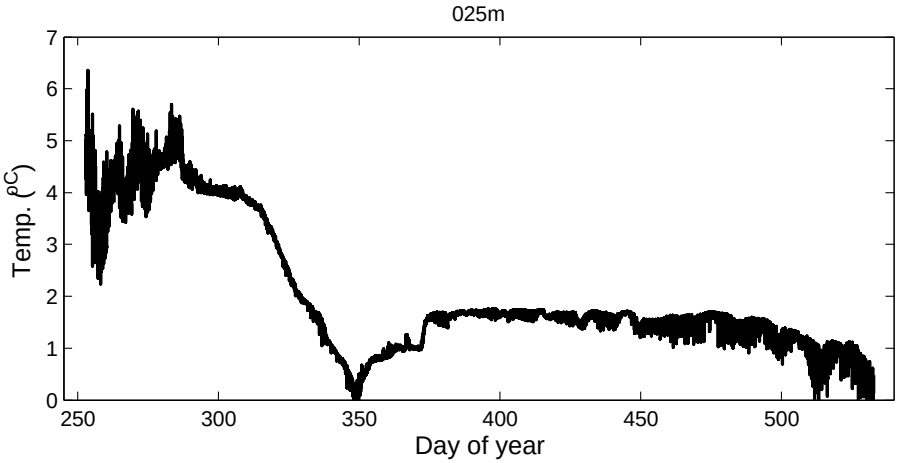

Figure 3.23: Time series plot of thermistors records at 25 m, M2.

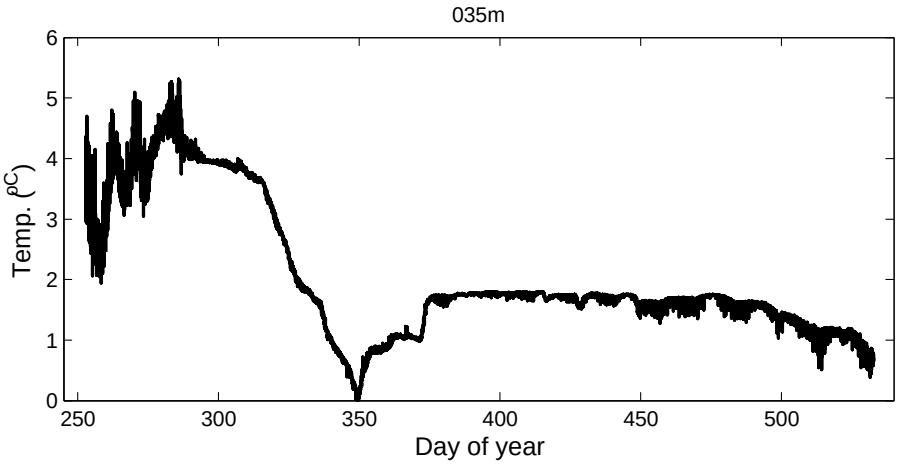

Figure 3.24: Time series plot of thermistors records at 35 m, M2.

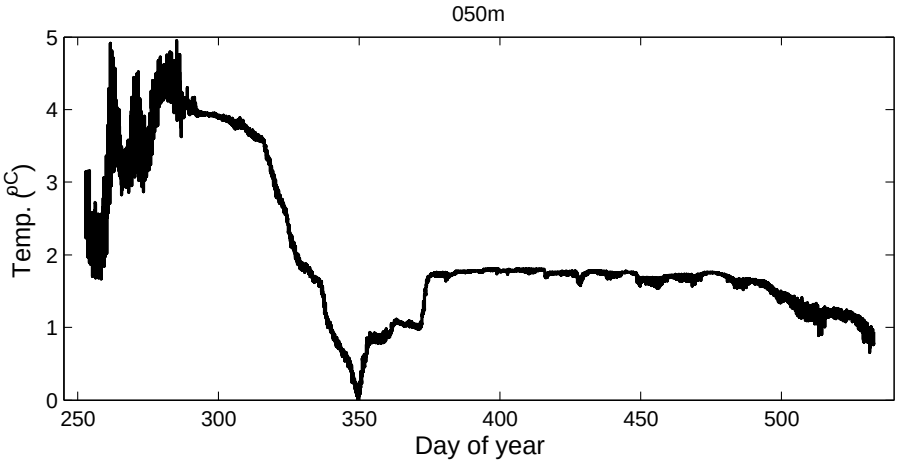

Figure 3.25: Time series plot of thermistors records at 50 m, M2.

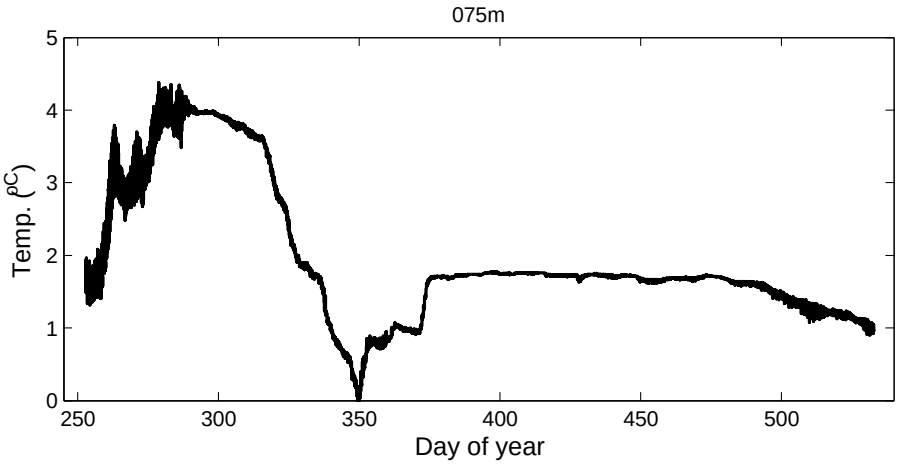

Figure 3.26: Time series plot of thermistors records at 75 m, M2.

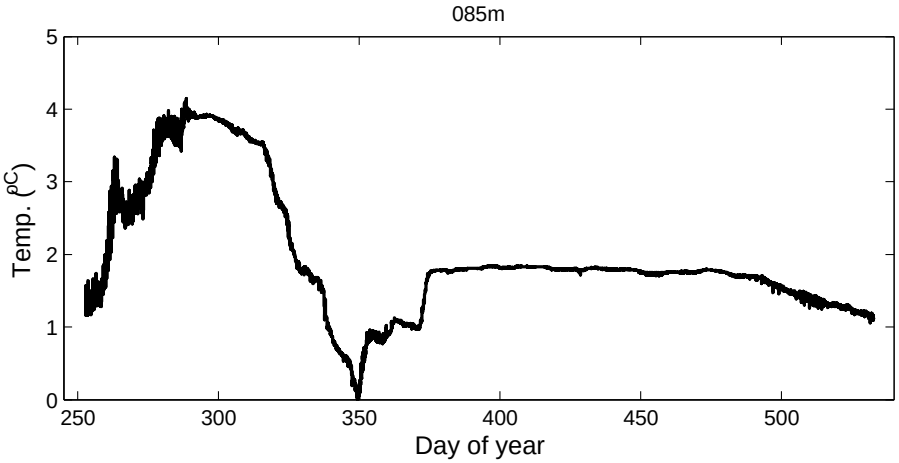

Figure 3.27: Time series plot of thermistors records at 85 m, M2.

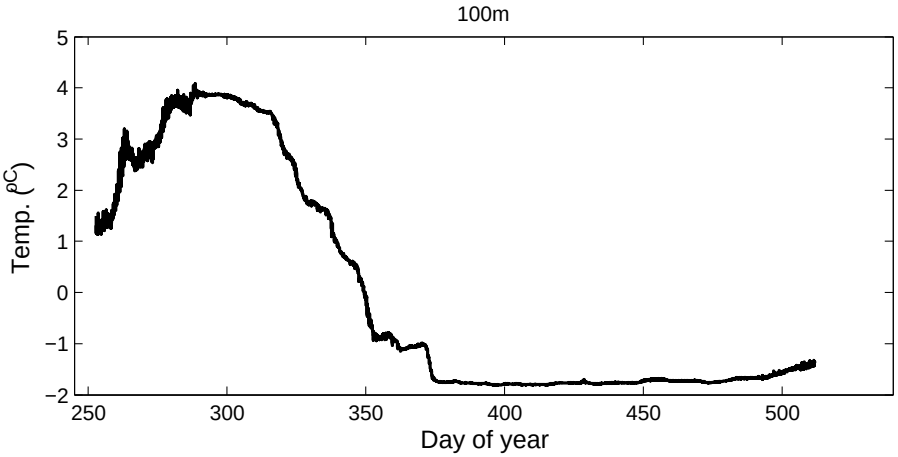

Figure 3.28: Time series plot of thermistors records at 100 m, M2.

3.3 CTDs records

3.3.1 CTD records, June 15 to June 17.

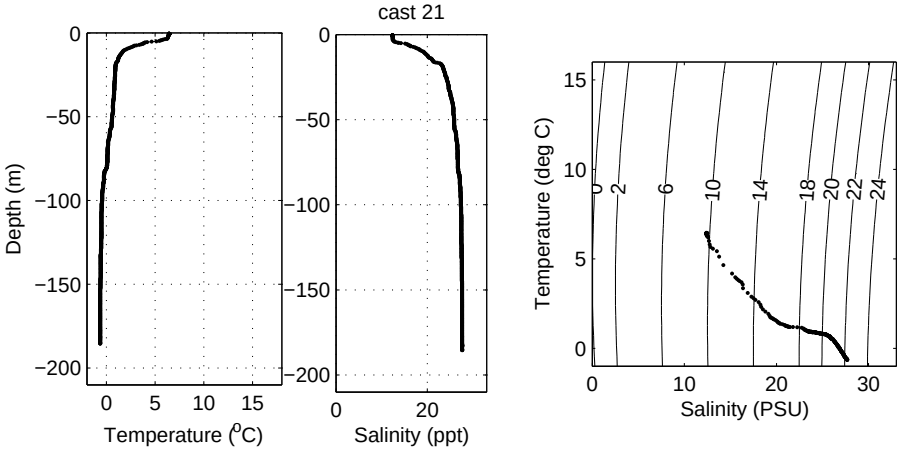

Figure 3.29: Profile of CTD cast 21.

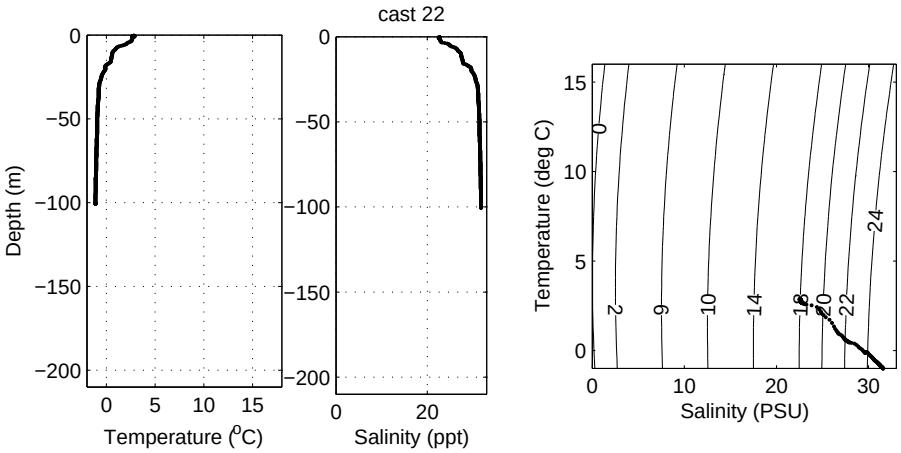

Figure 3.30: Profile of CTD cast 22.

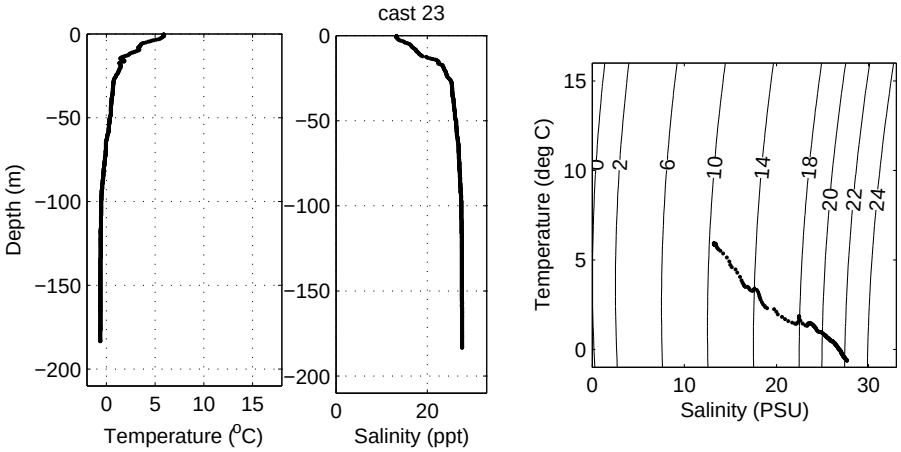

Figure 3.31: Profile of CTD cast 23.

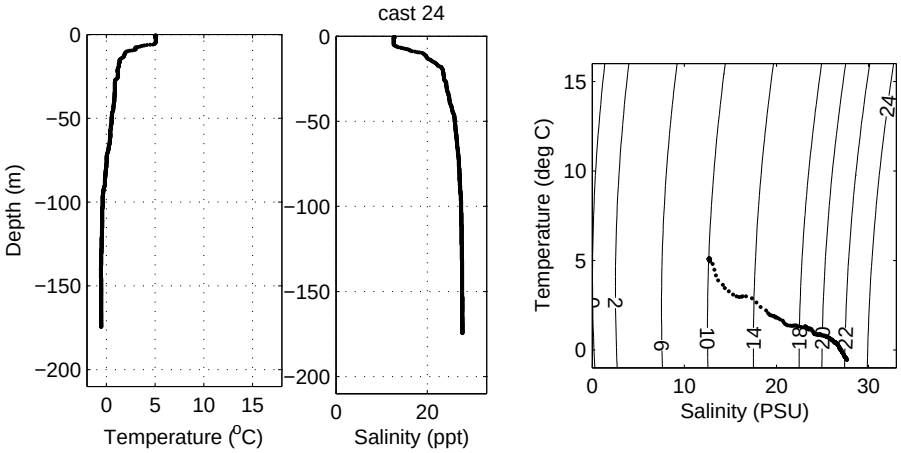

Figure 3.32: Profile of CTD cast 24.

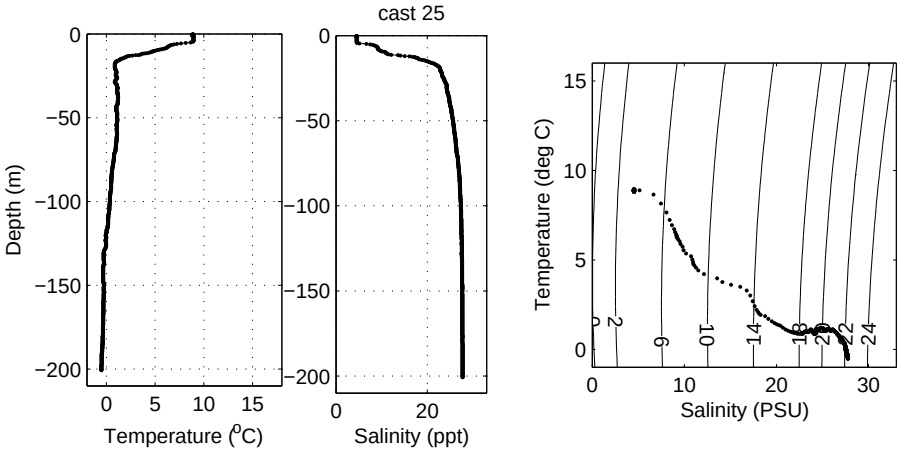

Figure 3.33: Profile of CTD cast 25.

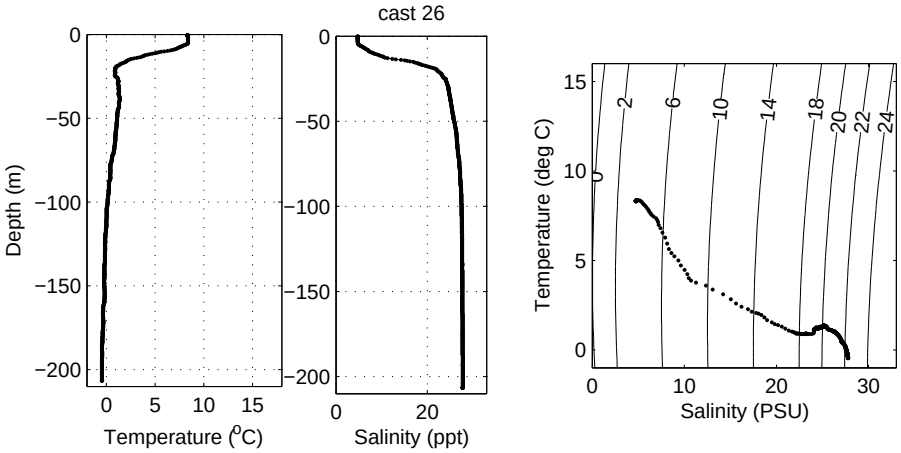

Figure 3.34: Profile of CTD cast 26.

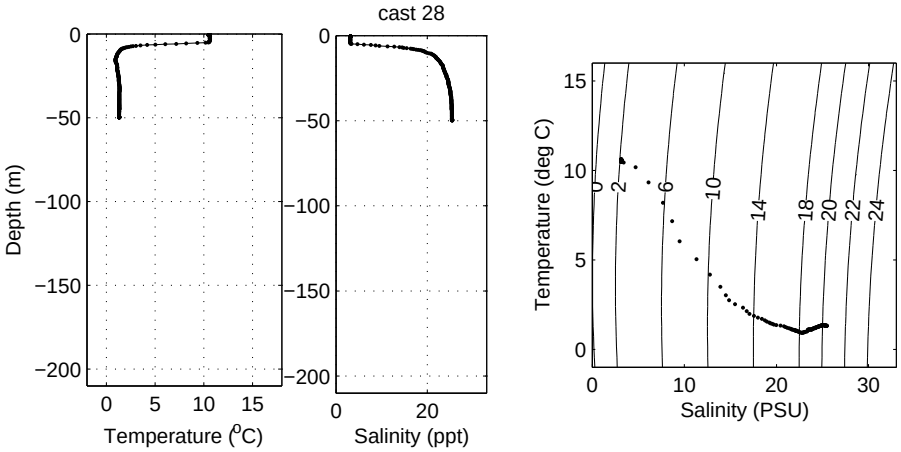

Figure 3.35: Profile of CTD cast 28.

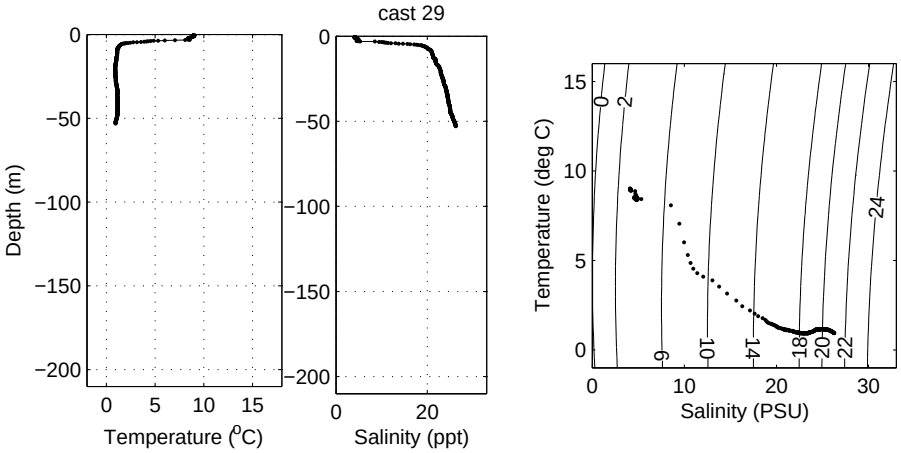

Figure 3.36: Profile of CTD cast 29.

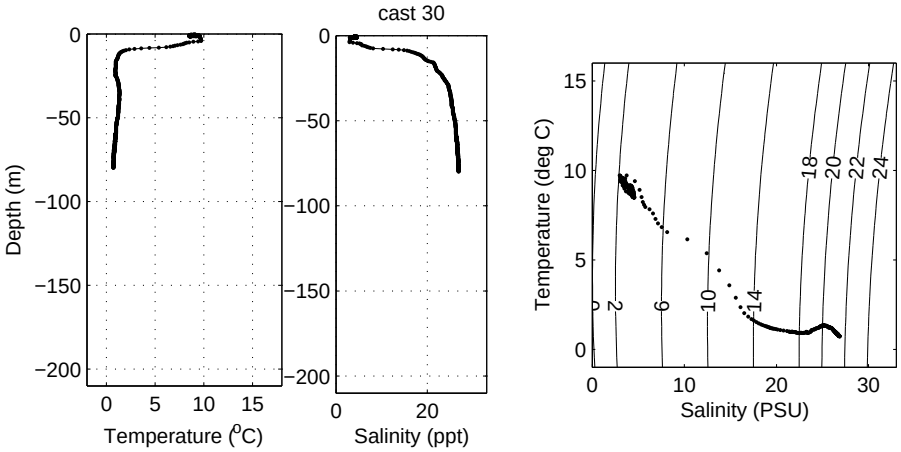

Figure 3.37: Profile of CTD cast 30.

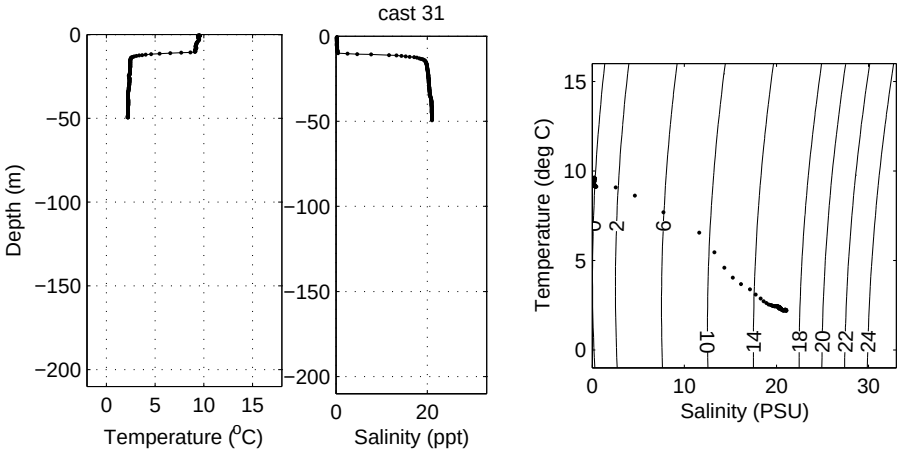

Figure 3.38: Profile of CTD cast 31.

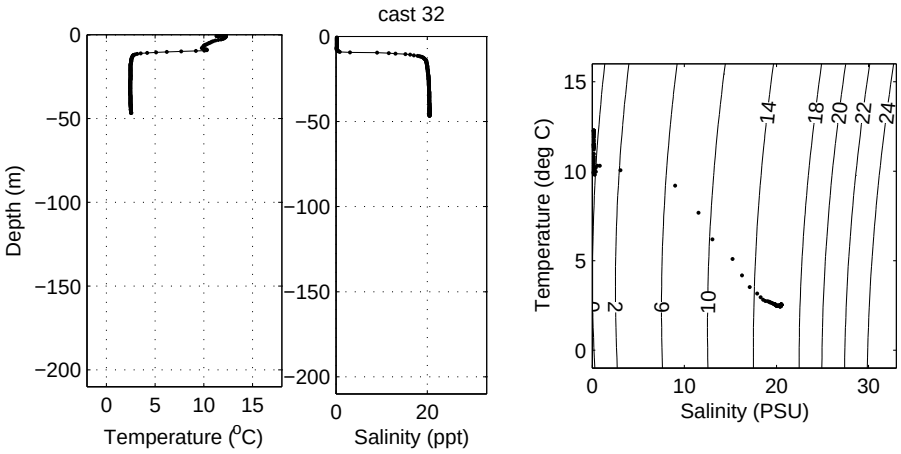

Figure 3.39: Profile of CTD cast 32.

3.3.2 CTD records, June 19 to July 03.

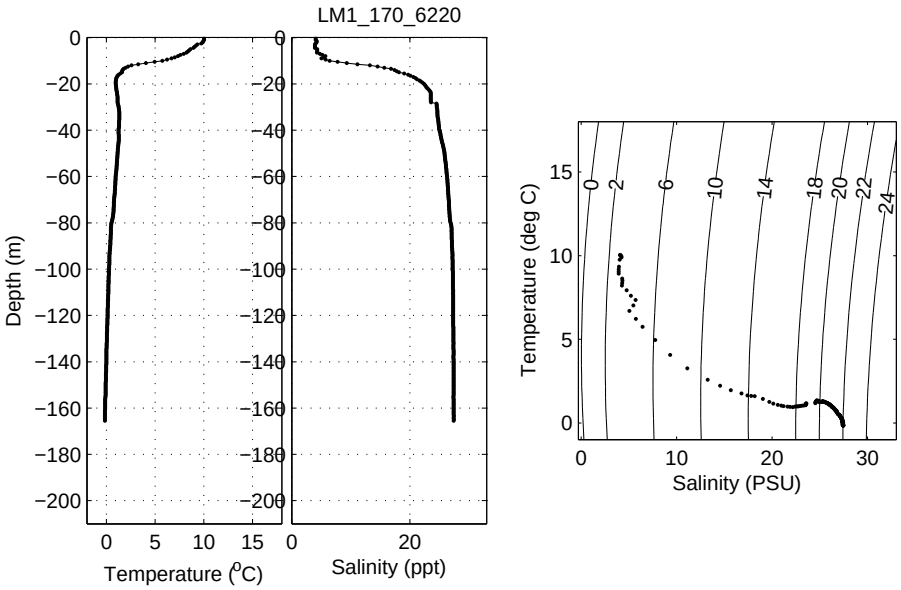

Figure 3.40: Profile of CTD cast JD170_LM1_170_6220.

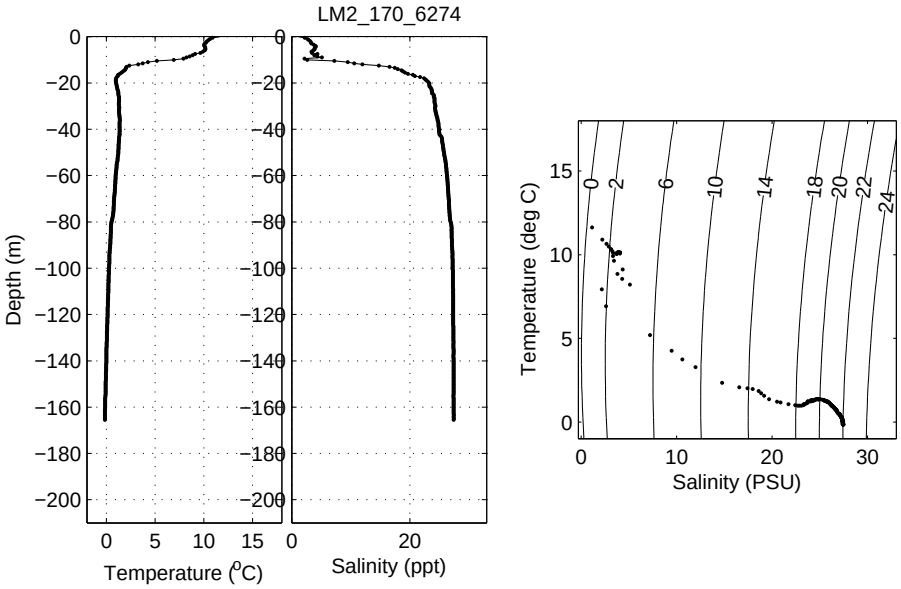

Figure 3.41: Profile of CTD cast JD170_LM2_170_6274.

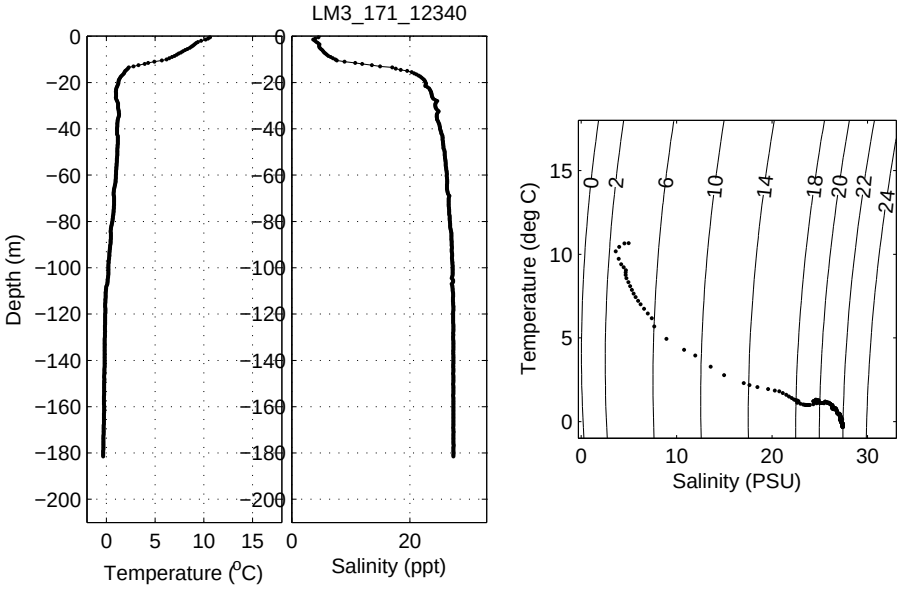

Figure 3.42: Profile of CTD cast JD171_LM3_171_12340.

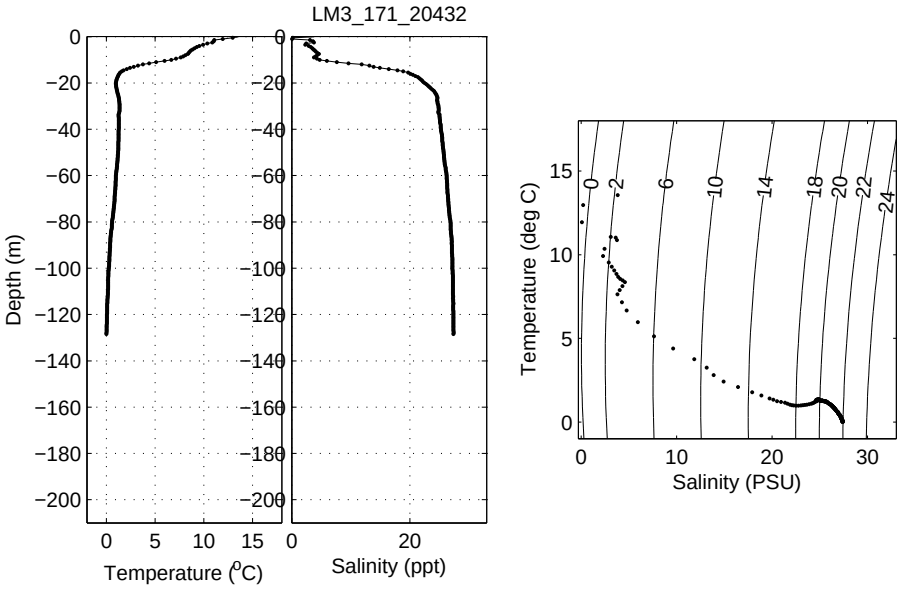

Figure 3.43: Profile of CTD cast JD171_LM3_171_20432.

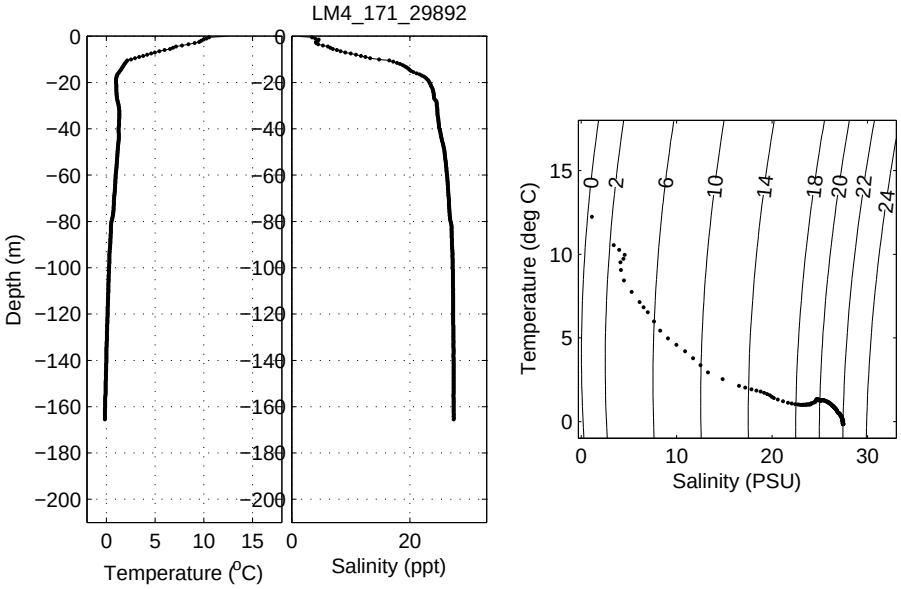

Figure 3.44: Profile of CTD cast JD171_LM4_171_29892.

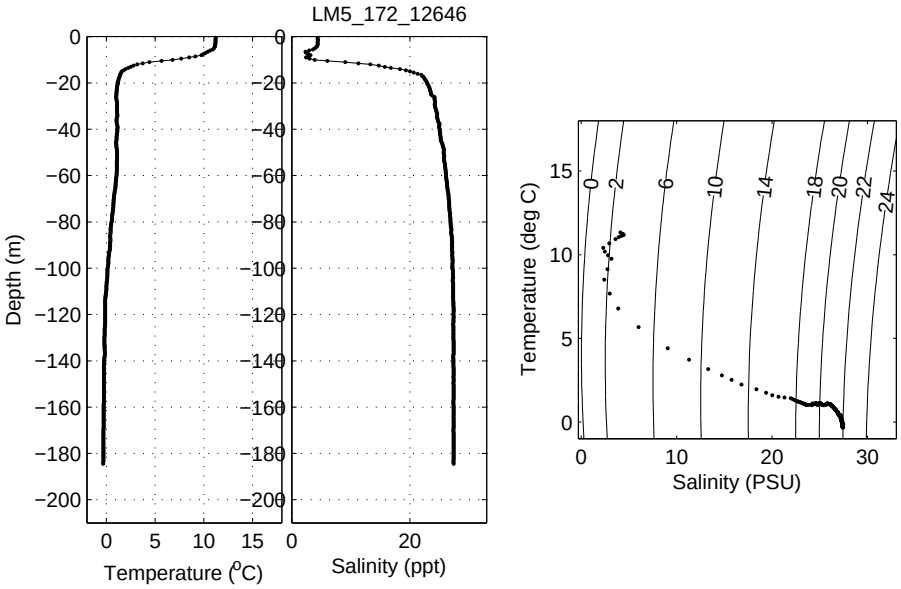

Figure 3.45: Profile of CTD cast JD172_LM5_172_12646.

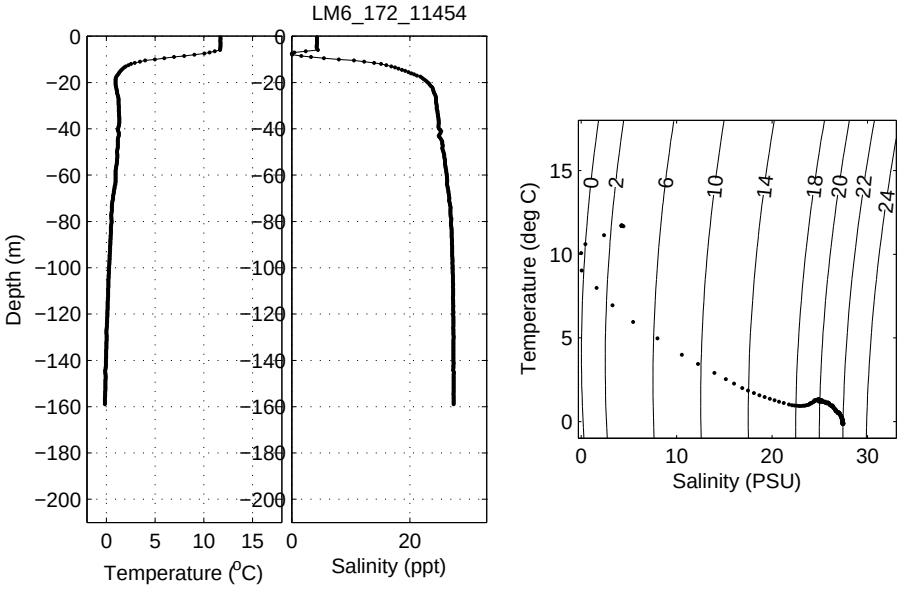

Figure 3.46: Profile of CTD cast JD172_LM6_172_11454.

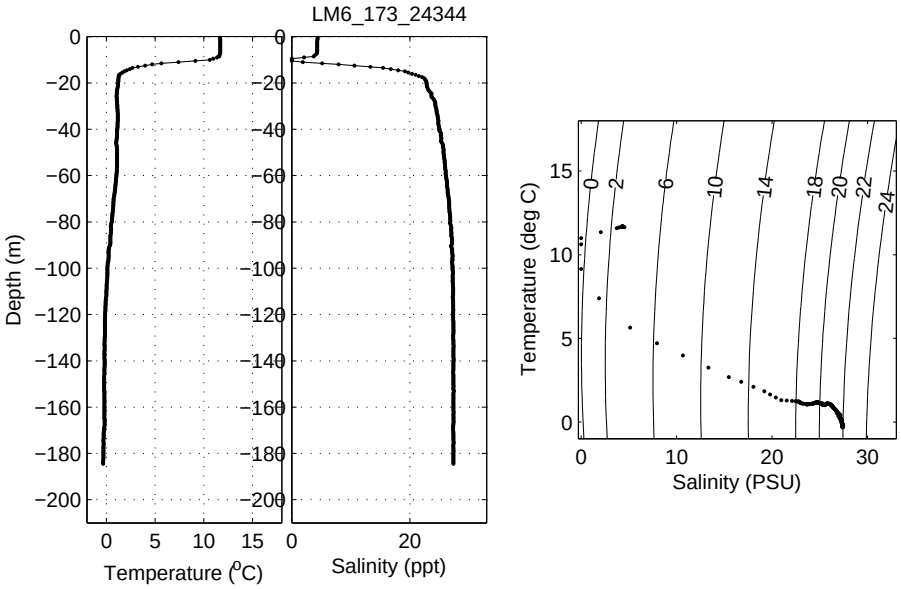

Figure 3.47: Profile of CTD cast JD173_LM6_173_24344.

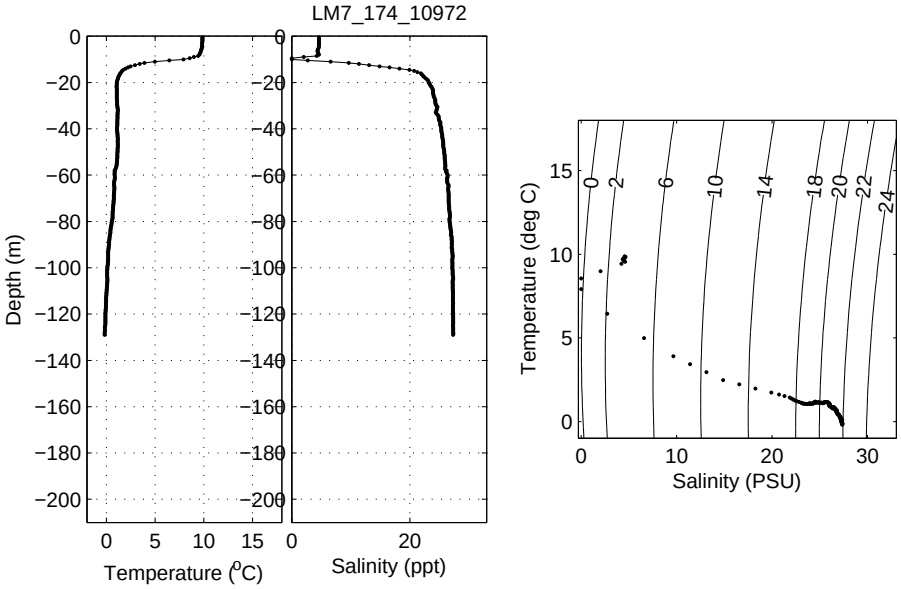

Figure 3.48: Profile of CTD cast JD174_LM7_174_10972

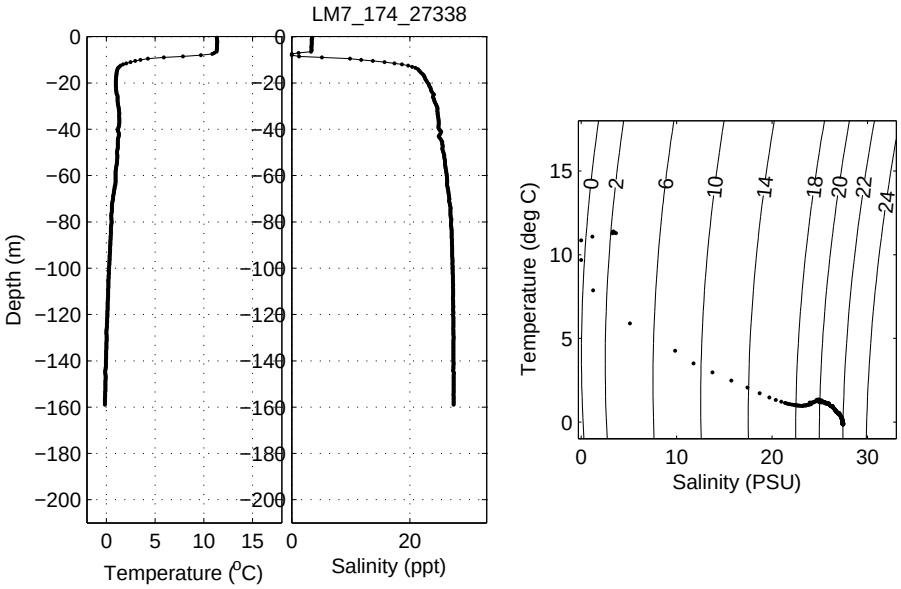

Figure 3.49: Profile of CTD cast JD174_LM7_174_27338

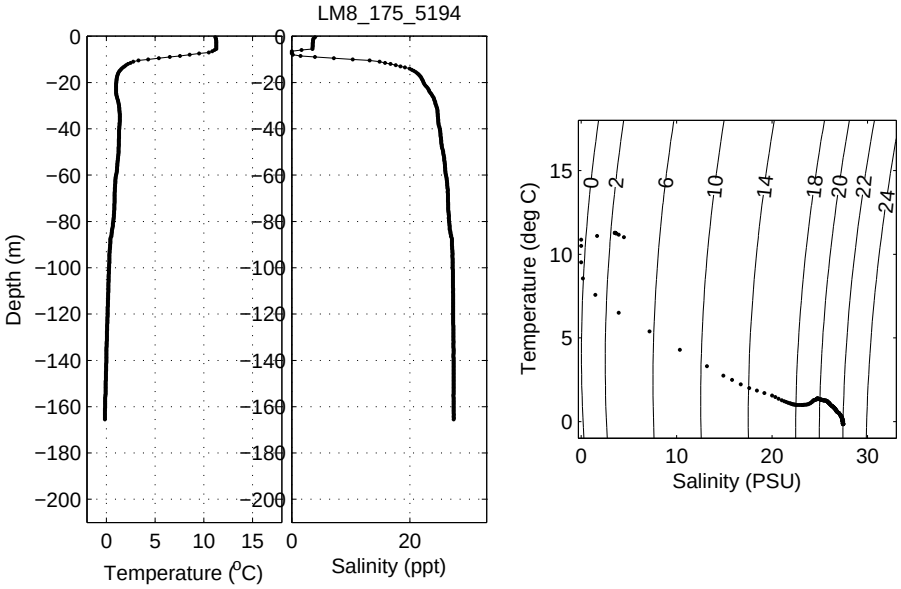

Figure 3.50: Profile of CTD cast JD175_LM8_175_5194

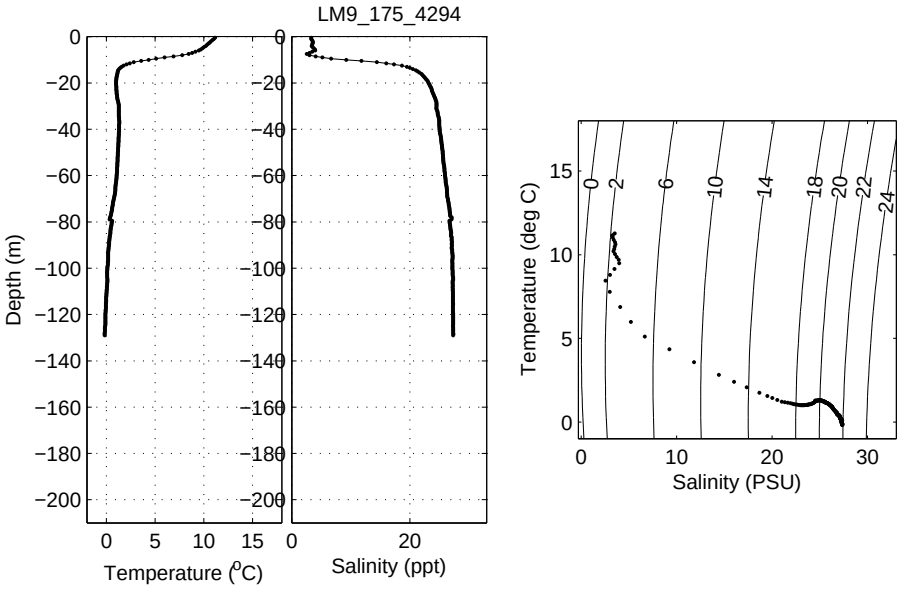

Figure 3.51: Profile of CTD cast JD175_LM9_175_4294

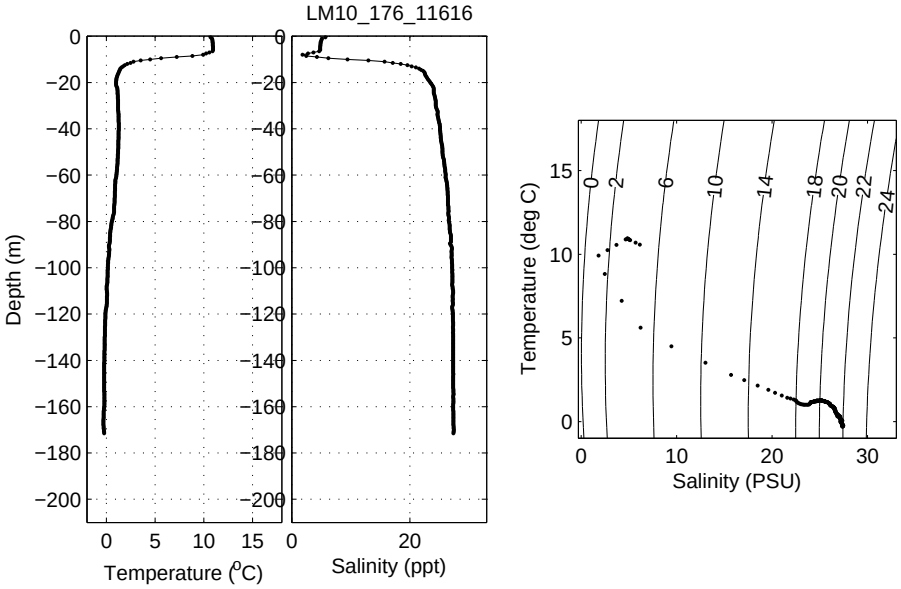

Figure 3.52: Profile of CTD cast JD176_LM10_176_11616

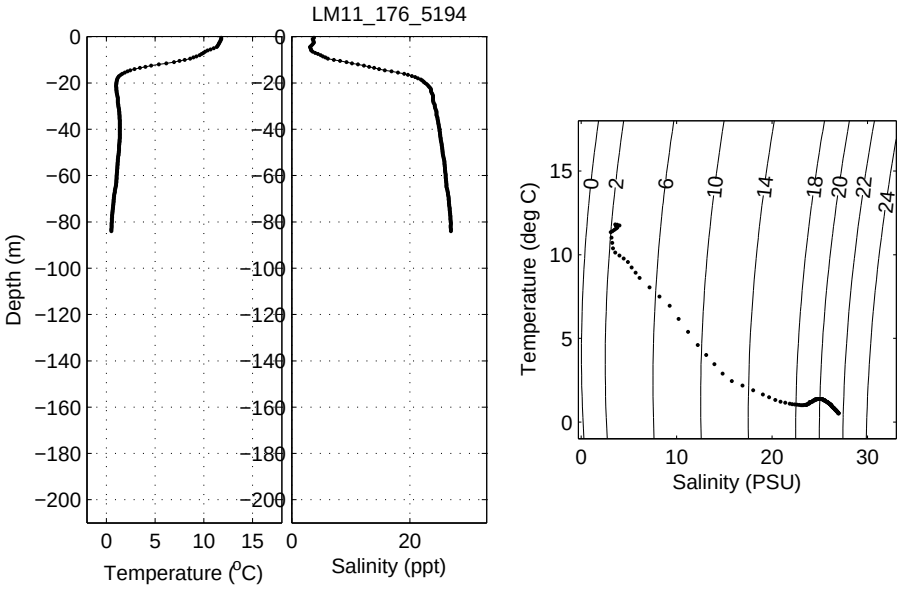

Figure 3.53: Profile of CTD cast JD176_LM11_176_5194

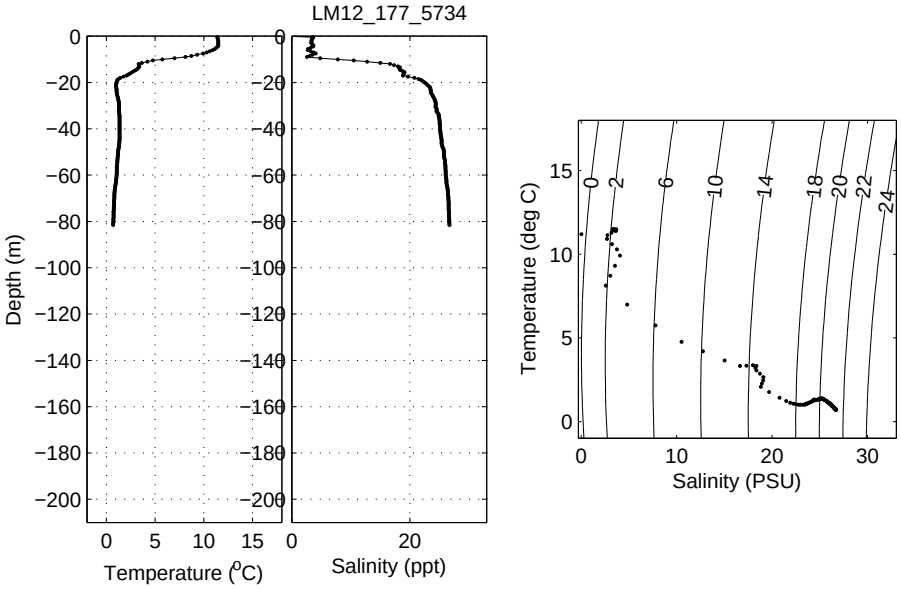

Figure 3.54: Profile of CTD cast JD177_LM12_177_5734

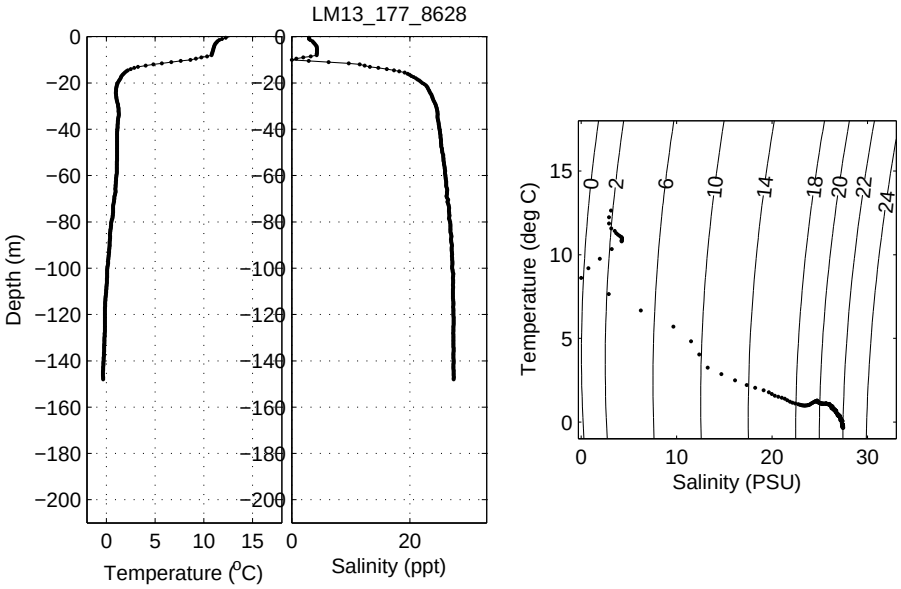

Figure 3.55: Profile of CTD cast JD177_LM13_177_8628

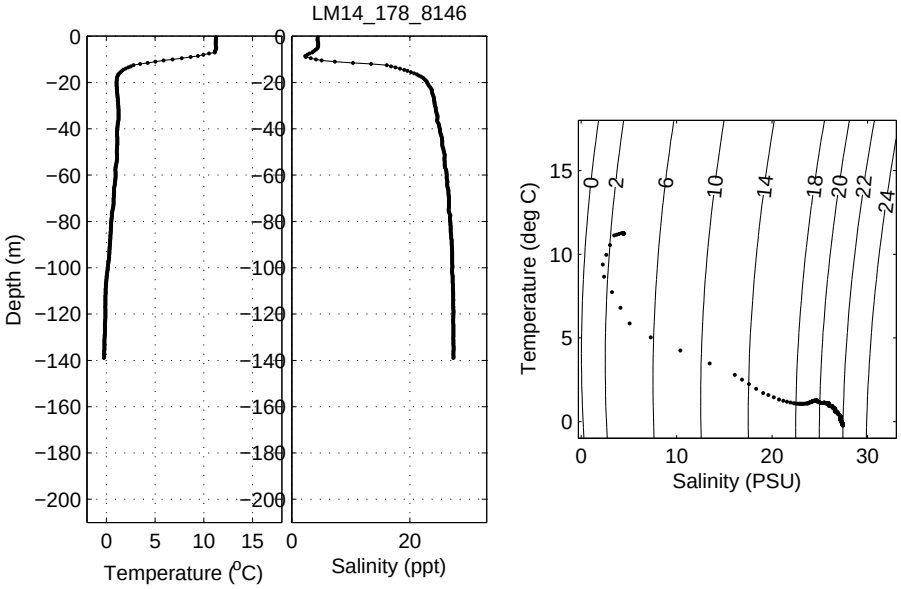

Figure 3.56: Profile of CTD cast JD178_LM14_178_8146

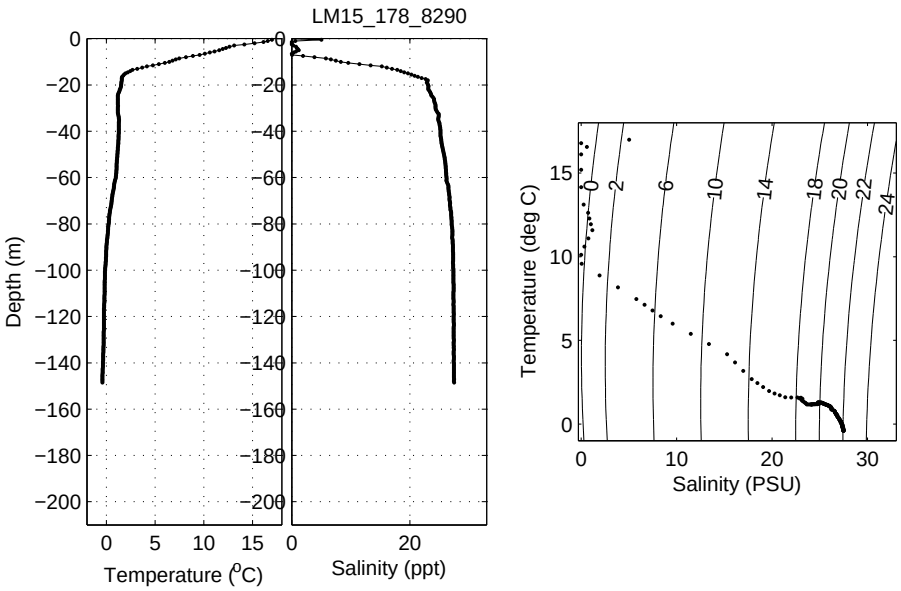

Figure 3.57: Profile of CTD cast JD178_LM15_178_8290

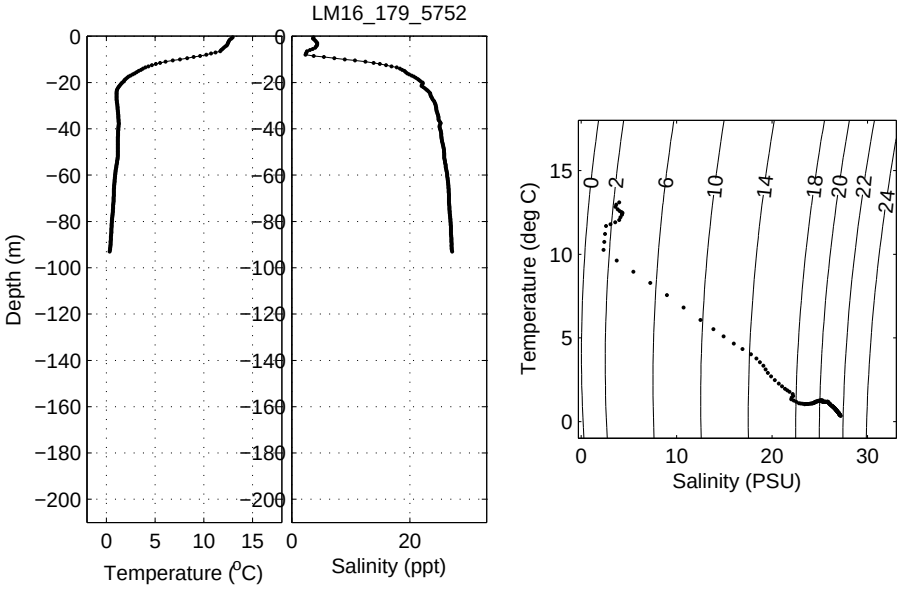

Figure 3.58: Profile of CTD cast JD179_LM16_179_5752

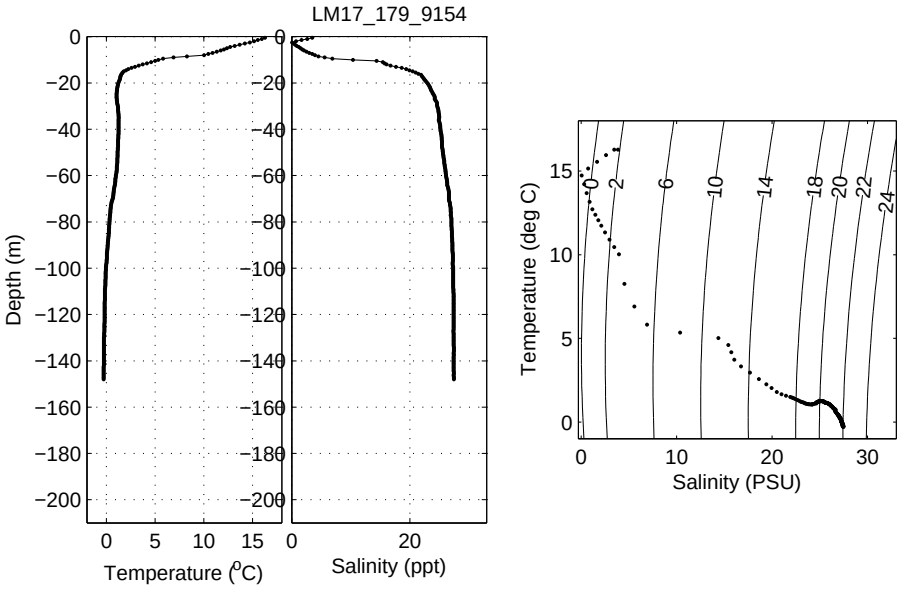

Figure 3.59: Profile of CTD cast JD179_LM17_179_9154

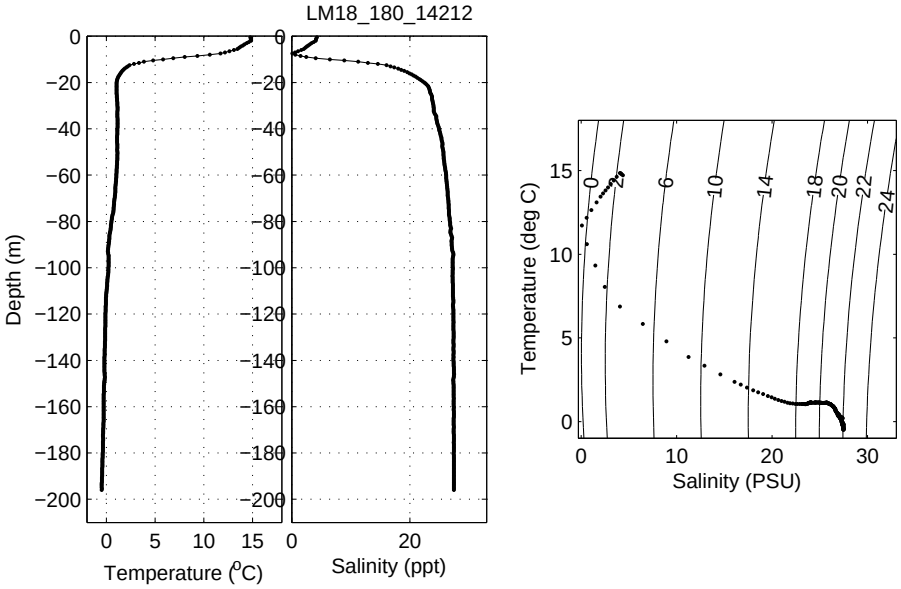

Figure 3.60: Profile of CTD cast JD180_LM18_180_14212

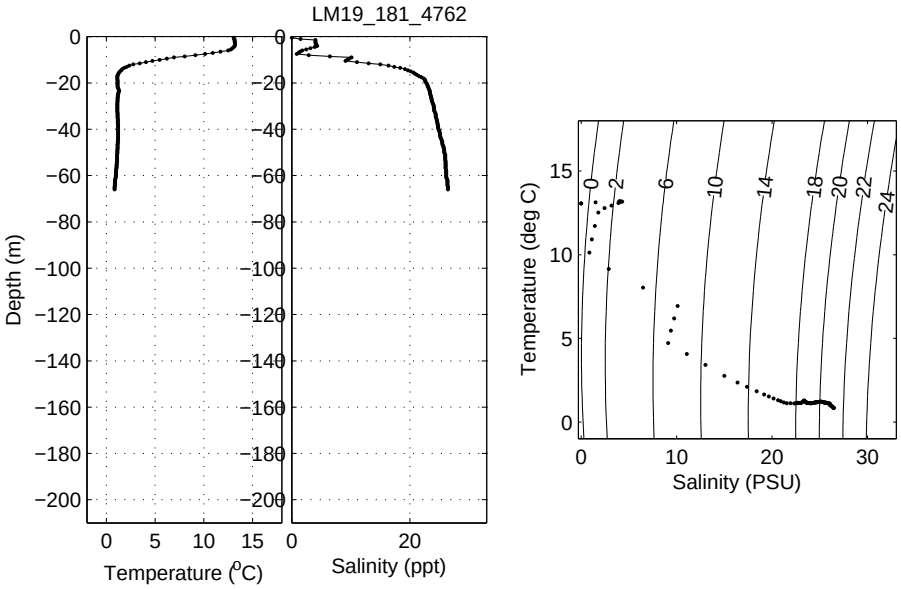

Figure 3.61: Profile of CTD cast JD181_LM19_181_4762

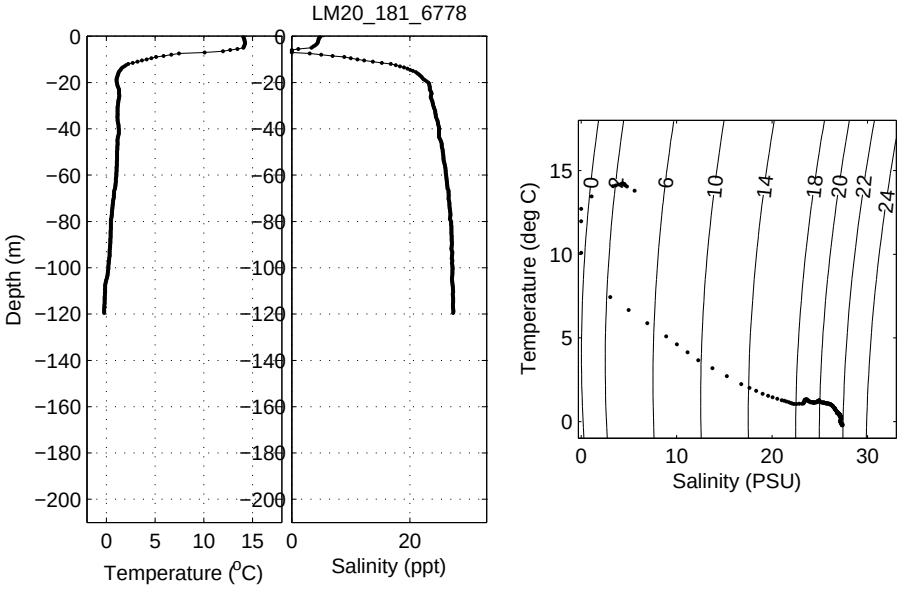

Figure 3.62: Profile of CTD cast JD181_LM20_181_6778

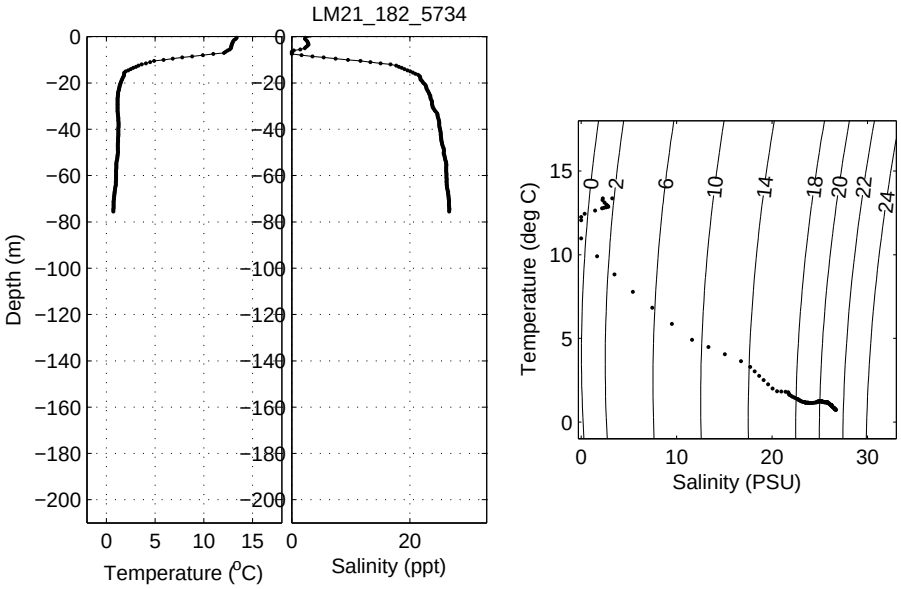

Figure 3.63: Profile of CTD cast JD182_LM22_182_5954

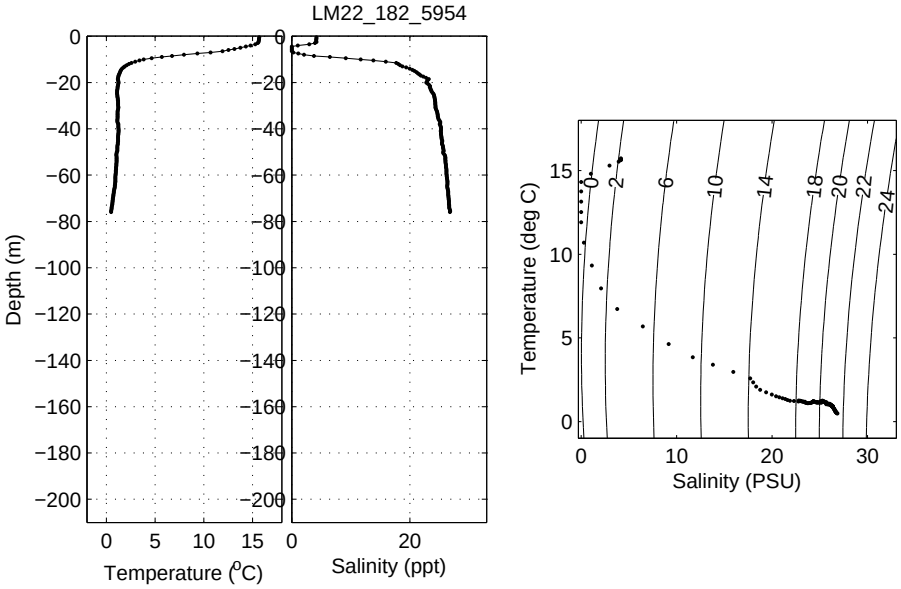

Figure 3.64: Profile of CTD cast JD182_LM22_182_5954

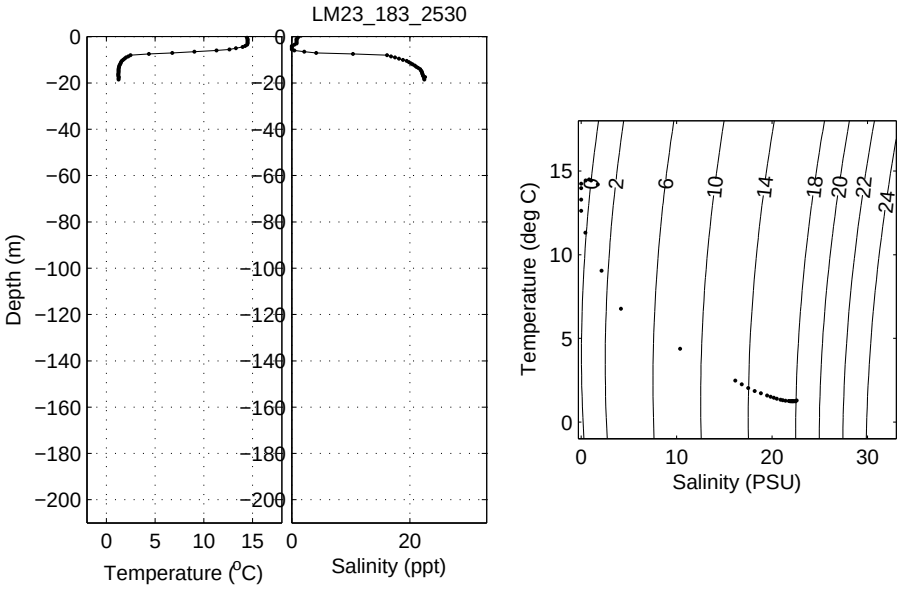

Figure 3.65: Profile of CTD cast JD183_LM23_183_2530

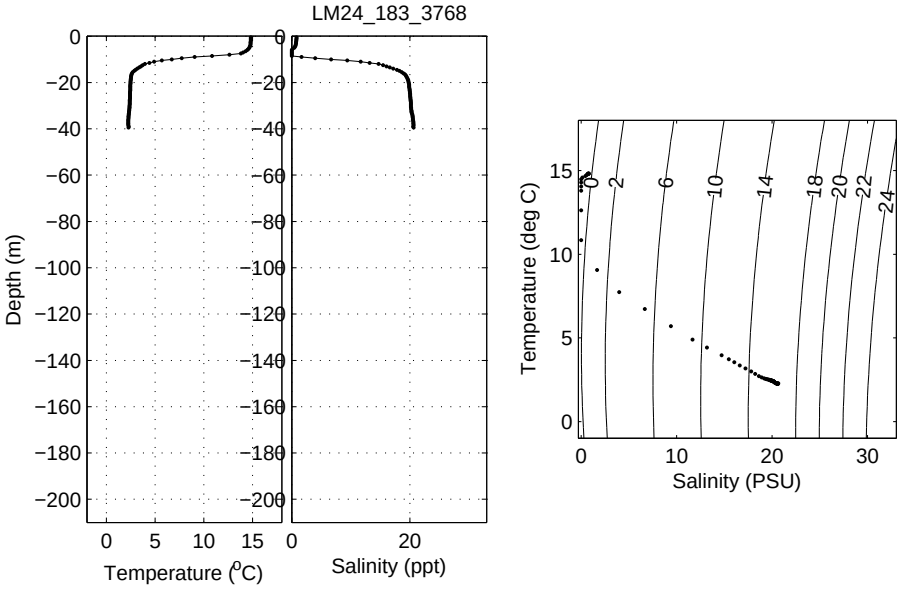

Figure 3.66: Profile of CTD cast JD183_LM24_183_3768

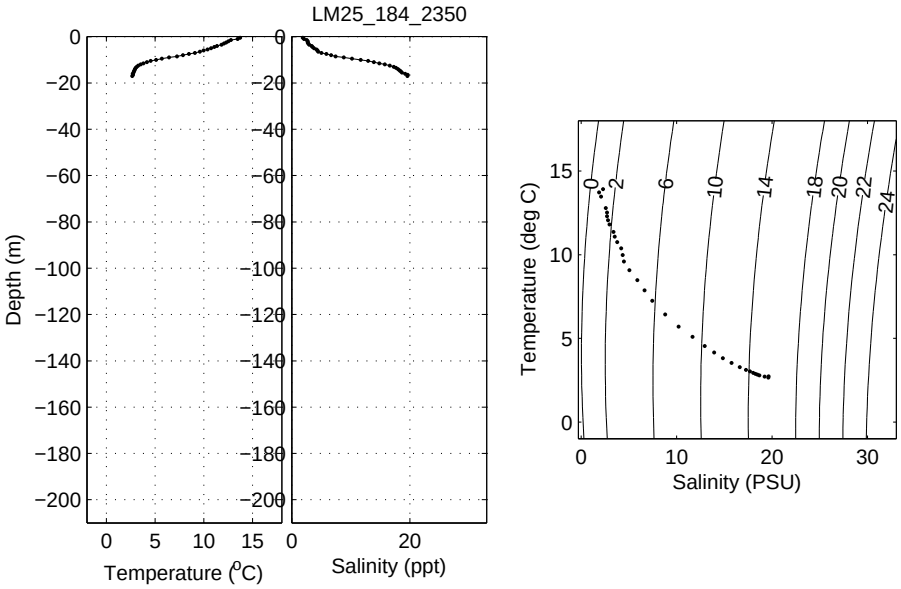

Figure 3.67: Profile of CTD cast JD184_LM25_184_2350

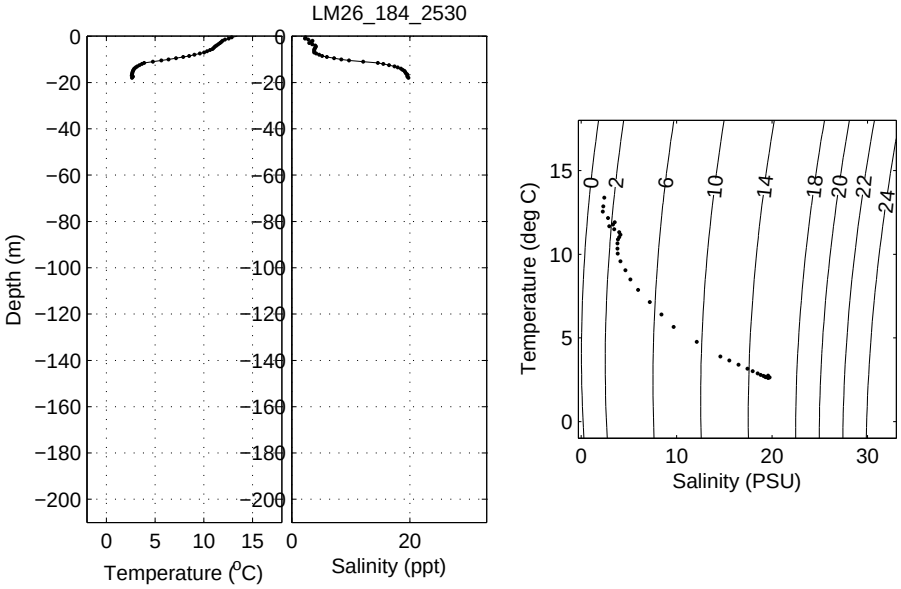

Figure 3.68: Profile of CTD cast JD184_LM26_184_2530

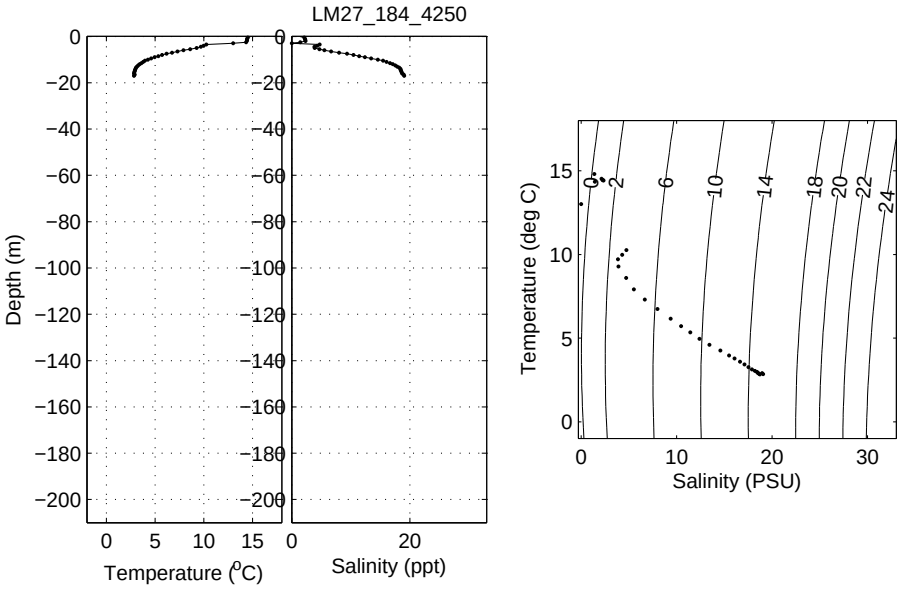

Figure 3.69: Profile of CTD cast JD184_LM27_184_4250

Chapter 4

Analysis and Results

Missing or bad data from both the thermistor and ACDP data were dealt with in the same manner: either they were replaced by linearly interpolated values from surrounding points if there was sufficient data, or if there was not, they were removed entirely and omitted from the plots.

Records from ADCP # 2460 were found bad and beam 2 was found bad due to some unknown reason. An ADCP uses four beams pointing in different directions to measure three velocity component. We need only three beams to find the water velocity components, but we add a fourth beam to compute a second vertical velocity component. The difference between the two vertical components produces an error velocity that helps determine whether the water currents are horizontally homogeneous and whether all four beams are operating properly. By replacing the bad beam 2 data velocity with a value calculated from the last row of the instrument transformation matrix so as to force the error velocity to zero. Indeed, the actual error velocity cannot be computed in this case, because there is no longer any redundant information. The X, Y, and Z components in the instrument coordinates are then calculated in the usual way using the other three rows (beam 1, 3 and 4) of the instrument transformation matrix. We then obtain the three beam solution for a RDI ADCP with Beam 2 bad.

Progressive vector plots, were created by calculating the distance travelled at each mooring using the unfiltered velocity data for each 30 minute interval. The position after each day is marked with an x, and the start and end positions are each marked with an unfilled and a filled circle, respectively.

In both the current velocity and the temperature isotherm time series plots, data were filtered using a 5th order forward-and-reverse Butterworth low pass digital filter with a cut-off frequency of 30 hours in order to remove high frequency variability. The filtered data were then interpolated into 0.25 m bins in order to plot the isotherms.

Currents records were divided into two groups, during periods with and without ice coverage, and were further analyzed and compared. At M1 mooring, ice coverage results was calculated from records between December 15th, 2012

and May 14th, 2013, when surface current was reduced obviously (Figure 3.1). At M2 mooring, ice coverage results was calculated from records between April 03rd, 2013 and April 20th, 2013, when surface current was reduced obviously (Figure 3.7).

Atmospheric data were obtained from Environment Canada for the same mooring period from the nearby weather monitoring station Happy Valley-Goose Bay. The wind stress calculated from the observed wind speed.

4.1 Statistical analysis

Table 4.1: Summary of current velocities at M1 (unit in cm/s).

		U			V		
Depth	Good Records	Mean	Max	Std. dev.	Mean	Max	Std. dev.
5	12888	17.74	235.62	61.48	-5.48	-121.07	23.24
11	12894	5.35	138.89	13.06	-0.30	-39.58	3.69
15	12902	8.51	117.12	15.77	0.97	-36.10	5.46
21	12902	4.06	110.81	13.41	0.91	-38.75	5.49
31	12902	0.67	87.67	10.37	-0.09	-36.71	5.57
51	12901	1.60	-74.52	11.35	-1.44	33.61	5.72
75	12902	5.19	65.05	12.58	0.04	-45.10	5.28
100	13407	3.17	50.80	13.13	0.40	-35.50	9.28
124	13408	0.72	-55.00	13.22	-1.68	-53.80	9.17
150	13410	-3.52	-64.30	14.11	-3.88	-55.70	10.32
174	13410	-7.34	-73.10	14.13	-4.06	-63.90	12.76
182	13409	-6.78	-62.10	10.25	-3.24	-48.20	11.06

Table 4.2: Summary of current velocities at M2 (unit in cm/s).

		U			V		
Depth	Good Records	Mean	Max	Std. dev.	Mean	Max	Std. dev.
5	12445	69.35	278.30	86.73	9.93	163.60	40.84
11	12447	23.39	172.60	29.61	6.60	72.60	11.66
15	12446	24.34	144.30	36.02	13.62	91.20	17.50
21	12447	9.04	119.50	37.44	7.49	81.80	18.81
31	12447	-7.59	100.70	32.45	-0.85	73.30	17.34
51	12447	-14.22	-110.60	31.25	-5.66	56.40	17.27
75	12447	-17.34	-112.60	33.14	-5.53	-48.40	15.32
95	12447	-16.40	-103.30	29.33	-7.54	-54.20	16.43

Statistical analysis for velocities were calculated and tabulated (Tables 4.1 and 4.2).

Averaged along Narrows velocity profiles at two mooring stations were calculated by averaging records of each ADCP bin over the mooring time period (Figure 4.1).

At station M1, eastward outflowing water was in the upper 30 m, and the compensating westward inflow was at depth of below 120 m depth. At station M2, the estuarine circulation is clearly shown, with eastward water in the upper

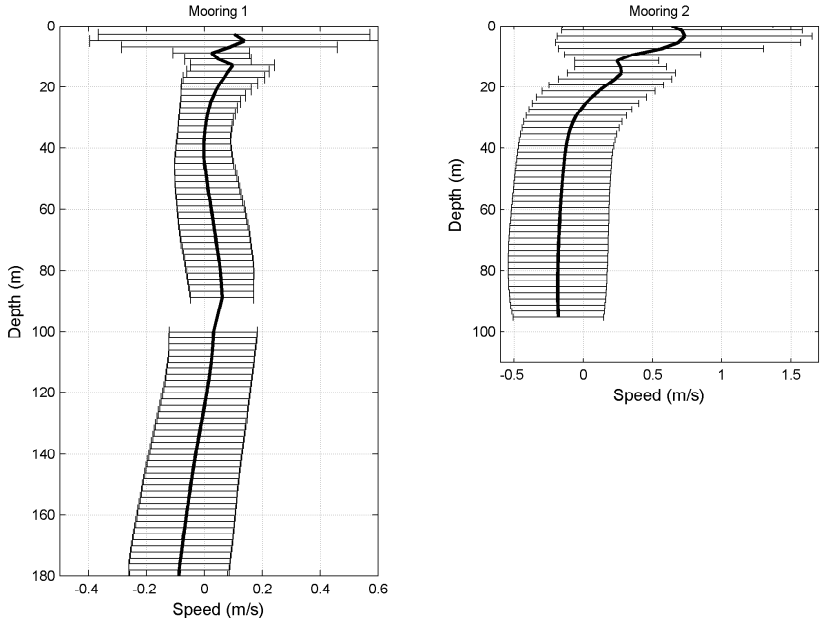

Figure 4.1: Averaged along Narrows velocity profile at M1 and M2 stations.

30 m, and the compensating westward inflow below 30 m depth. Averaged outgoing speed gradually increased to its maximum of about 70 cm/s at 10 meter depth. The speed then decreed with depth and changed direction to inward at depth of 30 m. It appeared that the velocity profile shown at mooring M2 is volume conserving.

4.2 Phase-Averaged Currents

Phase-averaged currents for M_2 tidal cycle and the magnitude of the vertical shear for M1 and M2 are presented in Figures 4.2 and 4.3. The phase ϕ is defined by $u(t) \propto cos(\phi)$, where $u(t)$ is the velocity near surface. So that $\phi = 0$ corresponds to the maximum falling/ebb tide and $\phi = \pi$ corresponds to the maximum flood/rising tide. Currents are close to zeros at $\phi = 1/2\pi$ and $\phi = 3/2\pi$.

The phase averaged magnitude was calculated as an average across M_2 tidal phase. For each M_2 cycle the velocities were interpolated to a common phase, and were then averaged over across M_2 tidal cycles. Phase-averaged currents are dominated by the M_2 tidal flow.

At M1 mooring station, phase averaged velocity field reveals near surface boundary layer thicknesses between 20 m as determined from amplitude and phase profiles, and tidal currents are constantly outflow. Below the constant surface outflow, flood tide reach its maximum 0.2 m/s at depth of 100m and

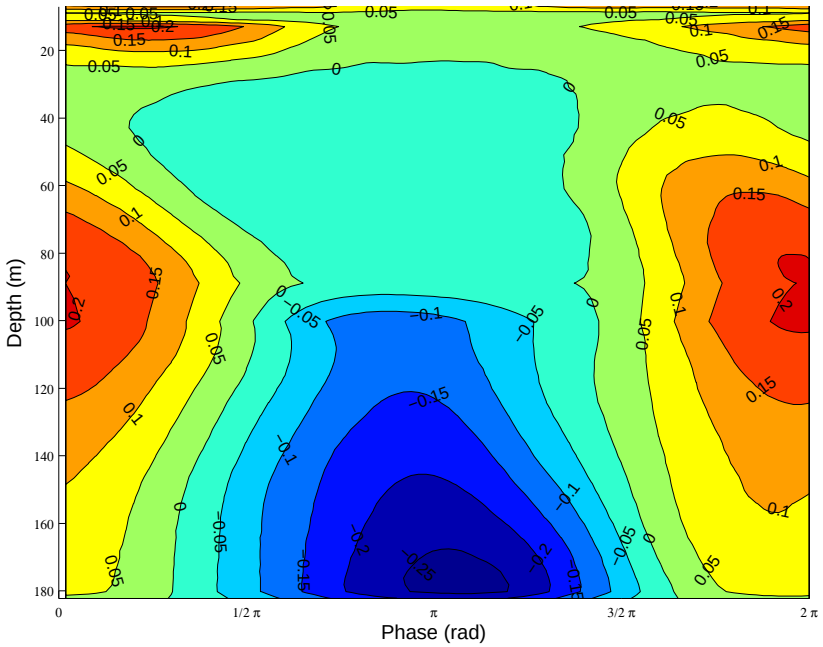

Figure 4.2: Phase-averaged along Narrows velocity for M_2 cycle, at M1.

ebb tide reach it maximum of 0.25 m/s around bottom (180 m).

At M2 mooring station, near surface boundary layer with constant seaward outflow is also revealed by the phase averaged velocity field. The surface layer exists over the top 20 meter and can reach its maximum velocity of over 0.8 m/s. Phase averaged velocity has opposite sign under the surface layer, ranging from 0.2 m/s to -0.4 m/s. The vertical structure of phase average velocity also show that maximum flooding of about 0.4 m/s mainly happened in the bottom layer (30 m to 90 m) and maximum ebb of about 1 m/s occur in the surface.

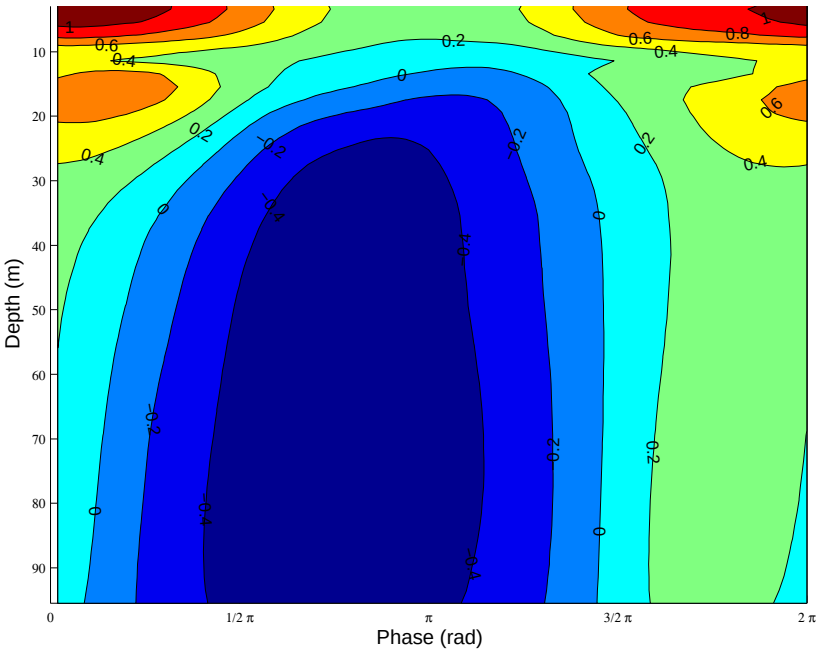

Figure 4.3: Phase-averaged along Narrows velocity for M_2 cycle, at M2.

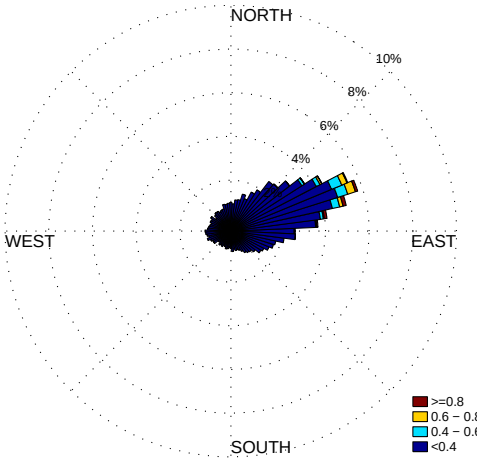

Figure 4.4: Rose plots of current at 10 m depth, M1 station.

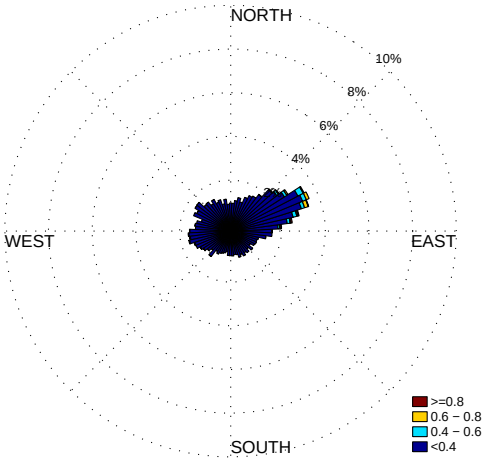

Figure 4.5: Rose plots of current at 20 m depth, M1 station.

4.3 Current rose

Rose plots for currents are presented in this section to show the current direction and percentage frequency of speed in specific intervals. The rose plots in Figures 4.4 and 4.13 give details of the described pattern of flood and ebb circulation for the two moorings. The overall rose plots show that there are clearly preferred current direction roughly along the narrows for both mooring locations. This significant symmetry in current direction also indicates that falling tide was in an opposite direction to rising tide.

At mooring M1, the currents flowed along the axis of the fjord towards and away from the Narrows (Figures 4.4 - 4.9). Near the surface at about 10 m depth, the prevalent direction was outward. Near the bottom, the flow direction was mainly inward. This symmetry of directions between ebb and flood tides indicates an strong and regular tidal signal. During the flood phase, the tidal current near the surface are enough to overcome the eastward outflow, and enhance the inflow at depth. During an ebb tidal phase, the surface average flow is out of the bay but the current at 175 m depth is still inward.

At mooring M2, it shows that currents flowed in dominant directions of along the narrows as well(Figures 4.10 - 4.13). At the surface, the flow was in outward direction both during flood and ebb tidal phases. Near the bottom, there is a symmetry between ebb and flood tidal current directions, and the prevailing direction was inward.

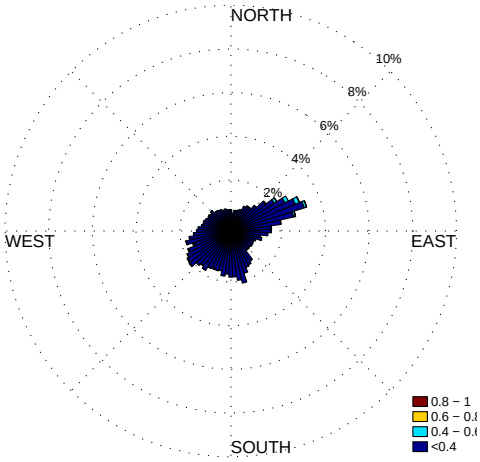

Figure 4.6: Rose plots of current at 50 m depth, M1 station.

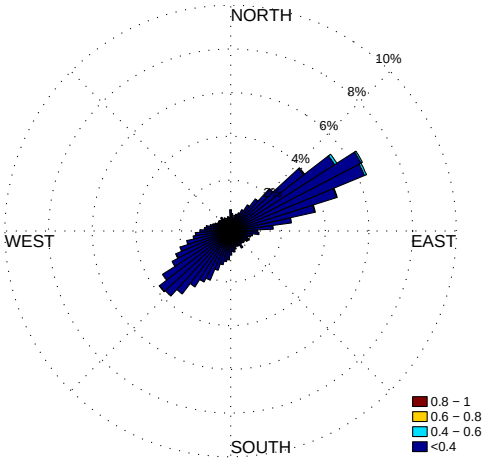

Figure 4.7: Rose plots of current at 100 m depth, M1 station.

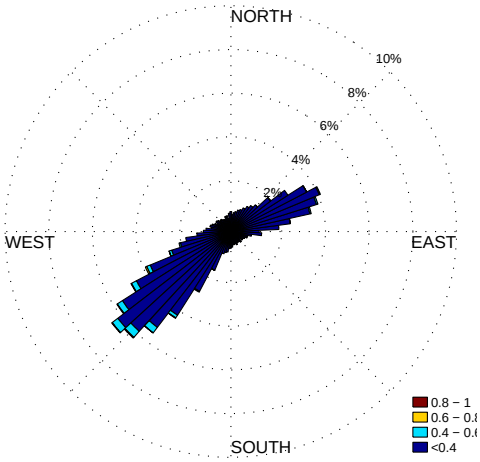

Figure 4.8: Rose plots of current at 150 m depth, M1 station.

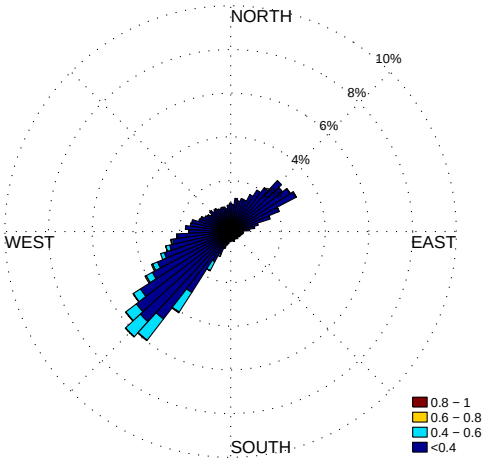

Figure 4.9: Rose plots of current at 175 m depth, M1 station.

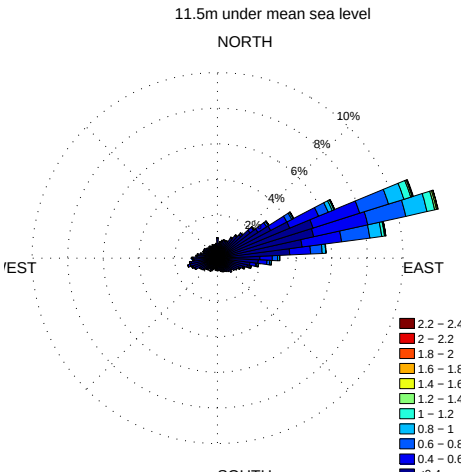

Figure 4.10: Rose plots of current at 10 m depth, M2 station.

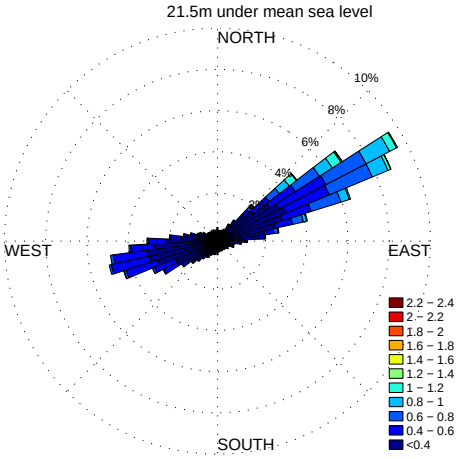

Figure 4.11: Rose plots of current at 20 m depth, M2 station.

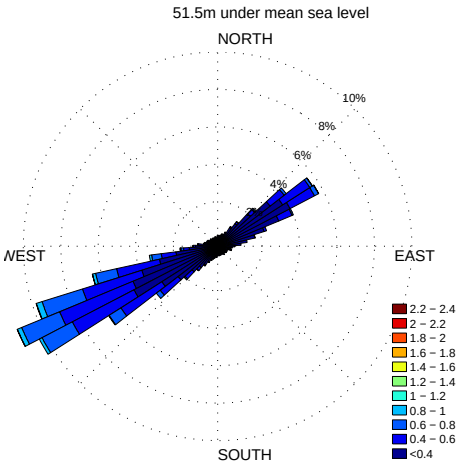

Figure 4.12: Rose plots of current at 50 m depth, M2 station.

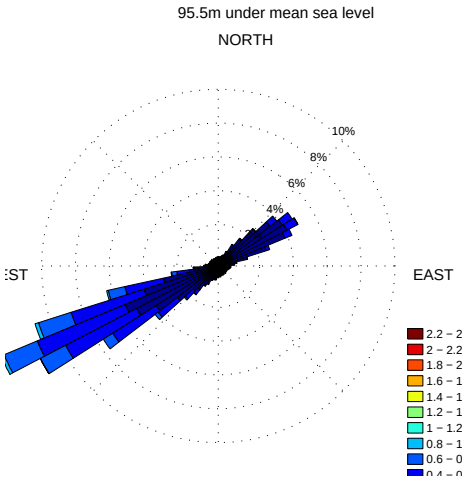

Figure 4.13: Rose plots of current at 95 m depth, M2 station.

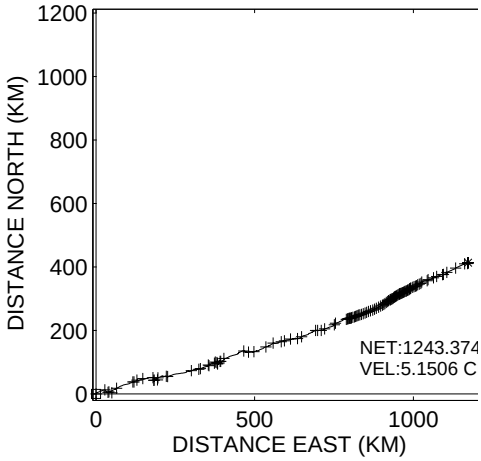

Figure 4.14: Progressive vector diagrams at 10 m depth, M1 station.

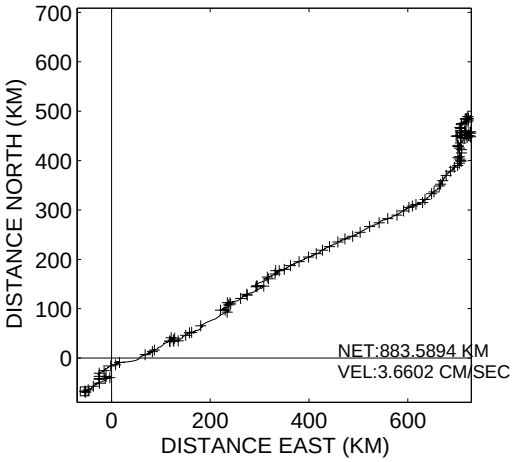

Figure 4.15: Progressive vector diagrams at 20 m depth, M1 station.

4.4 Progressive vector diagrams

Progressive vector diagrams show the distance and direction a particle of water would travel if the flow were spatially uniform. The progressive diagrams in Figures 4.14 - 4.23 were produced from 30-minute samples. The cross marks in the diagram represent time intervals of two days. Variabilities of different timescales are superimposed on the residual current according to the progressive vector diagrams. A net displacement in outward direction at the surface and an inward flow near the bottom can be found at both mooring stations.

At mooring M1, averaged surface current velocity was 11.7 cm/s at depth of 7 meter, over the duration of the measurements. At the depth of 21 m, the averaged speed reduced to only 3.6 cm/s. Inward flow was found below 130 m depth, and at depth of 180 m and the its maximum speed of about 8.9 cm/s.

At mooring M2, the averaged outward current at 5 m depth was 70 cm/s and directional variability was weak. at 50 m depth, the averaged current was 15 cm/s and the current direction switched from northeast to southwest anticlockwise. At the depth of 95 m, current direction was very organized and increased to 18 cm/s.

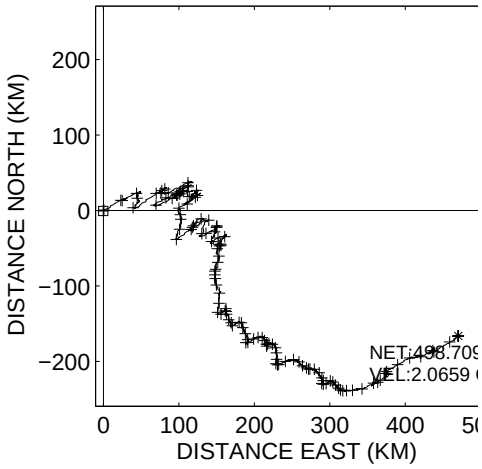

Figure 4.16: Progressive vector diagrams at 50 m depth, M1 station.

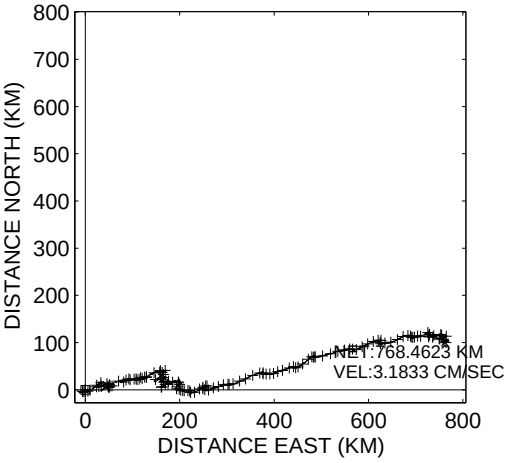

Figure 4.17: Progressive vector diagrams at 100 m depth, M1 station.

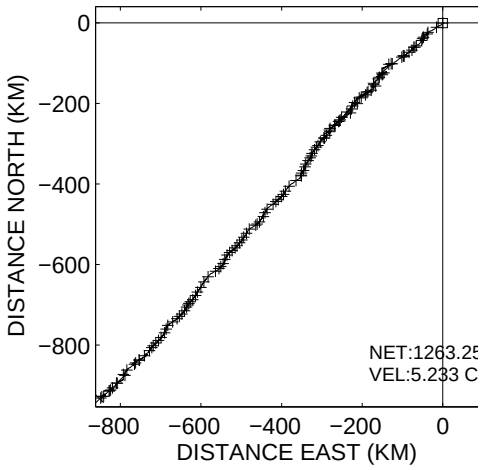

Figure 4.18: Progressive vector diagrams at 150 m depth, M1 station.

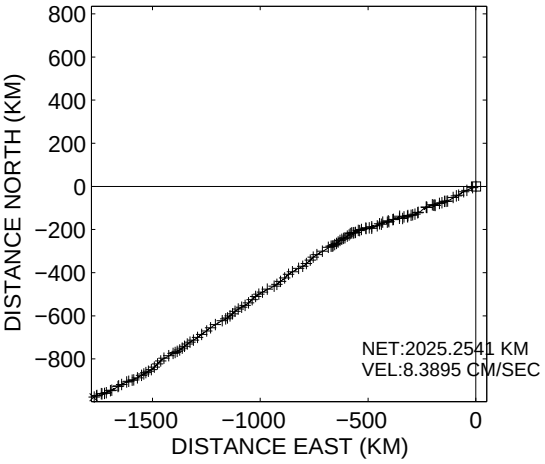

Figure 4.19: Progressive vector diagrams at 175 m depth, M1 station.

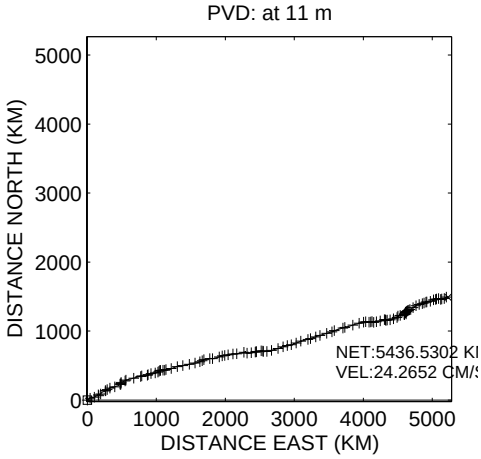

Figure 4.20: Progressive vector diagrams at 10 m depth, M2 station.

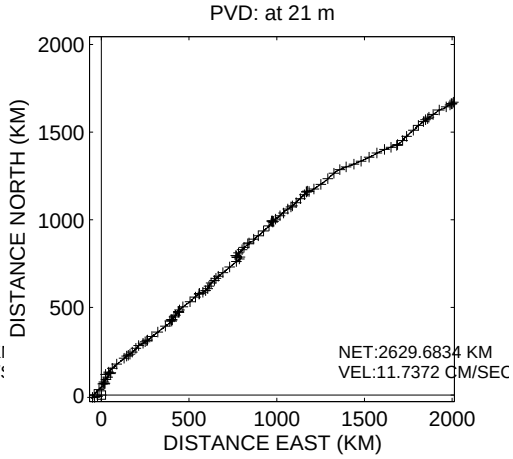

Figure 4.21: Progressive vector diagrams at 20 m depth, M2 station.

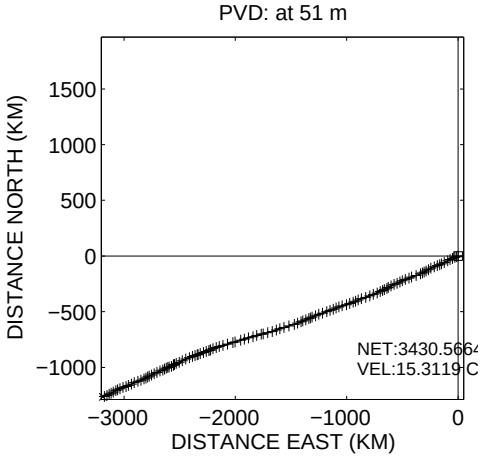

Figure 4.22: Progressive vector diagrams at 50 m depth, M2 station.

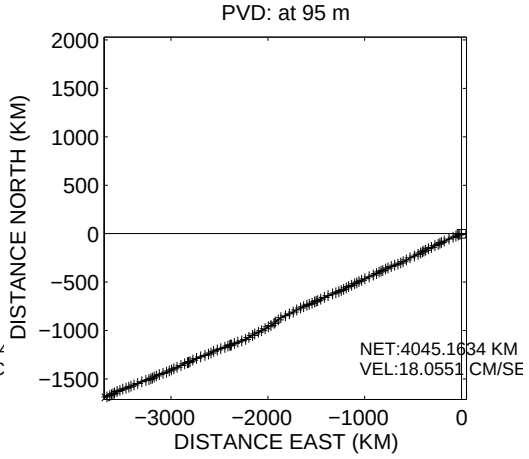

Figure 4.23: Progressive vector diagrams at 95 m depth, M2 station.

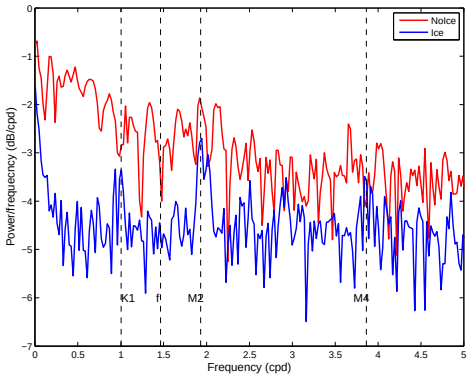

Figure 4.24: Power Spectral Density plot at 10 m, M1.

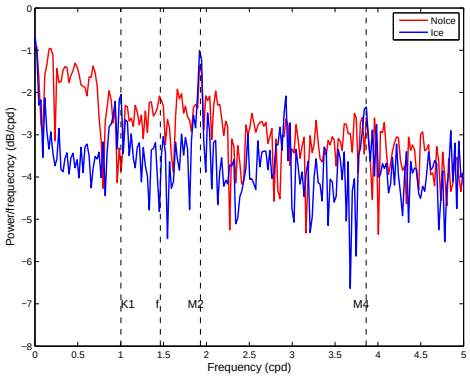

Figure 4.25: Power Spectral Density plot at 20 m, M1.

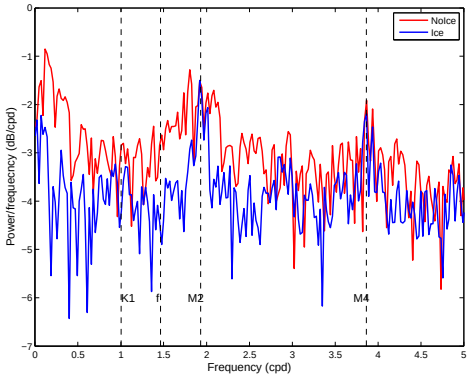

Figure 4.26: Power Spectral Density plot at 50 m, M1.

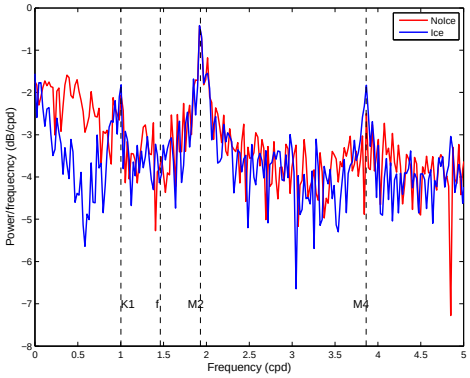

Figure 4.27: Power Spectral Density plot at 100 m, M1.

4.5 Spectral Analysis

Spectral analysis was used to investigate the kinetic energy distribution. The Power Spectral Density technique was performed on the current component along the narrows. Figures 4.24- 4.29 show graphically, the results of the spectral calculations for both the ice covered and ice-free periods of selected depth at M1 mooring station. The Power Spectral Density plots indicate that a low frequency current with a period longer than 2 days (0.5 cpd) and K_1 were the most significant current at the surface. Below the outward surface flow, it shows that the semidiurnal tides (M_2) dominate the energy spectrum for both locations. Inertial current (about 16 hours period) was found not important to the energy spectrum. The meridional (North/South) component was found weaker than the zonal component (East/West).

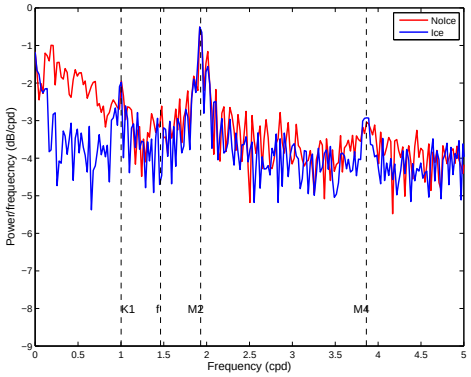

Figure 4.28: Power Spectral Density plot at 150 m, M1.

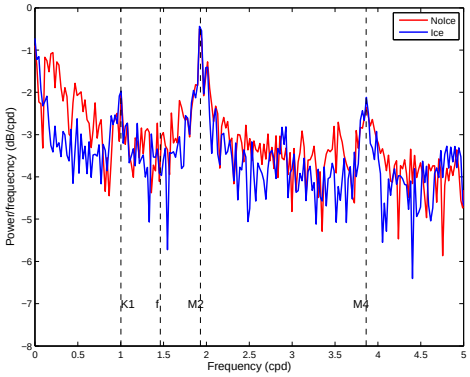

Figure 4.29: Power Spectral Density plot at 175 m, M1.

4.6 Harmonic Analysis

Table 4.3: M_2 Tidal Constituents at M1 mooring, without ice coverage.

Depth (m)	Major Axis (cm/s)	Minor Axis (cm/s)	Inclination (°)	Phase (°)
5	22.669822	-0.50499	15.953567	201.806727
10	4.905687	0.107556	15.669277	196.294592
15	9.051869	1.042162	19.558558	204.3689
20	5.877256	1.303027	19.93042	208.163059
30	3.233096	-0.178225	173.449937	348.395496
50	5.967444	-0.979393	29.915958	150.147425
75	10.364591	0.224036	31.268799	177.547935
100	15.939299	-1.590699	35.254379	184.67624
125	13.64008	0.310864	34.677613	183.713478
150	14.883606	-1.474499	35.083393	182.633735
175	16.068093	-0.558424	44.023135	189.851874
182	11.585766	0.269491	46.905899	191.068376

Table 4.4: M_2 Tidal Constituents at M1 mooring, with ice coverage.

Depth (m)	Major Axis (cm/s)	Minor Axis (cm/s)	Inclination (°)	Phase (°)
5	0.746829	-0.161961	52.827693	213.941924
10	0.909817	-0.150363	14.264564	223.685964
15	6.930137	-0.29181	25.714295	243.888289
20	3.659508	0.891525	33.978563	242.388861
30	3.162909	-1.070302	174.280822	7.439572
50	6.288649	0.036668	35.238794	162.560078
75	11.204495	-0.336359	29.108614	197.616752
100	16.941599	-1.293379	32.298403	197.276826
125	15.216556	-1.480747	30.923522	192.07998
150	16.120469	-1.891228	34.998236	189.244191
175	19.595317	-1.432835	45.50514	199.441373
182	16.316145	-0.235599	52.7955	202.756603

Table 4.5: K_1 Tidal Constituents at M1 mooring, without ice coverage.

Depth (m)	Major Axis (cm/s)	Minor Axis (cm/s)	Inclination (°)	Phase (°)
5	5.330496	-1.488999	32.870091	215.654446
10	2.072296	0.054592	30.501423	310.465921
15	3.161821	0.195395	19.764072	331.130433
20	1.940206	-0.113246	172.088066	129.041514
30	1.139085	-0.456445	177.862322	148.725487
50	0.691229	-0.445596	78.711879	15.978665
75	1.076813	0.043466	55.92923	330.000076
100	2.13133	-0.500596	33.687051	321.566338
125	1.672409	0.125041	33.106217	309.407035
150	2.231882	0.346638	38.01068	316.012924
175	2.624676	0.469497	39.876414	312.192941
182	1.949924	0.445438	40.997456	321.990449

Table 4.6: K_1 Tidal Constituents at M1 mooring, with ice coverage.

Depth (m)	Major Axis (cm/s)	Minor Axis (cm/s)	Inclination (°)	Phase (°)
5	0.118488	-0.021284	20.017081	37.856946
10	0.472977	0.063023	7.226775	311.337356
15	3.118859	0.258367	17.125183	8.027243
20	2.649342	-0.013746	14.408383	13.041827
30	1.432044	-0.01646	8.188713	18.234421
50	0.520759	-0.040491	125.188168	126.05046
75	1.414069	0.140525	11.482274	282.87046
100	3.210873	-0.04626	27.270901	321.775505
125	2.975776	0.030081	33.203608	313.260684
150	2.894771	0.096328	27.463436	307.552594
175	3.274474	0.377175	40.551823	307.606173
182	2.771038	0.32376	45.706242	309.870105

Harmonic analysis was performed on the data to separate the tidal constituents and thus gain information on the tidal flow. Two principal lunar semidiurnal M_2 and K_1 are the major constituents at both mooring station. The largest contribution at all depths is from the M_2. Another important result of the harmonic analysis is the rotation angle of the tidal ellipses or hodographs. It gives an estimate of the orientation of the tidal constituents. A negative value for the length of the semi-minor axis indicates that the current rotates clockwise around the tidal ellipse. The values for the M_2 and K_1 constituent at different depths are presented in Tables 4.3 to 4.10.

Table 4.7: M_2 Tidal Constituents at M2 mooring, without ice coverage.

Depth (m)	Major Axis (cm/s)	Minor Axis (cm/s)	Inclination (°)	Phase (°)
5	41.95205	-3.983199	19.744847	181.08098
10	19.775743	1.205265	16.289154	193.235694
15	41.763989	1.865548	23.463092	193.983214
20	46.457512	-0.172669	23.267689	176.980706
30	42.093009	-3.290031	25.733096	159.407581
50	41.597522	0.892794	27.449053	149.794639
75	42.547737	0.953402	23.851608	145.032116
95	38.438254	1.234153	27.945218	140.049929

Table 4.8: M_2 Tidal Constituents at M2 mooring, with ice coverage.

Depth (m)	Major Axis (cm/s)	Minor Axis (cm/s)	Inclination (°)	Phase (°)
5	1.791487	-0.670674	15.437559	311.200072
10	2.679947	1.348676	45.200336	241.555428
15	24.062394	-0.019441	25.729318	200.332207
20	45.353446	-0.245383	19.678915	197.680343
30	44.809753	-1.5383	18.403944	182.045972
50	48.277609	0.350242	29.743501	162.009077
75	49.019109	1.651529	23.404788	154.351614
95	45.279723	-0.264747	27.330142	148.525681

The inclinations of tidal ellipses represent the degrees the major axes make with respect to east. The results show that at both Moorings M1 and M2 the tidal currents were aligned along the axis of Narrows/Channels throughout the water column. The small amplitudes of the minor axes indicate a weak cross-channel flow.

At Location M1, when the lake was not covered by ice, maximum magnitude of M_2 was at 5 depth was about 23 cm/s, and magnitude decreased with depth to about 3 m/s at 30 m. Below 30 m depth, magnitude of M_2 start to increase with depth and it is 16 cm/s at about 175 m depth. Almost all M_2 tidal energy was dissipated traveling through the narrows near the top 20 m. The remained M_2 tidal energy was then reflected to the deeper layer of the water column (Figures 4.31 to 4.34). In the upper 30m, the tidal amplitude reduced during the ice cover. Tidal phase was also delayed by about 140° ($\sim$ 4.7 hours) at 5 m depth.

At Location M2, the magnitude of M_2 was about 40 cm/s below the top 30 m. Surface M_2 tidal amplitude was about 40 cm/s without ice cover and was receded to 1.8 cm/s and phase was delayed by about 130° ($\sim$ 4.3 hours) at 5 m depth.

For both locations, magnitude of K_1 near the surface was also reduced after tidal wave passed the Narrows, and amplitudes were reduced by ice cover as well (Figures 4.31 to 4.34).

Table 4.9: K_1 Tidal Constituents at M2 mooring, without ice coverage.

Depth (m)	Major Axis (cm/s)	Minor Axis (cm/s)	Inclination (°)	Phase (°)
5	5.962808	-2.74355	168.976192	191.707792
10	3.375356	0.167927	0.506403	3.058825
15	7.917724	-0.140494	27.853369	354.854458
20	10.07466	-0.33553	31.121251	334.582843
30	8.403722	-0.890262	23.553497	320.533347
50	6.816233	-0.889407	22.521773	308.982689
75	5.668982	-0.159083	25.651688	307.020711
95	4.338189	0.570466	29.091251	302.456458

Table 4.10: K_1 Tidal Constituents at M2 mooring, with ice coverage.

Depth (m)	Major Axis (cm/s)	Minor Axis (cm/s)	Inclination (°)	Phase (°)
5	0.432238	-0.070386	6.653064	294.661993
10	1.038059	-0.119656	36.015789	334.180578
20	8.774175	-1.09239	18.919257	321.29984
30	10.313574	-1.263909	24.965087	305.920677
50	7.483781	0.391987	28.652045	289.78522
75	5.824723	-0.622636	21.717809	293.804077
95	4.474739	-0.065285	18.41091	290.555829

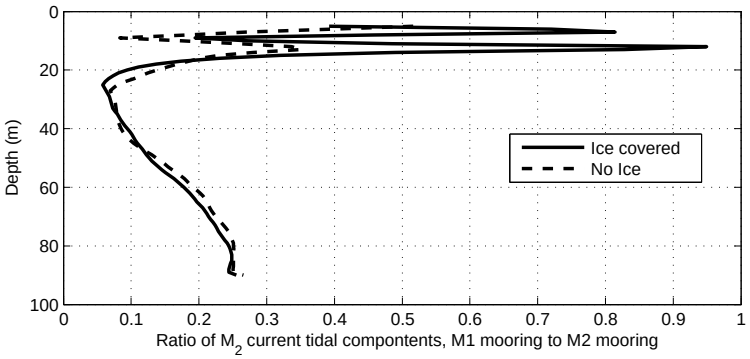

Figure 4.30: Ratio of Tidal harmonics amplitude profiles, M1 to M2, with and without ice coverage.

Figure 4.30 shows ratio profile of M_2 tidal current components (major axes of tidal ellipses) at M1 moorings. When the lake was not covered by ice, the ratio of tidal amplitudes at two moorings was less than 50 percents, indicating that only about 25 percents of tidal energy can pass the Narrow between surface to about 90 m.

Tidal ellipses for different depths at both locations are presented in Figures 4.35 - 4.54.

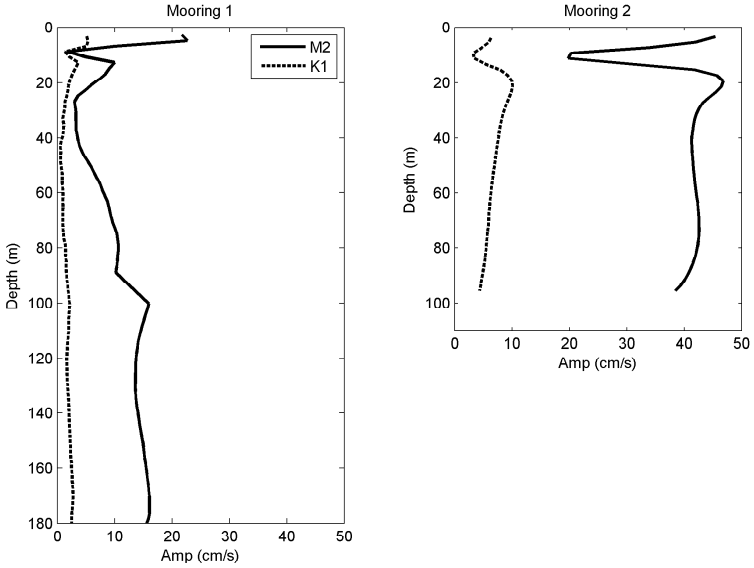

Figure 4.31: Tidal harmonics amplitude profiles at M1 and M2 stations, without ice coverage.

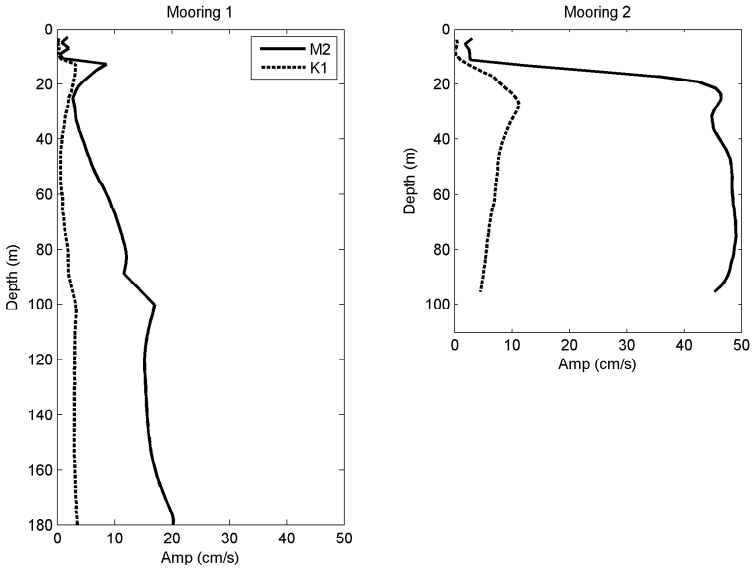

Figure 4.32: Tidal harmonics amplitude profiles at M1 and M2 stations, with ice coverage.

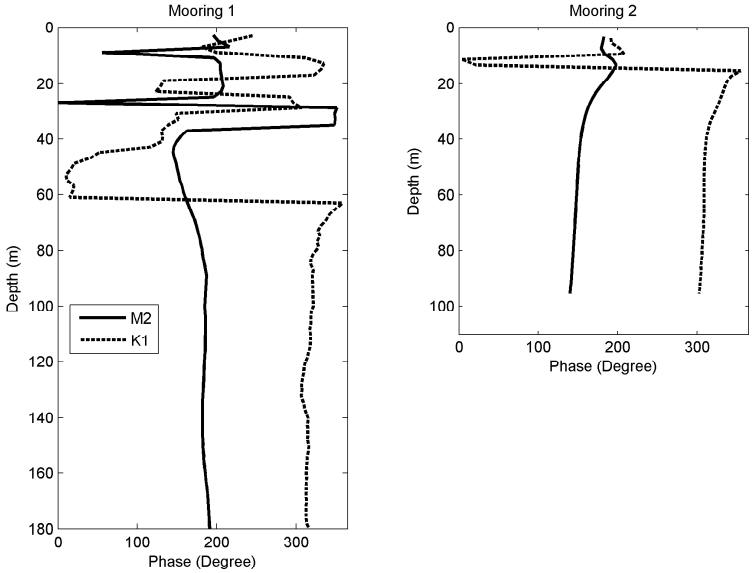

Figure 4.33: Tidal harmonics phase profiles at M1 and M2 stations, without ice coverage.

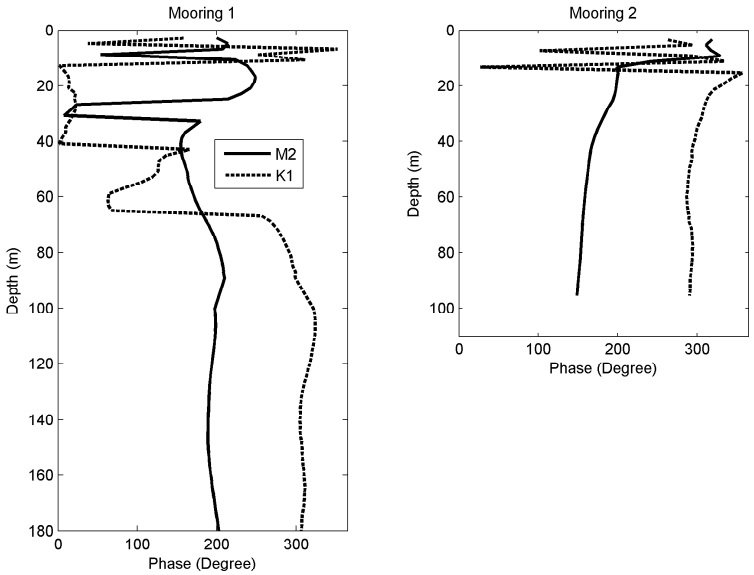

Figure 4.34: Tidal harmonics phase profiles at M1 and M2 stations, with ice coverage.

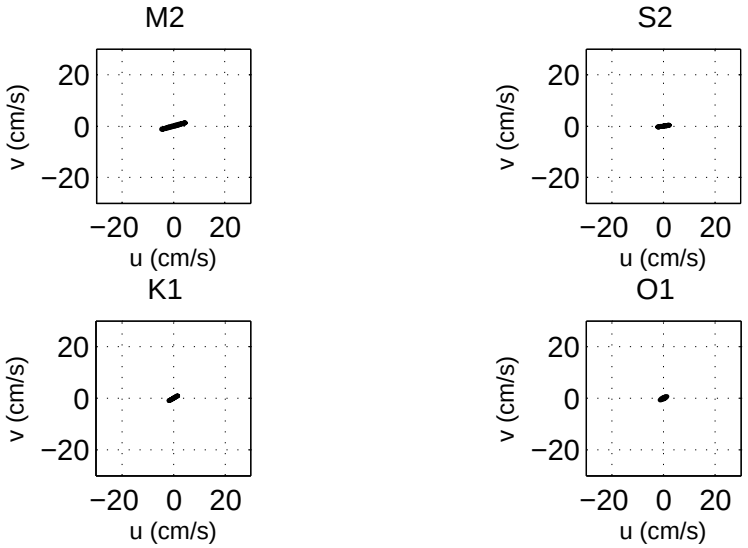

Figure 4.35: Tidal Ellipse of the currentat 10 m without ice coverage, M1.

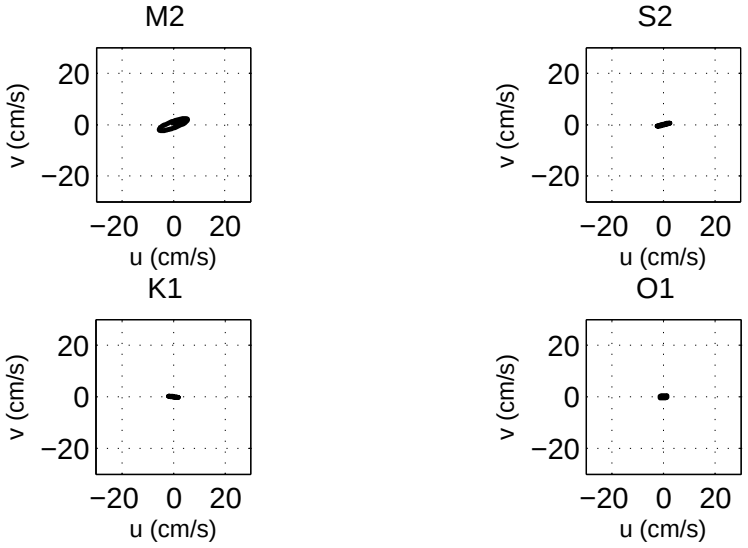

Figure 4.36: Tidal Ellipse of the currentat 20 m without ice coverage, M1.

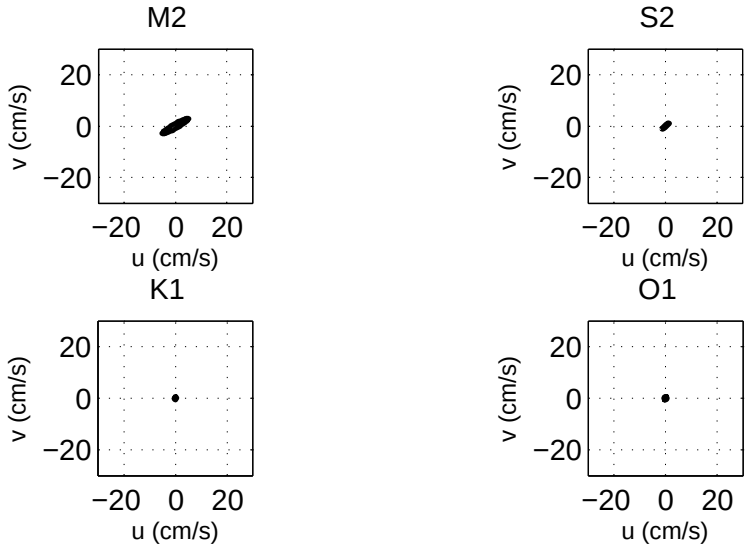

Figure 4.37: Tidal Ellipse of the currentat 50 m without ice coverage, M1.

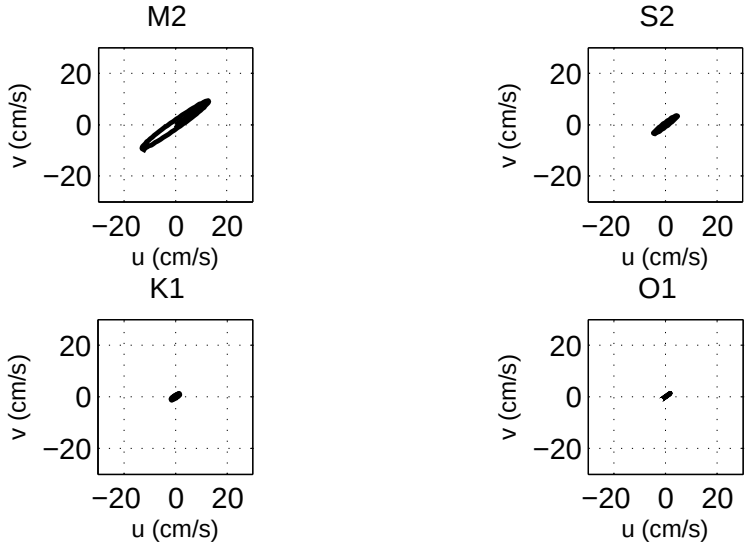

Figure 4.38: Tidal Ellipse of the currentat 100 m without ice coverage, M1.

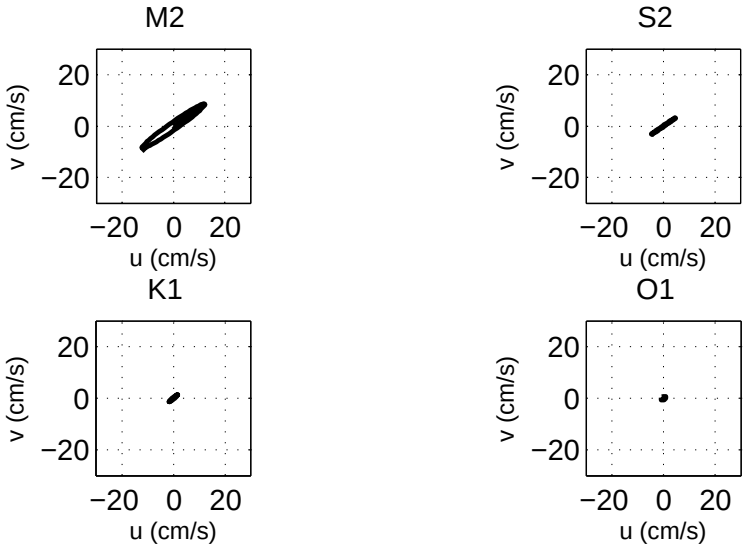

Figure 4.39: Tidal Ellipse of the currentat 150 m without ice coverage, M1.

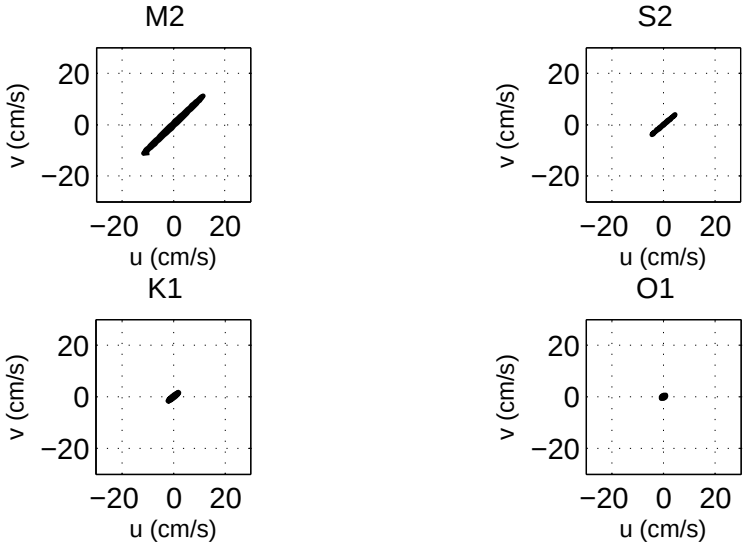

Figure 4.40: Tidal Ellipse of the currentat 175 m without ice coverage, M1.

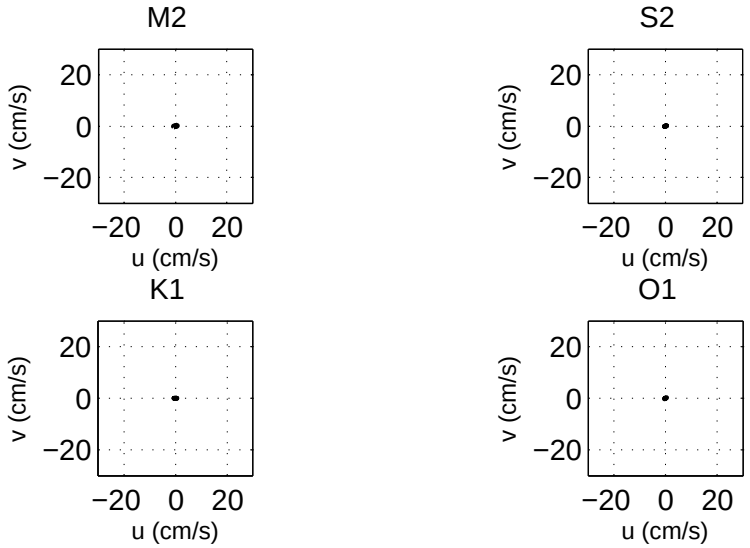

Figure 4.41: Tidal Ellipse of the currentat 10 m with ice coverage, M1.

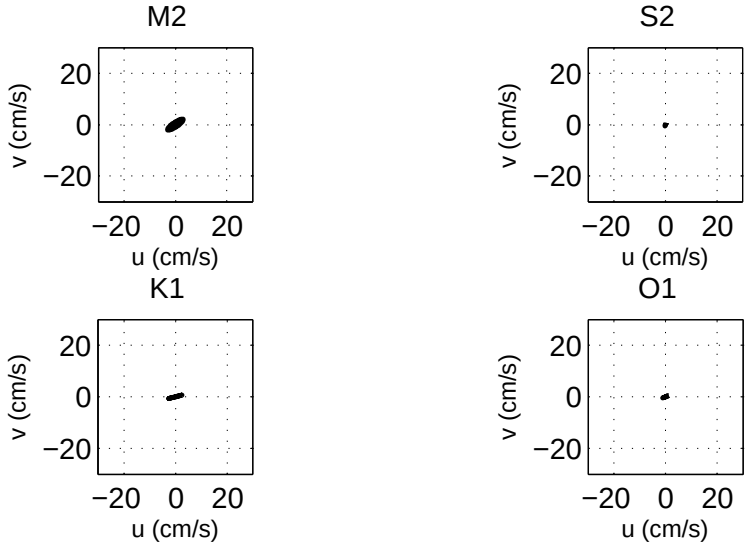

Figure 4.42: Tidal Ellipse of the currentat 20 m with ice coverage, M1.

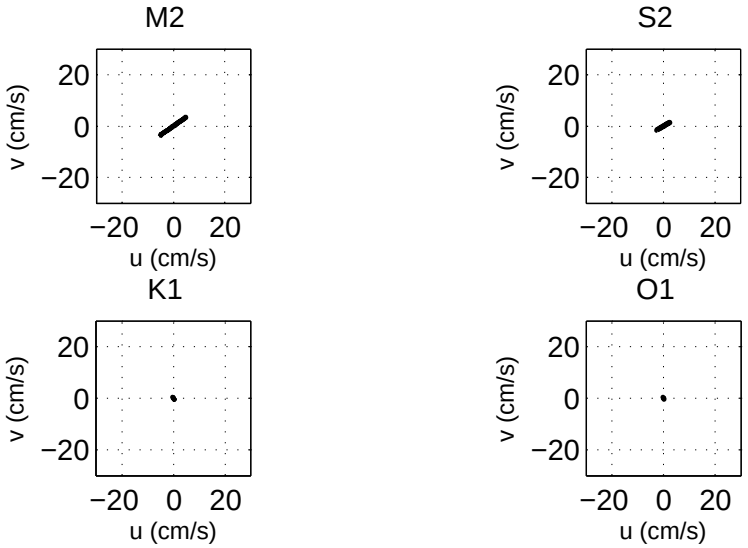

Figure 4.43: Tidal Ellipse of the currentat 50 m with ice coverage, M1.

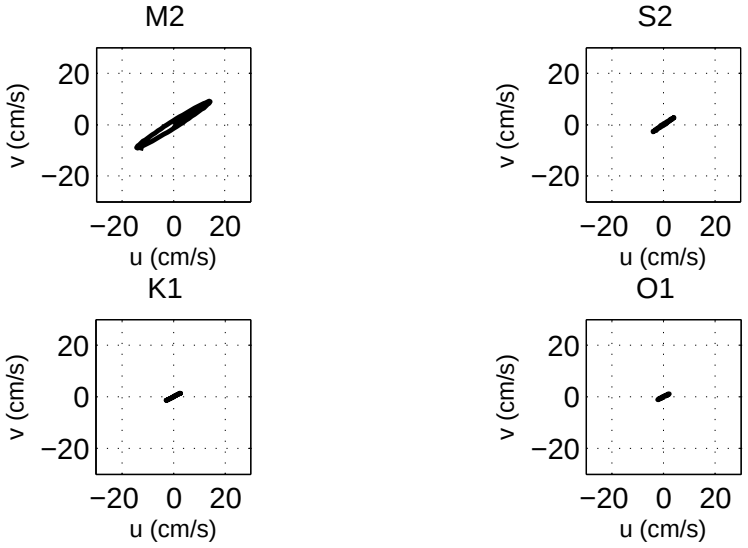

Figure 4.44: Tidal Ellipse of the currentat 100 m with ice coverage, M1.

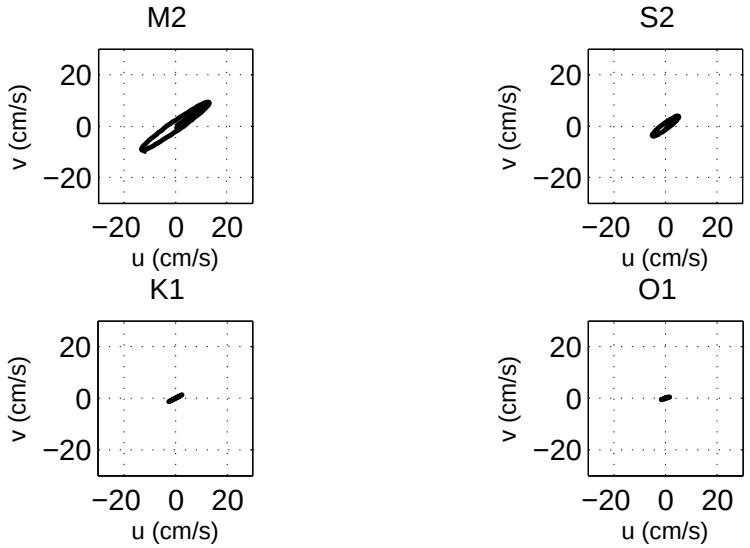

Figure 4.45: Tidal Ellipse of the currentat 150 m with ice coverage, M1.

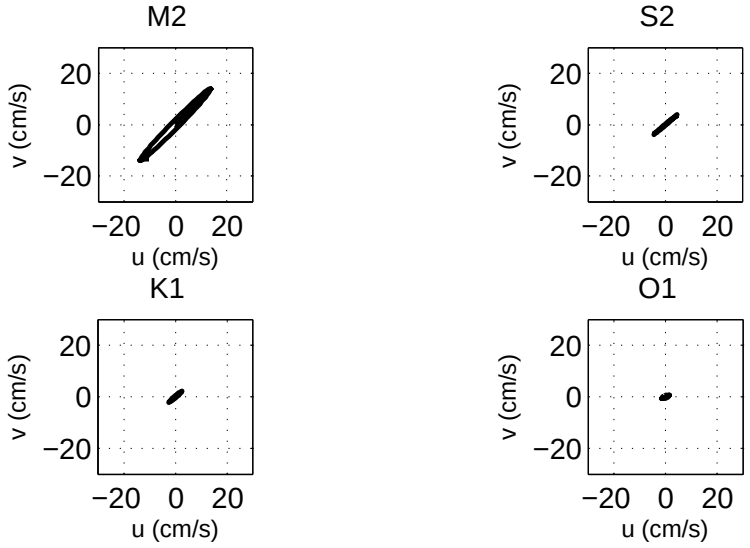

Figure 4.46: Tidal Ellipse of the currentat 175 m with ice coverage, M1.

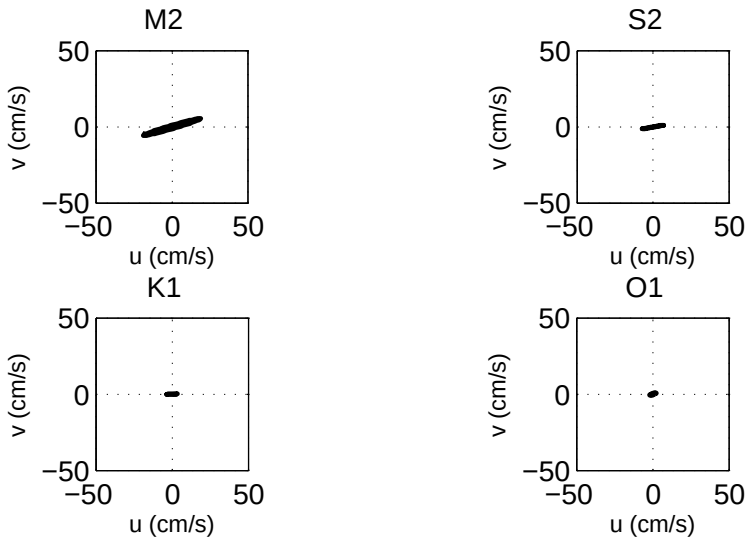

Figure 4.47: Tidal Ellipse of the currentat 10 without ice coverage, M2.

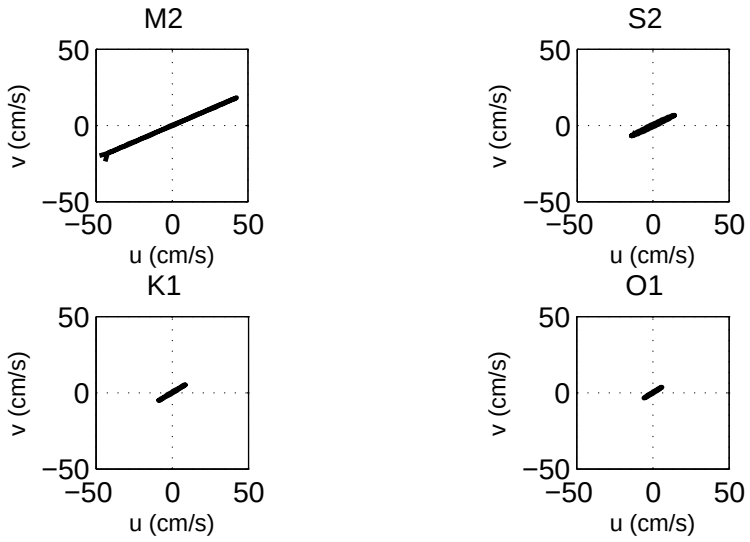

Figure 4.48: Tidal Ellipse of the currentat 20 m without ice coverage, M2.

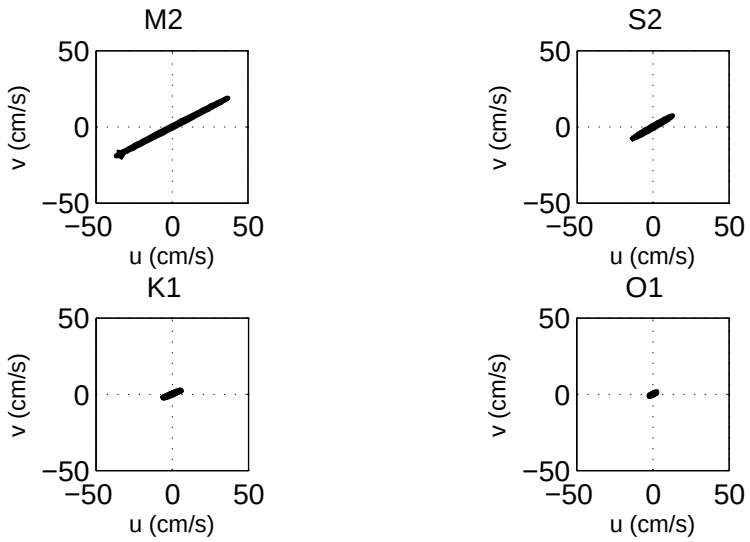

Figure 4.49: Tidal Ellipse of the currentat 50 m without ice coverage, M2.

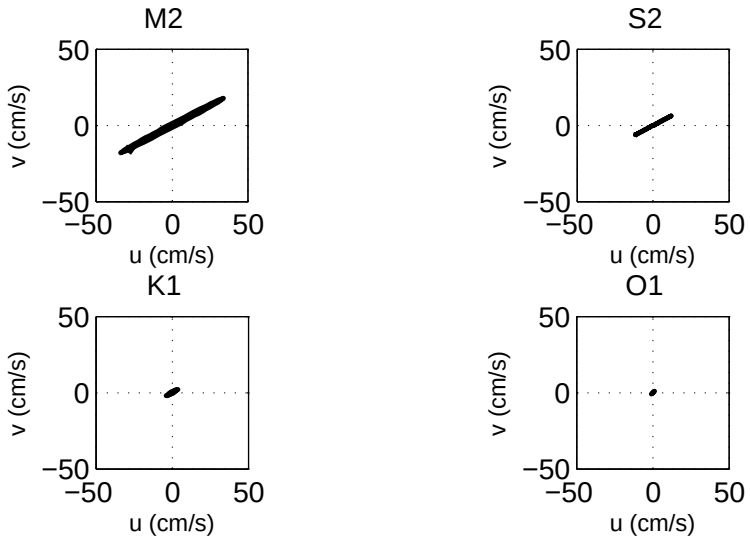

Figure 4.50: Tidal Ellipse of the currentat 95 m without ice coverage, M2.

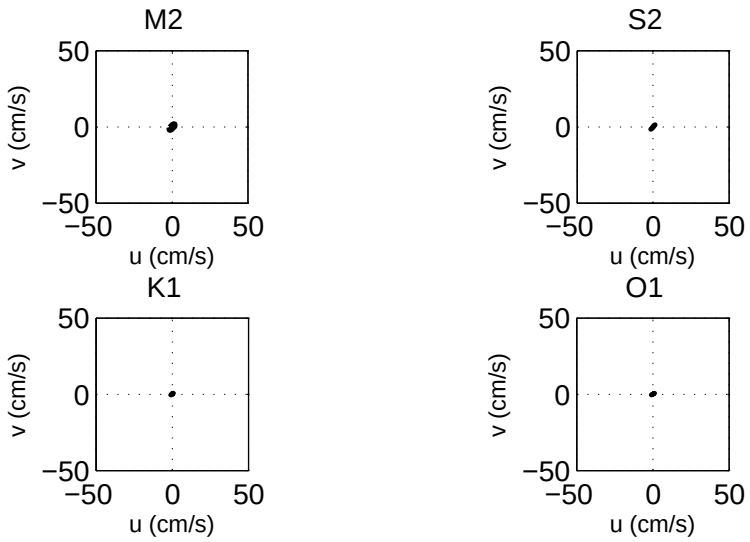

Figure 4.51: Tidal Ellipse of the currentat 10 m without ice coverage, M2.

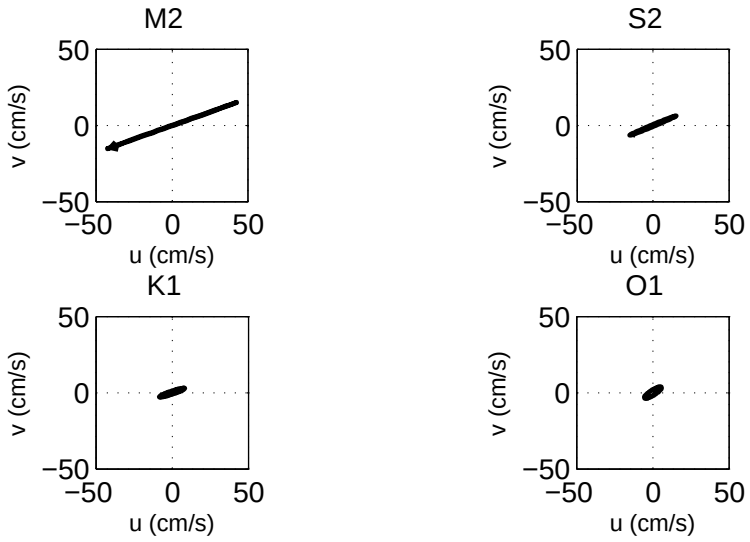

Figure 4.52: Tidal Ellipse of the currentat 20 m without ice coverage, M2.

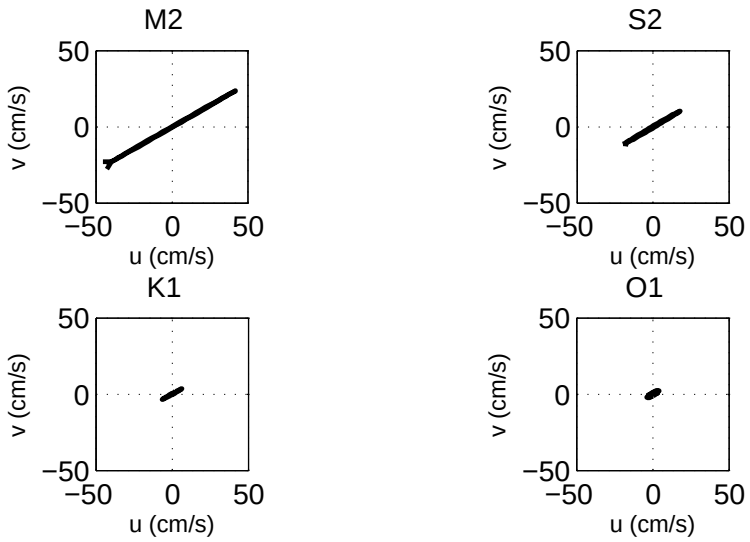

Figure 4.53: Tidal Ellipse of the currentat 50 m without ice coverage, M2.

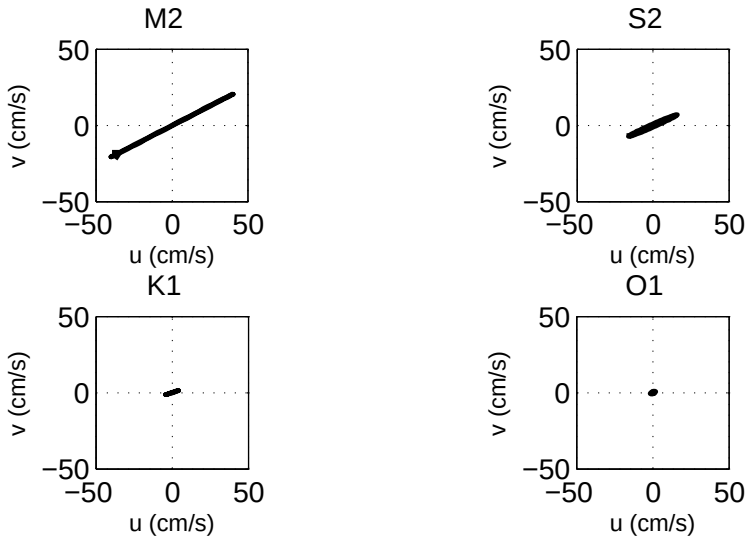

Figure 4.54: Tidal Ellipse of the currentat 95 m without ice coverage, M2.

4.7 Temperature recorded of thermistors

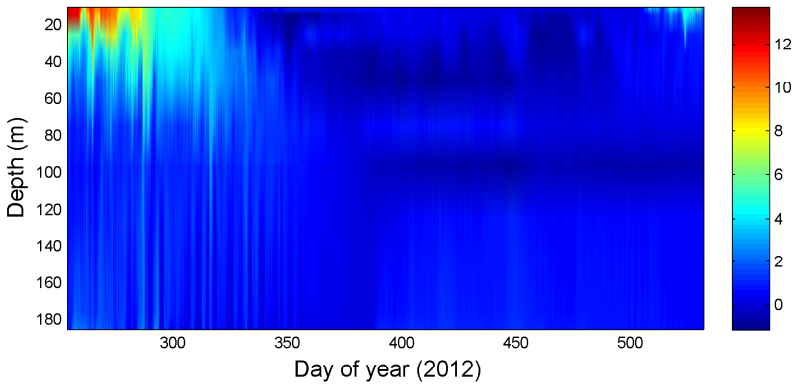

Figure 4.55: Contour plot of temperature at M1, unit in ° C.

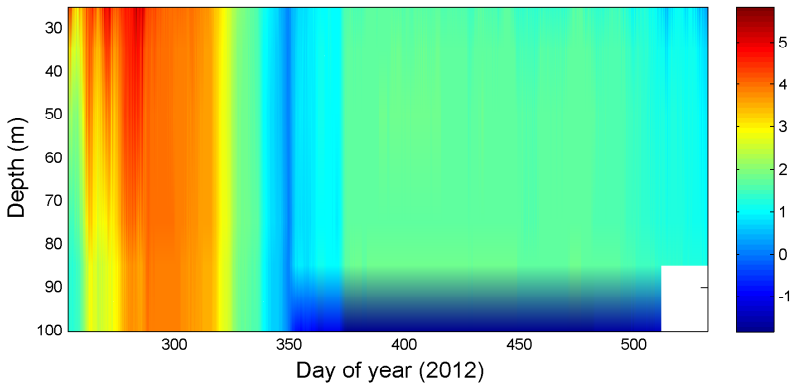

Figure 4.56: Contour plot of temperature at M2, unit in ° C.

Figures 4.55 and 4.56 show depth-time contour plots of temperature derived from thermistors instruments. A low pass Butterworth filter was applied to raw records with cutoff period of 24 hours.

At location M1, surface layer was dominated by warm water of above 12°C before winter (day 320), and the dominant frequency of about 3 to 4 days. Temperatures steadily decreased with depth to 0°C at a depth of 120 m. The temperature then stay at 0°C. With ice cover in the surface during winter time, temperature was around 0°C through whole water column. thereafter with deeper water. Vertical motions of isotherm indicates energetic internal wave propagation.

At location M2, Water was well mixed and surface temperature was slightly higher than lower water column before winter (day 320). Temperature was about 4 1°C before day 320 and dropped to the range of $1 \sim 2$°C after day 320.

4.8 CTD Cast profiles

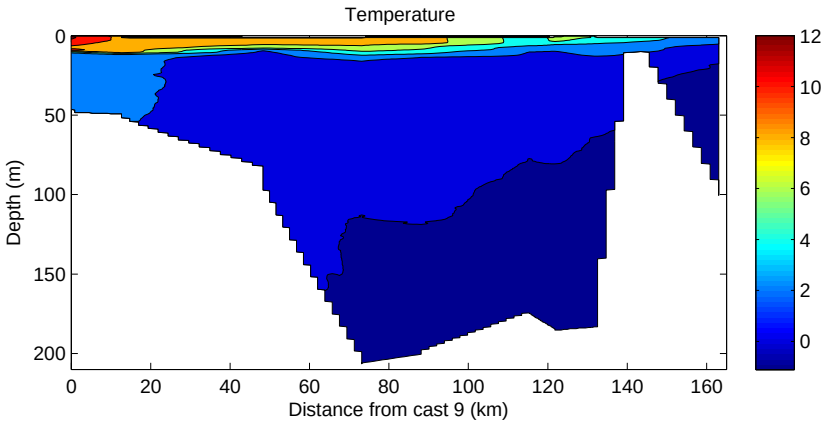

Figure 4.57: Temperature profiles taken along the center of the lake and Narrows, Jun 15 to Jun 17, 2013, unit in $°C$.

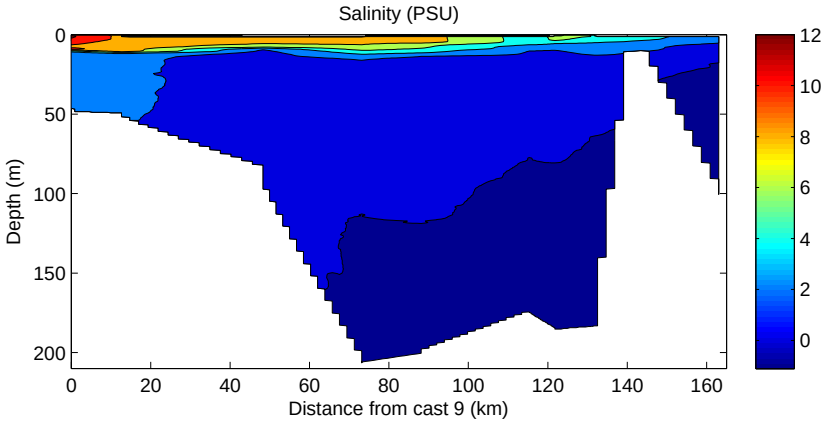

Figure 4.58: Salinity profiles taken along the center of the lake and Narrows, Jun 15 to Jun 17, 2013, unit in PSU.

Figures 4.57, 4.58 and 4.59 shows the temperature, salinity and density profile of CTD transect taken along the center of the lake (Figure 2.1) between Jun 15 to Jun 17, 2013. The stratification in the lake was well defined as those profiles showed a fresh, warm surface layer of about 20 m thick inside the lake. The fresh surface layer became thinner toward the Narrows and almost disappeared outside the Narrows. a strong density gradient had developed below the fresh surface layer.

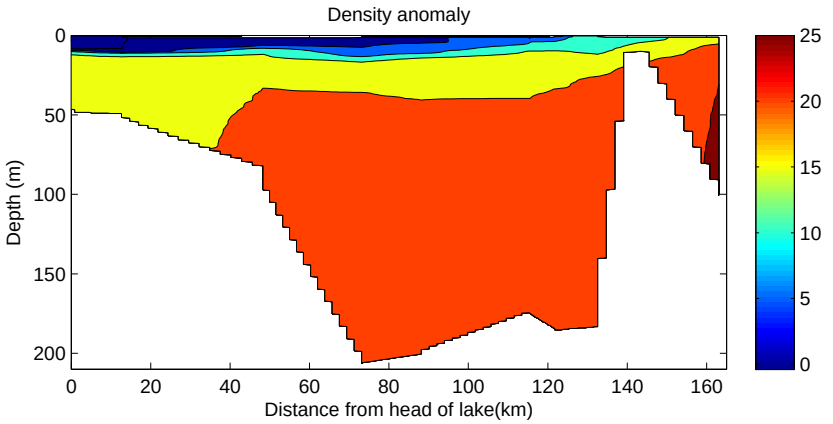

Figure 4.59: Density anomaly profiles taken along the center of the lake and Narrows, Jun 15 to Jun 17, 2013, unit in kg/m^3.

The T-S diagrams in Figure 4.60 show two distinct water masses and strong stratification. Water properties exchanged between surface fresh and bottom saline water mass, with mixing across density surfaces for most of those locations.

The raw temperature and salinity data of CTD casts were plotted as horizontal contour maps for (nominal) depths of surface, 5, 10, 20, and 30 metres, utilising interpolation and extrapolation for locations between the CTD casts (Figures 4.61 to 4.84).

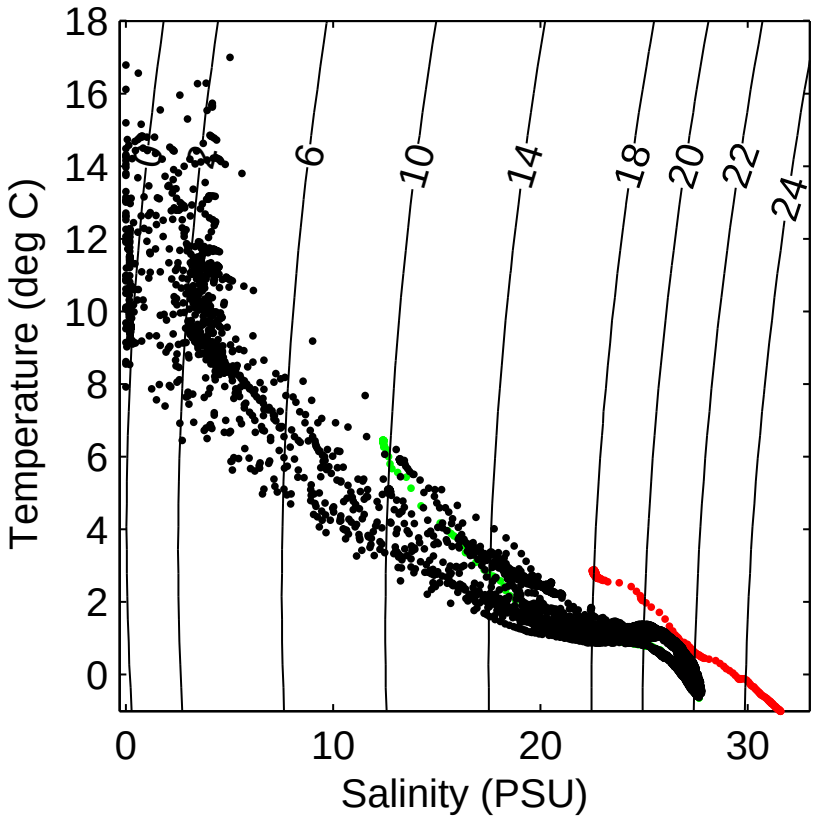

Figure 4.60: T-S diagrams of CTD data collected in the lake (Red:Cast 22 outside the Narrows at M2 ADCP mooring; Green: Cast 21 over the sill in the middle of Narrows at M1 ADCP mooring).

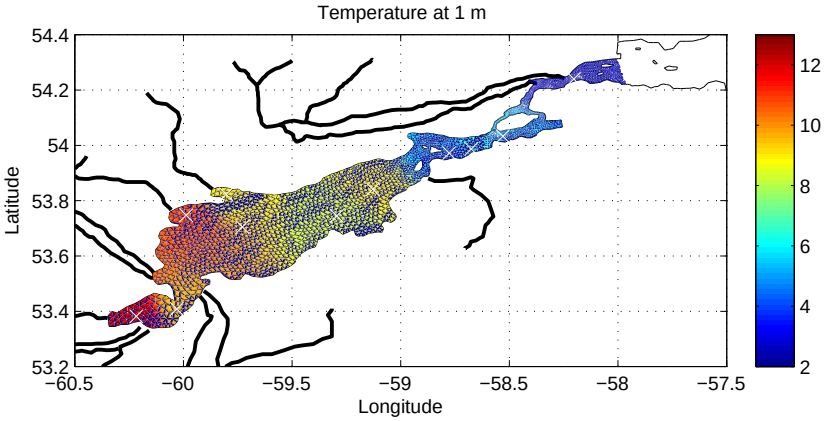

Figure 4.61: Temperature field at 1 m, interpolated and extrapolated from CTD casts between June 15 and June 17, 2013.

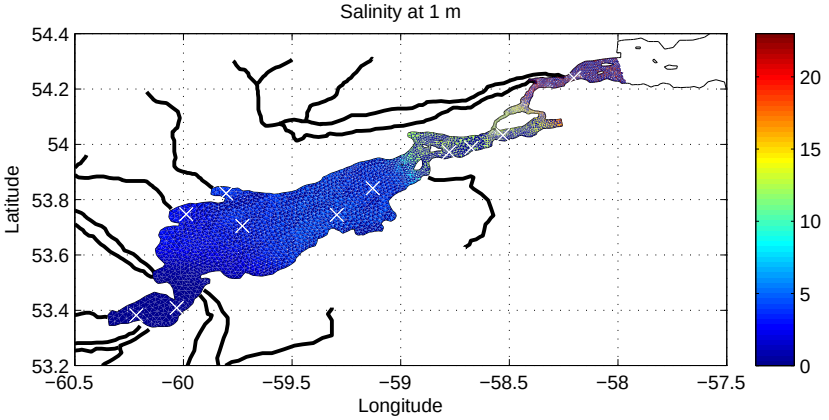

Figure 4.62: Salinity field at 1 m, interpolated and extrapolated from CTD casts between June 15 and June 17, 2013.

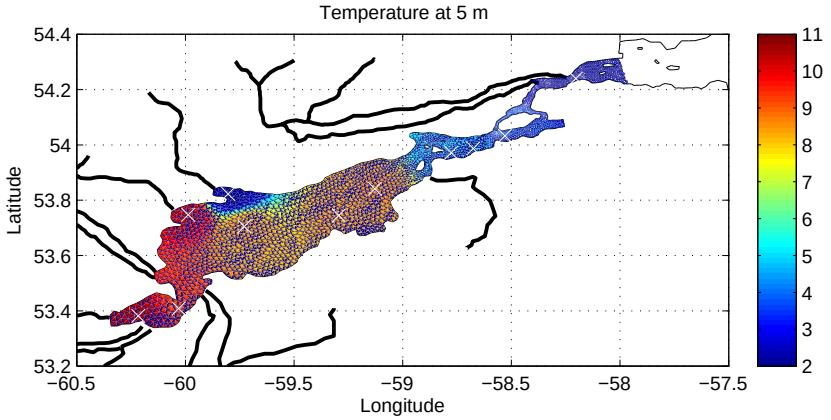

Figure 4.63: Temperature field at 5 m, interpolated and extrapolated from CTD casts between June 15 and June 17, 2013.

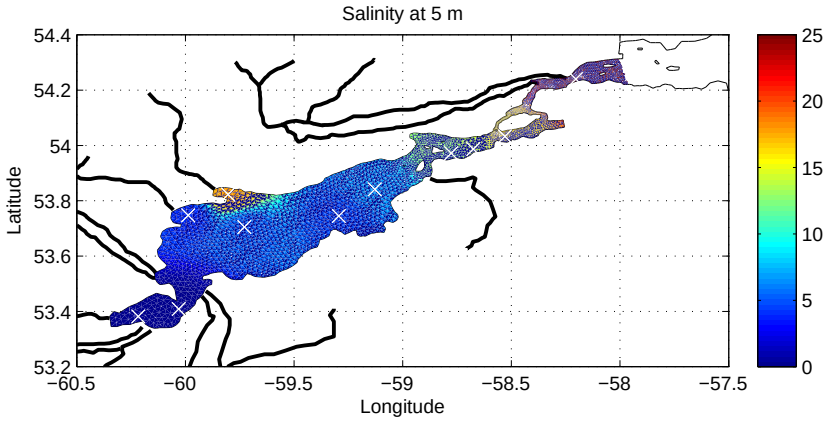

Figure 4.64: Salinity field at 5 m, interpolated and extrapolated from CTD casts between June 15 and June 17, 2013.

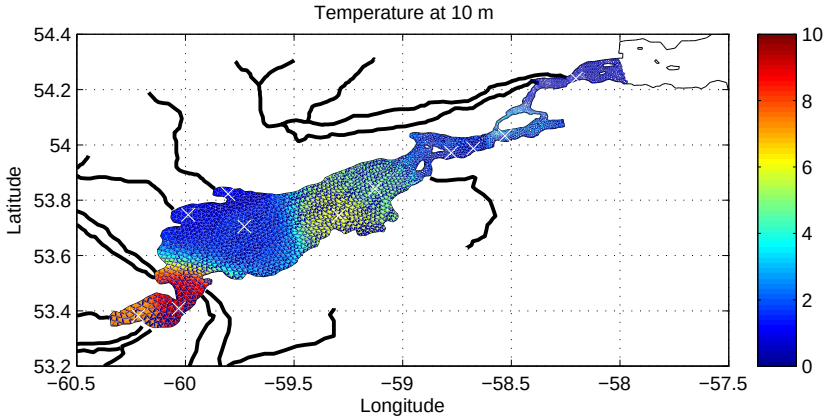

Figure 4.65: Temperature field at 10 m, interpolated and extrapolated from CTD casts between June 15 and June 17, 2013.

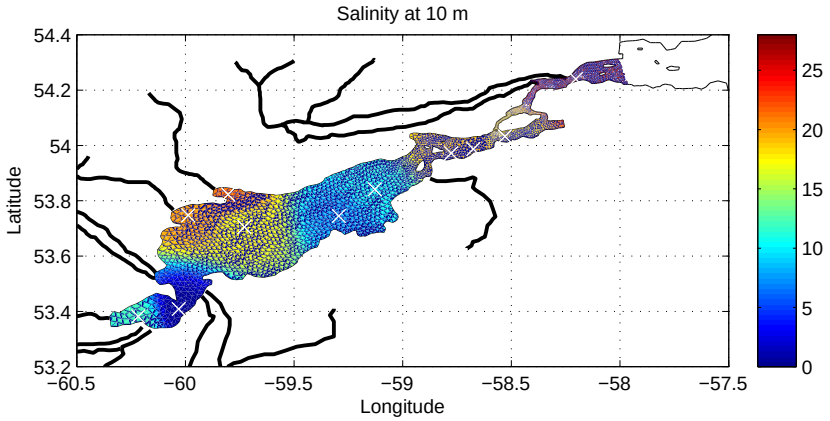

Figure 4.66: Salinity field at 10 m, interpolated and extrapolated from CTD casts between June 15 and June 17, 2013.

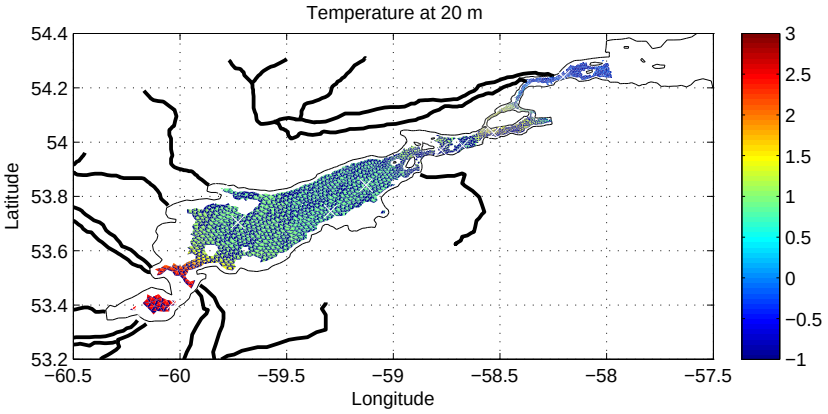

Figure 4.67: Temperature field at 20 m, interpolated and extrapolated from CTD casts between June 15 and June 17, 2013.

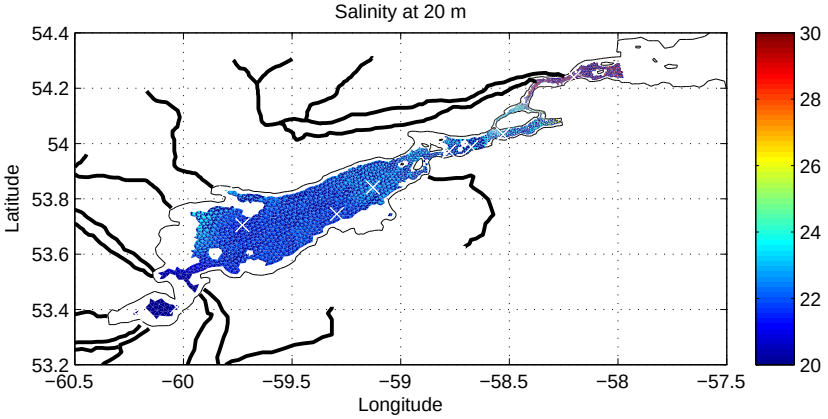

Figure 4.68: Salinity field at 20 m, interpolated and extrapolated from CTD casts between June 15 and June 17, 2013.

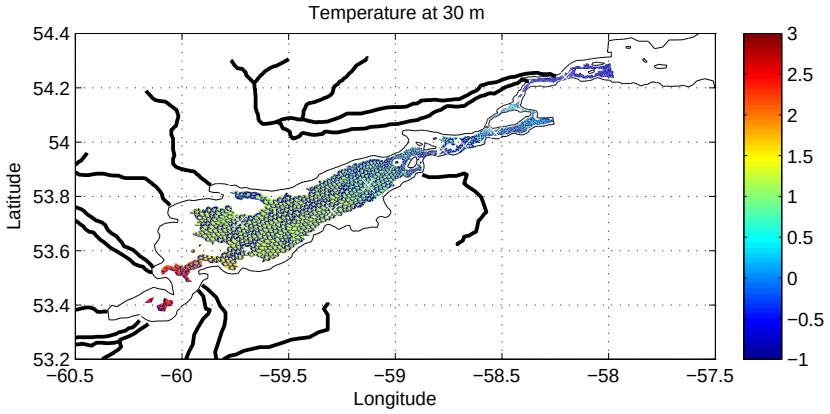

Figure 4.69: Temperature field at 30 m, interpolated and extrapolated from CTD casts between June 15 and June 17, 2013.

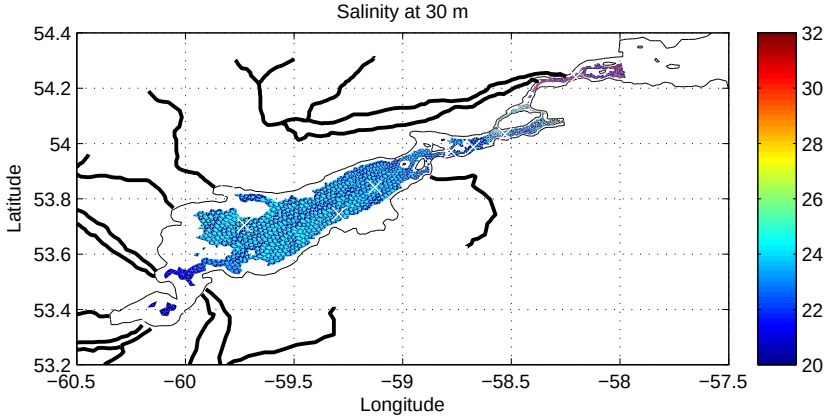

Figure 4.70: Salinity field at 30 m, interpolated and extrapolated from CTD casts between June 15 and June 17, 2013.

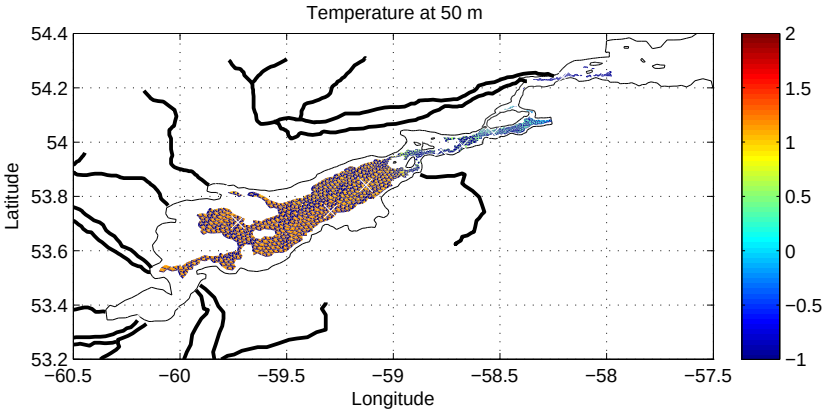

Figure 4.71: Temperature field at 50 m, interpolated and extrapolated from CTD casts between June 15 and June 17, 2013.

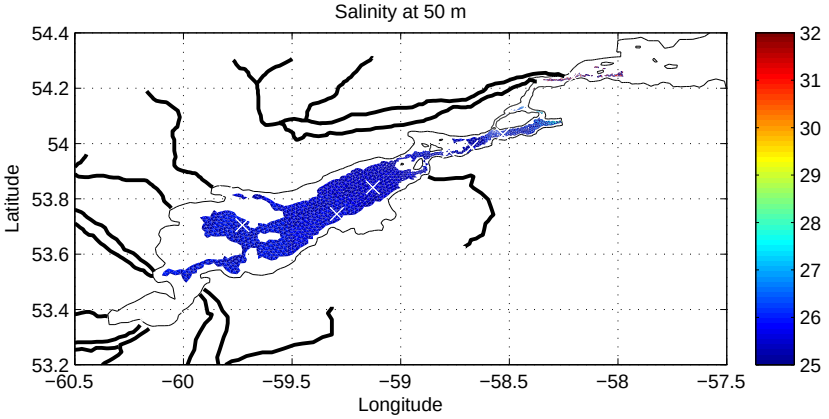

Figure 4.72: Salinity field at 50 m, interpolated and extrapolated from CTD casts between June 15 and June 17, 2013.

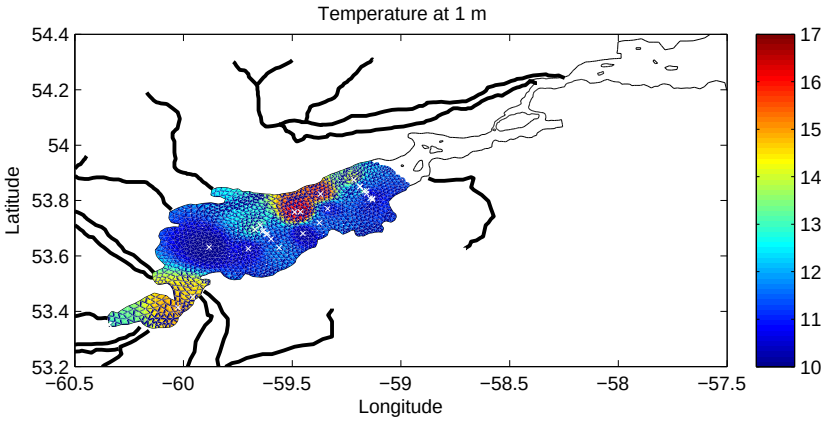

Figure 4.73: Temperature field at 1 m, interpolated and extrapolated from CTD casts between June 19 and July 3, 2013.

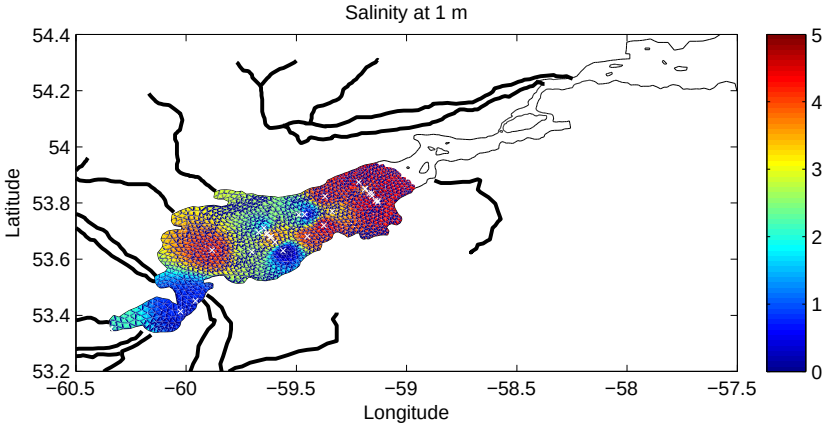

Figure 4.74: Salinity field at 1 m, interpolated and extrapolated from CTD casts between June 19 and July 3, 2013.

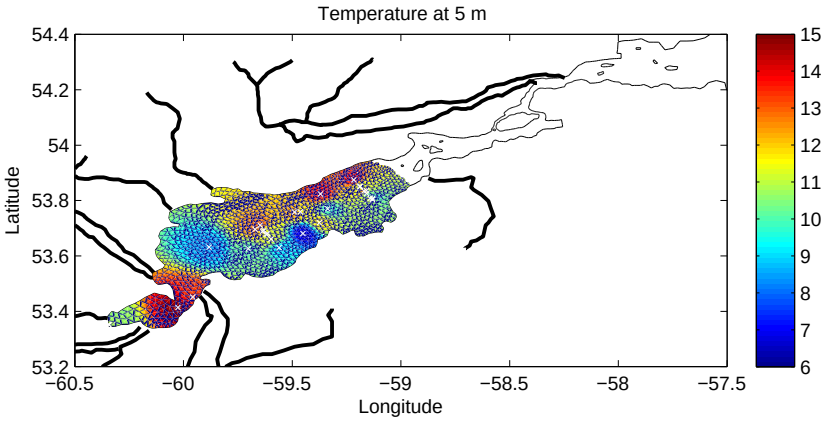

Figure 4.75: Temperature field at 5 m, interpolated and extrapolated from CTD casts between June 19 and July 3, 2013.

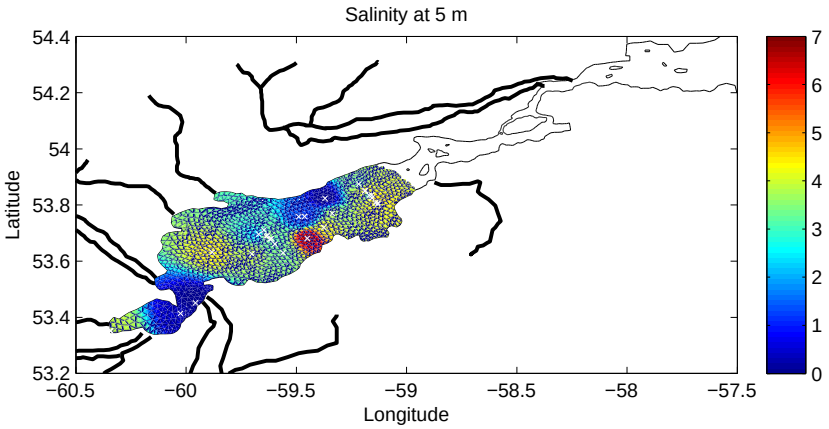

Figure 4.76: Salinity field at 5 m, interpolated and extrapolated from CTD casts between June 19 and July 3, 2013.

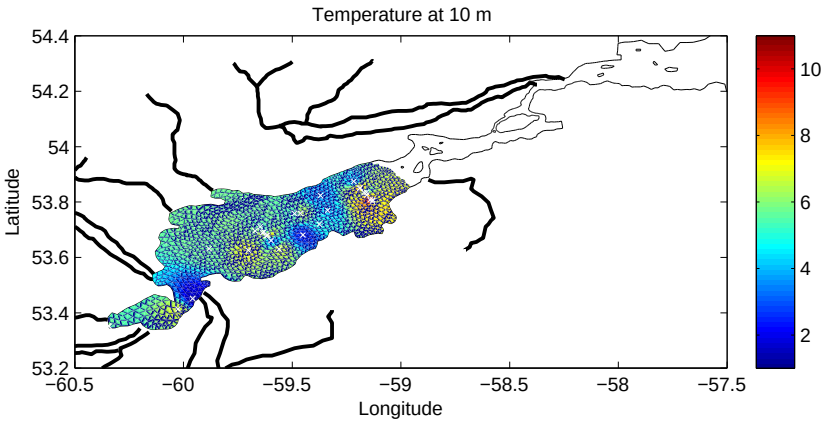

Figure 4.77: Temperature field at 10 m, interpolated and extrapolated from CTD casts between June 19 and July 3, 2013.

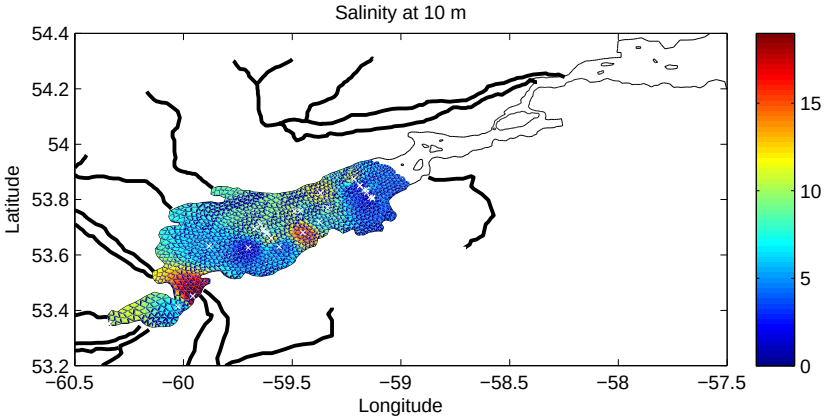

Figure 4.78: Salinity field at 10 m, interpolated and extrapolated from CTD casts between June 19 and July 3, 2013.

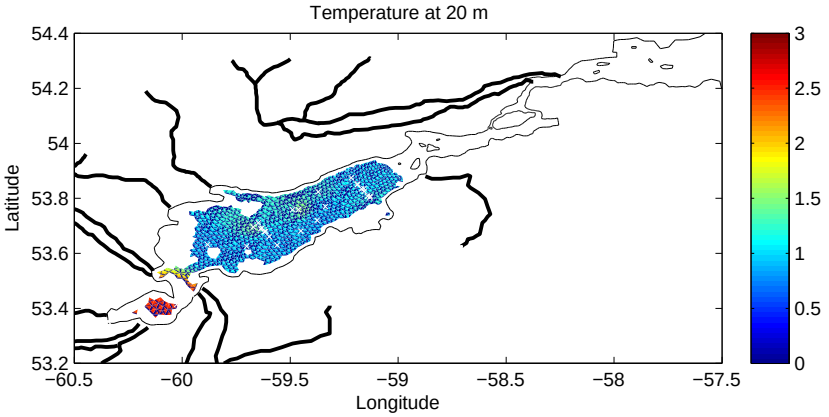

Figure 4.79: Temperature field at 20 m, interpolated and extrapolated from CTD casts between June 19 and July 3, 2013.

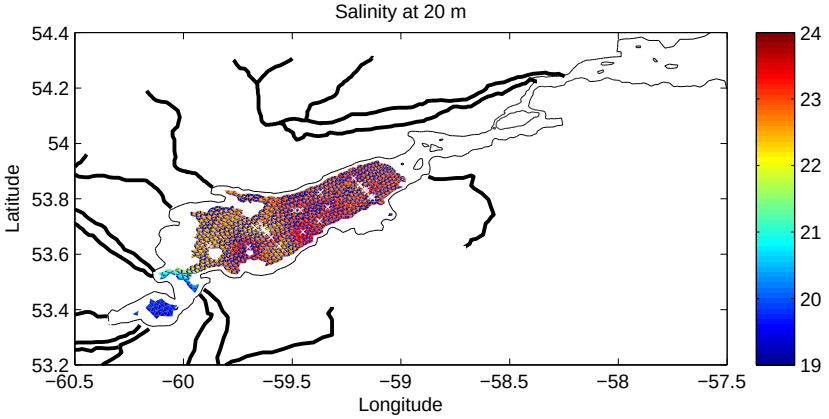

Figure 4.80: Salinity field at 20 m, interpolated and extrapolated from CTD casts between June 19 and July 3, 2013.

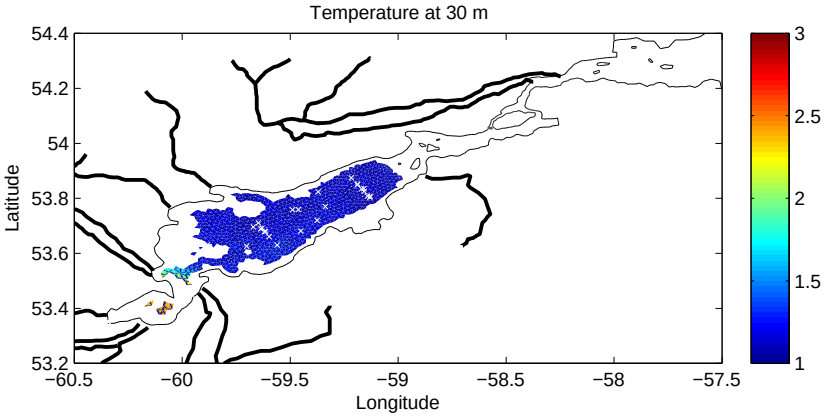

Figure 4.81: Temperature field at 30 m, interpolated and extrapolated from CTD casts between June 19 and July 3, 2013.

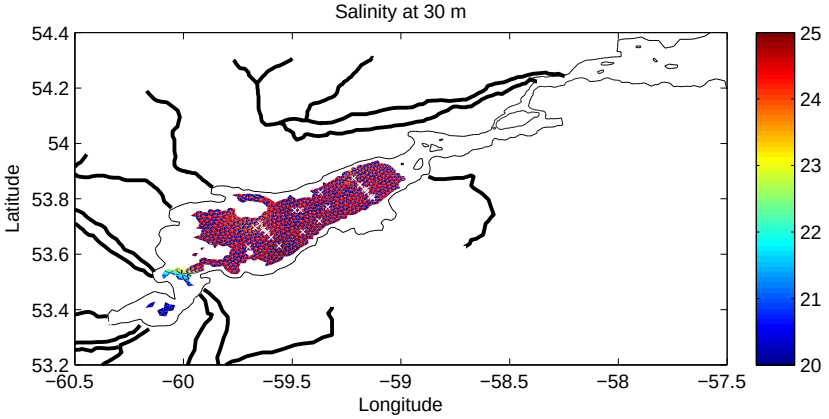

Figure 4.82: Salinity field at 30 m, interpolated and extrapolated from CTD casts between June 19 and July 3, 2013.

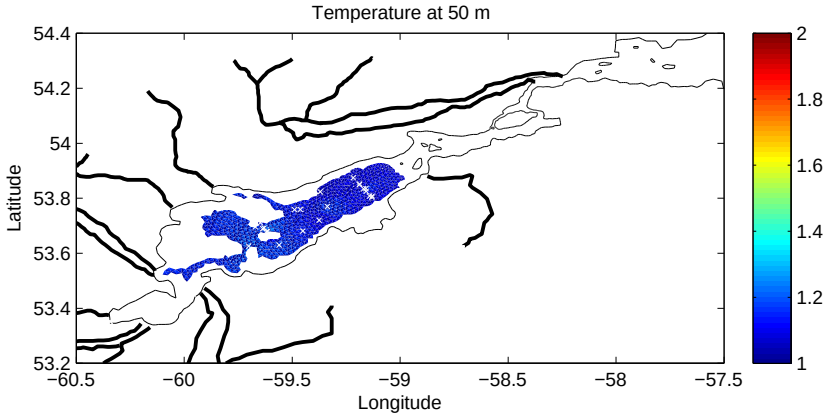

Figure 4.83: Temperature field at 50 m, interpolated and extrapolated from CTD casts between June 19 and July 3, 2013.

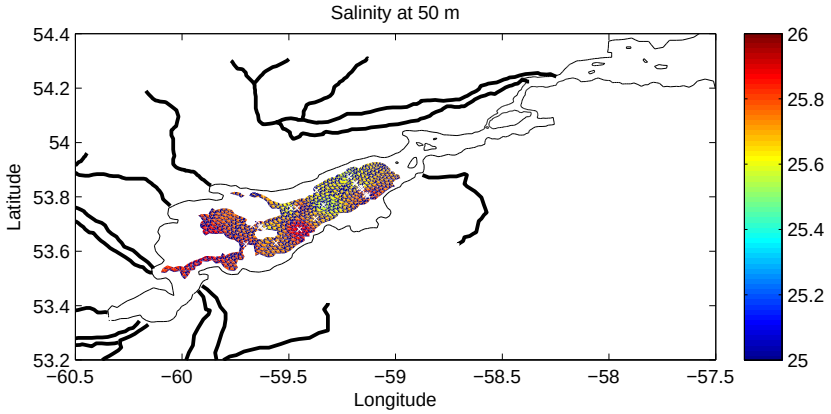

Figure 4.84: Salinity field at 50 m, interpolated and extrapolated from CTD casts between June 19 and July 3, 2013.

4.9 Atmospheric records at Happy Valley-Goose Bay

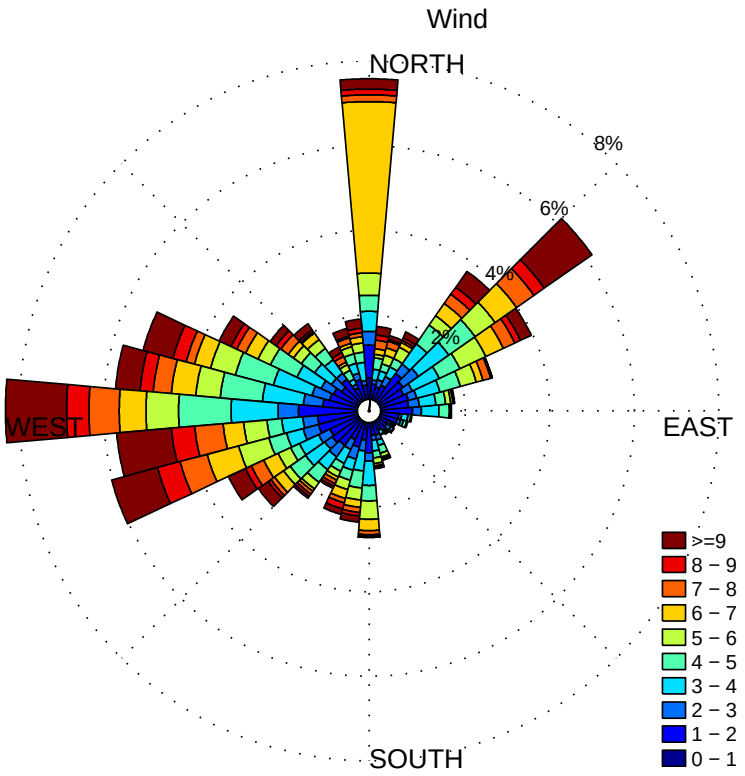

Figure 4.85: Current rose of wind at Goose bay, Labrador, unit in m/s.

Figures 4.85, 4.86 and 4.87 show atmospheric records at the nearby Happy Valley-Goose Bay weather station. Wind roses from the Happy Valley-Goose Bay weather station are shown in Figure 4.85. These preferred wind direction are west and southwest for the mooring period.

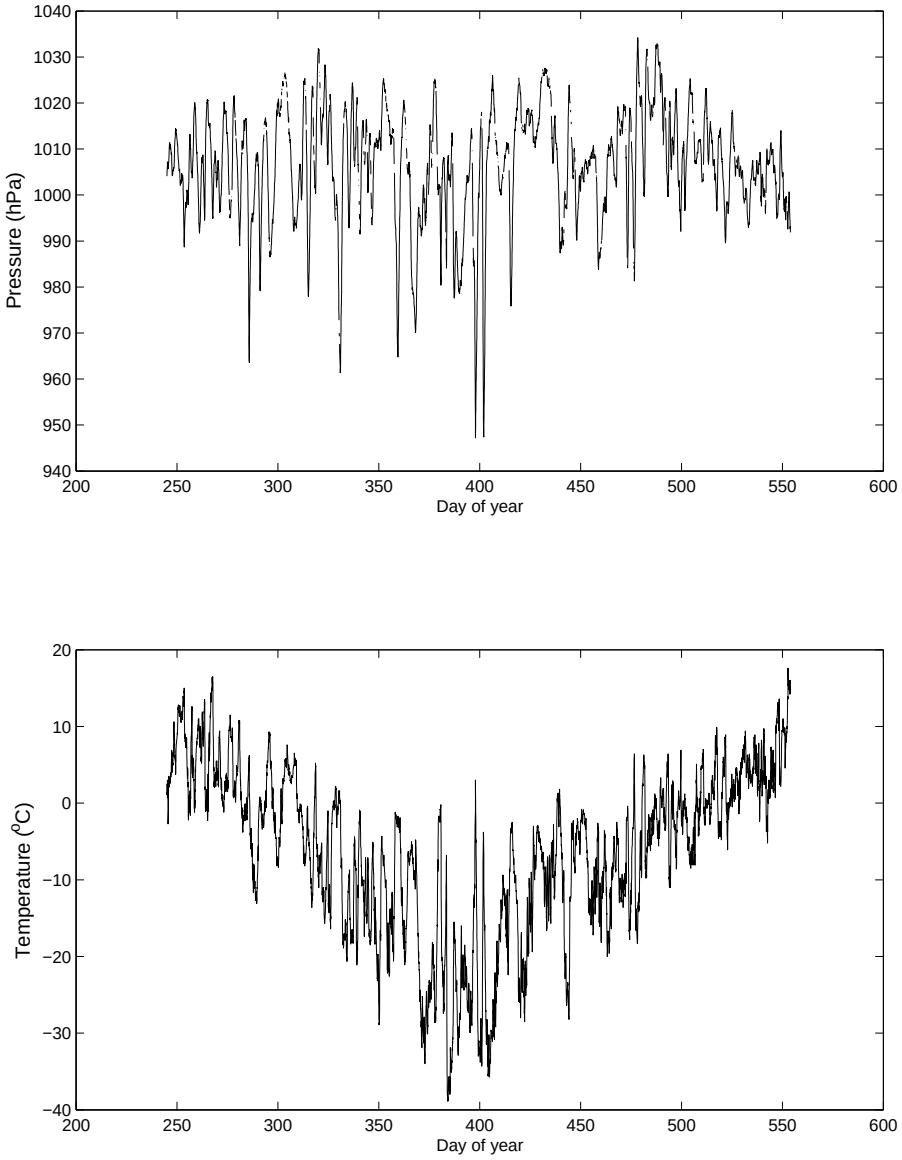

Figure 4.86: Air pressure and temperature at Goose bay, Labrador.

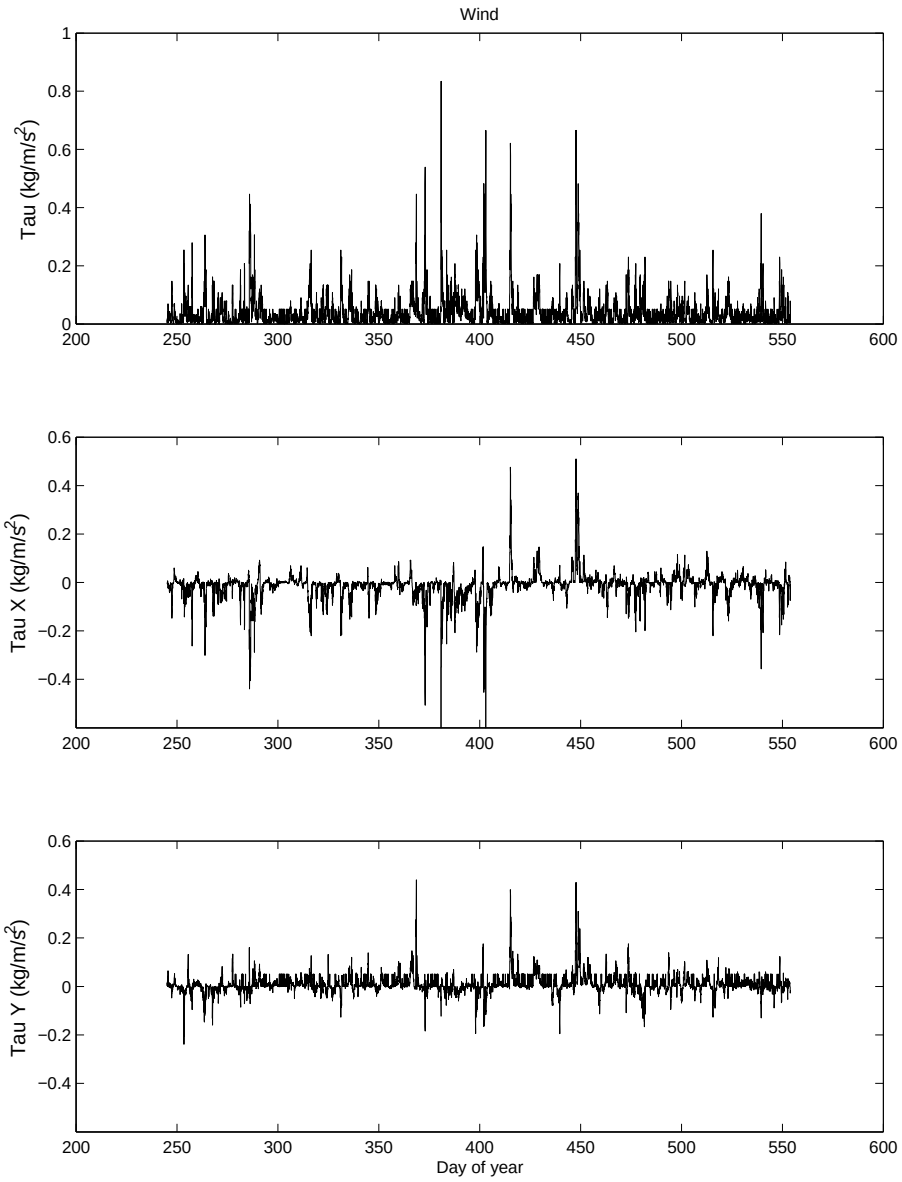

Figure 4.87: Wind stress at Goose bay, Labrador.